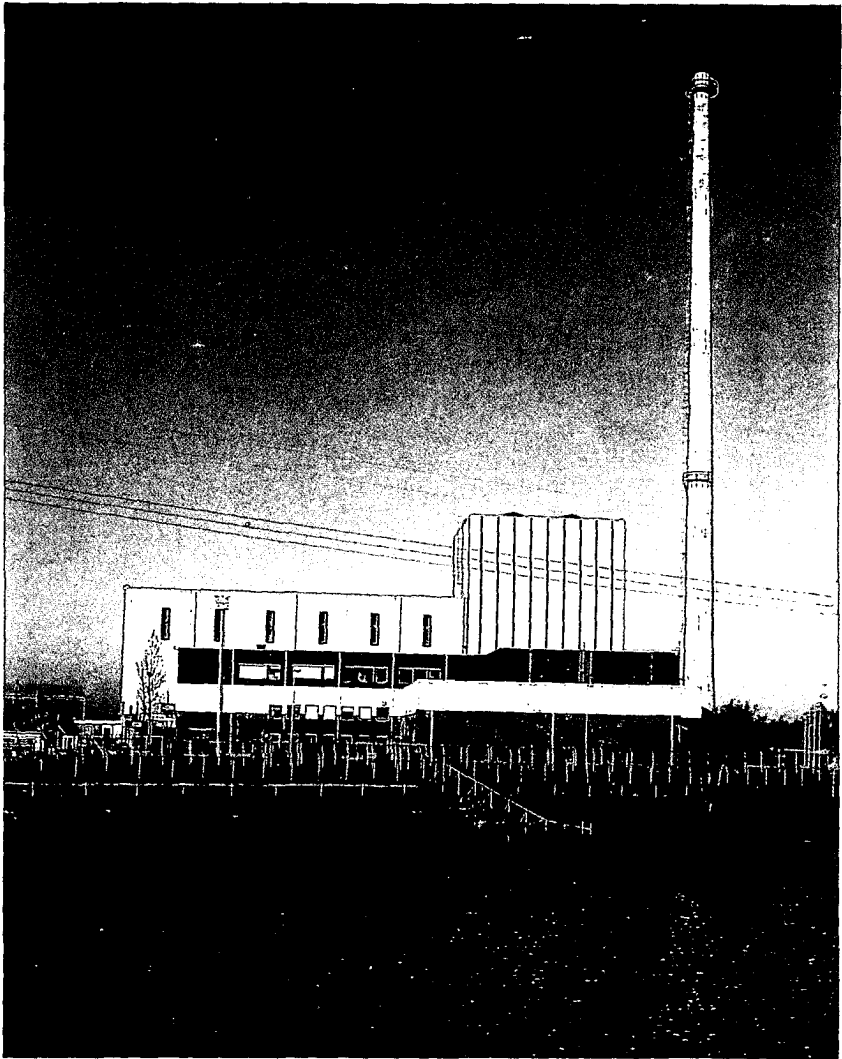


STABILITY MONITORING OF A NATURAL-CIRCULATION-COOLED BOILING WATER REACTOR



TR diss
1704

T.H.J.J. VAN DER HAGEN

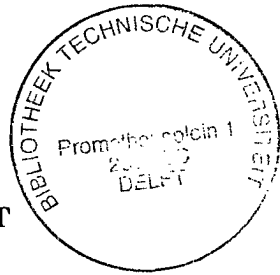
465274

3179045

TR diss 1704

**STABILITY MONITORING
OF A NATURAL-CIRCULATION-COOLED
BOILING WATER REACTOR**

PROEFSCHRIFT



TER VERKRIJGING VAN DE GRAAD VAN DOCTOR AAN
DE TECHNISCHE UNIVERSITEIT DELFT, OP GEZAG VAN
DE RECTOR MAGNIFICUS, PROF. DR. P.A. SCHENCK,
IN HET OPENBAAR TE VERDEDIGEN TEN OVERSTAAN
VAN EEN COMMISSIE DOOR HET COLLEGE VAN
DEKANEN DAARTOE AANGEWEEZEN,
OP 9 MAART 1989 TE 16.00 UUR

door

TIMOTHEUS HENRICUS JOHANNES JACOBUS VAN DER HAGEN

geboren te Tilburg,
natuurkundig ingenieur

**TR diss
1704**

Dit proefschrift is goedgekeurd door de promotor

Prof. Dr. Ir. H. van Dam

STELLINGEN

behorende bij het proefschrift

Stability monitoring of a natural-circulation-cooled boiling water reactor

1. De door March-Leuba en Fry c.s. toegepaste beginvoorwaarden voor de bepaling van de impulsresponsie uit een autoregressief model zijn in strijd met de fysische werkelijkheid daar zij een momentane signaaloverdracht impliceren.

*J. March-Leuba,
Ph.D. thesis, The University of Tennessee, Knoxville (1984)
D.N. Fry, J. March-Leuba en F.J. Sweeney,
NUREG/CR-3303, ORNL/TM-8774 Knoxville, Tennessee (1984)
Dit proefschrift, hoofdstuk 8*

2. Het door March-Leuba c.s. gehanteerde uitgangspunt voor de bepaling van overdrachtsfuncties uit ruissignalen (alle meetbare overdrachtsfuncties corresponderen met een minimum-fasesysteem) is niet toepasbaar op een kokend-waterreactor.

*J. March-Leuba, R.T. Wood, P.J. Otaduy en C.O. McNew
Nuclear Technology 74, 38-52 (1986)*

3. Het niet voldoende onderkennen van het belang van 'alignment' bij het bepalen van looptijden met behulp van ruiscorrelatie leidt tot onjuiste resultaten.

Dit proefschrift, hoofdstuk 4

4. Het gebruikelijke stemmen van een gitaar door het vergelijken van flageolettonen stemt niet overeen met de gelijkzwevende stemming en werkt derhalve ontstemmend.
5. De verbetering van muziekinstrumenten wordt in hoge mate gefrustreerd door de emotionele weerstand tegen het gebruik van kunststoffen als basismateriaal voor instrumenten.
6. Wedstrijdzwemmen is oneerlijk daar lange zwemmers/sters een kortere afstand hoeven af te leggen dan kleinere deelnemers/sters.
7. De toepassing van automatische administratiesystemen leidt in veel gevallen tot een dubbele administratie.
8. De uitspraak van Arthur Schopenhauer (1788-1860) "Een van de dingen die de vooruitgang der mensheid het meest in de weg staan, is dat mensen niet luisteren naar degenen die het verstandigst, doch naar degenen die het luidst spreken" is ook van toepassing op de kernenergieproblematiek.
9. De taalkundige affiliatie van het woord 'kernenergie' met het woord 'kernwapen' staat de maatschappelijke acceptatie van kernenergie in de weg.
10. De tijdens conferenties veel gebezigde foutieve uitspraak van de Engelse afkorting 'BWR' als 'be we are' veroorzaakt communicatiestoornissen.

9 maart 1989
T.H.J.J. van der Hagen

*Aan mijn ouders
en alle anderen
die interesse
in mijn werk
hebben getoond*

Cover photograph: the Dodewaard boiling water reactor

CIP-GEGEVENS KONINKLIJKE BIBLIOTHEEK DEN HAAG

Hagen, T.H.J.J. van der

Stability monitoring of a natural-circulation-cooled boiling water reactor / T.H.J.J. van der Hagen. - Arnhem : KEMA. - Ill.

Proefschrift Delft. - Met lit. opg.

ISBN 90-353-1017-9

SISO 644.5 UDC 621.039(043.3)

Trefw.: kokend-waterreactoren ; Dodewaard / kokend-waterreactoren ; stabiliteitsmetingen.

Contents

Summary	9
Chapter 1: Introduction: stability monitoring of a BWR	11
Description of a BWR	12
Principle of operation	12
Characteristics of the Dodewaard reactor	13
Stability	14
Second-order system	16
Stability of a BWR	18
Reactor-kinetic stability	19
Thermal-hydraulic stability	20
Scope of this study	20
Outline	21
Chapter 2: The frequency-dependent field-of-view of a neutron detector	23
Numerical model	23
Theory	23
Non-conventional cross-sections in diffusion calculations	27
Calculations on the field-of-view of Dodewaard detectors	30
Phase behaviour of the field-of-view	30
Two-dimensional modelling	32
The field-of-view of an in-core detector	34
The field-of-view of an ex-vessel detector	36
Evaluations	41
Chapter 3: Measuring in-core coolant velocity by noise correlation	43
Velocity determination by noise correlation	44
Design and manufacturing of a twin self-powered detector	45
Velocity profile	47
Conclusions	49

Chapter 4: Interpretation of velocities determined by noise analysis for various void fractions and flow regimes in two-phase flow	51
<i>(published in Progress in Nuclear Energy 21: 565-573; 1988)</i>	
<i>(republished with permission of Pergamon Press PLC)</i>	
Abstract	51
Introduction	52
Description of the air/water loop	52
Characteristic functions	54
Theoretical velocities	56
Velocities obtained by noise correlation	60
Conclusions	62
Acknowledgement	63
References	63
Chapter 5: Fast measurements of the in-core coolant velocity in a BWR by neutron noise analysis	65
<i>(published in Annals of Nuclear Energy 15: 439-448, 1988)</i>	
<i>(reprinted with permission of Pergamon Journals Ltd.)</i>	
Abstract	67
Introduction	67
Fast velocity determination	67
Velocity monitoring	71
Accuracy	71
Velocity monitoring in practice	73
Estimated accuracy in a BWR	73
Applications in the Dodewaard BWR	74
Averaged velocity response	74
Fast velocity measurements	74
Concluding remarks	75
Acknowledgement	76
References	76
Chapter 6: Determination of reactor stability by deterministic and stochastic methods	77
Experimental conditions	78
Evaluation of the experimental results	79
Reactor-kinetic stability	79
Thermal-hydraulic stability	80
Total-plant stability	82
Stability during the cycle start-up phase	83
Conclusions	83

Chapter 7: Experimental and theoretical evidence for a short effective fuel time constant in a BWR	85
<i>(published in Nuclear Technology 83: 171-181, 1988)</i>	
<i>(reprinted with permission of the American Nuclear Society)</i>	
Abstract	87
Introduction	87
Lumped parameter model	87
Experimental results	88
Peaking of the reactor transfer function	88
Transfer function from power to pressure	88
Fuel elongation	91
Numerical analysis	92
Stationary temperature profile	92
Dynamic behaviour	92
Concluding Remarks	96
References	96

Chapter 8: Application of noise analyses to stability determination of a natural-circulation-cooled BWR	99
<i>(published in Progress in Nuclear Energy 21: 753-761, 1988)</i>	
<i>(republished with permission of Pergamon Press PLC)</i>	
Abstract	99
Introduction	100
Experimental conditions	101
Stability evaluations	101
Absolute stability	101
Monitoring changes in stability	104
Concluding Remarks	109
References	109

Chapter 9: Stability monitoring by means of the rms ratio and variations of the in-core coolant velocity	111
Experimental conditions	111
Stability analysis using the ex-vessel neutron flux	114
Stability monitoring using the rms ratio	114
The influence of the reflector on the rms ratio	120
Variations of the in-core coolant velocity	122
Axial profile of velocity variations	122
Radial profile of velocity variations	123
Comparison of velocity variations at one core position	125
Conclusions	128

References	129
Appendix 1: radial peaking factors and outlet void fractions for cases A and B	135
Appendix 2: standard deviation of the estimated rms ratio	139
Appendix 3: nomenclature	143
List of most important symbols	143
List of abbreviations	146
Samenvatting	147
概要	149
Acknowledgements	151
Curriculum vitae	153

Summary

Methods for monitoring the stability of a boiling water reactor (BWR) are discussed. Surveillance of BWR stability is of importance as problems were encountered in several large reactors. Moreover, surveying stability allows plant owners to operate at high reactor power with acceptable stability margins.

The results of experiments performed on the Dodewaard BWR (The Netherlands) are reported. Research on this particular reactor is of interest as this type is cooled by natural circulation, a cooling principle that is also being considered for new reactor designs. Only two reactors of this type are currently in operation.

The stability of the Dodewaard reactor was studied both with deterministic methods (control-rod steps and pressure-valve movements) and by noise analysis. The latter method can be applied during normal operation and avoids any intentional system disturbance since a continuous intrinsic noise source is formed by the boiling process of the water in the core. Three types of stability are distinguished and were investigated separately: reactor-kinetic stability, thermal-hydraulic stability and total-plant stability. It is shown that the Dodewaard reactor has very large stability margins.

A simple yet reliable stability criterion is introduced that was tested thoroughly. It can be derived on-line from the noise signal of ex-vessel neutron detectors during normal operation. The sensitivity of neutron detectors to in-core flux perturbations - reflected in the so-called field-of-view of the detector - was calculated in order to insure proper stability surveillance.

A novel technique is presented which enables the determination of variations of the in-core coolant velocity by noise correlation. The velocity measured was interpreted on the basis of experiments performed on the air/water flow in a model of a BWR coolant channel. It appeared from this analysis that the velocity measured was much higher than the volume-averaged water velocity, the volume-averaged air velocity and the volumetric flux, which other investigators suggested had equivalent values.

The applicability of the above-mentioned technique to monitoring of local channel-flow stability was tested. It was observed that stability effects on the coolant velocity are masked by other effects originating from the local flow pattern. However, the variations of the coolant veloci-

ties in the Dodewaard reactor are very small because the channel flow is very stable.

Experimental and theoretical studies were performed on the fuel time constant, a parameter of great importance to the reactor-kinetic stability. It is shown that the effective value of this constant can be much smaller than the value usually agreed on.

Finally, the methods presented for stability monitoring were applied to various conditions of the Dodewaard core.

Chapter 1

Introduction: stability monitoring of a BWR

The stability of boiling water reactors (BWRs) has been the object of investigation since the very first design experiments in the 1950s. In fact, it was the concern about stability that delayed the introduction of BWRs until it was shown experimentally that unstable behaviour is not to be expected at high system pressures (Kramer, 1958).

Despite these reassuring findings, stability monitoring of BWRs is still of great importance for optimum plant performance. It has been observed that large BWRs in current operation do show a less stable behaviour under certain conditions with low coolant flow. These conditions may be encountered during start-up or shut-down, during rod-pattern changes and as a result of tripping of one or more recirculation pumps.

Stability problems under such conditions were reported for, among others, the following plants:

- (1) the BWR of Santa Maria de Garona (Spain), that showed undamped flux oscillations during start-up on December 17, 1984 (OECD-NEA, 1986);
- (2) the Caorso BWR (Italy), where two scrams were experienced during the first cycle due to neutron-flux oscillations: one during the start-up and one at the end of the cycle (Gialdi et al., 1985);
- (3) the La Salle BWR (USA), where neutron-flux oscillations were observed quite recently (March 9, 1988). Both recirculation pumps tripped due to a technician's error, after which the core flow decreased to natural circulation (Murphy, 1988; NEI, 1988).

Oscillations have also been reported from experiments in which the coolant flow was decreased purposely (Waaranderä & Andersson, 1981; Sandoz & Chen, 1983).

These experiences emphasize the importance of stability monitoring. Stability monitoring enables plant owners to operate at high reactor power with acceptable stability margins (March-Leuba & King, 1988). Moreover, it gives vital system information during non-nominal reactor conditions, such as during start-up and during load following (Nielsen et al., 1988).

Description of a BWR

The general principle of operation for a BWR is set out in this section, followed by a description of the characteristics of the Dodewaard BWR.

Principle of operation - A simplified description of the main features of a BWR is given here. A more detailed outline can be found in the literature (see, e.g., Lahey & Moody, 1977, or the text-books on nuclear reactors).

The main part of a BWR consists of a steel vessel containing the reactor core in which the nuclear fissions take place (Fig. 1). The core

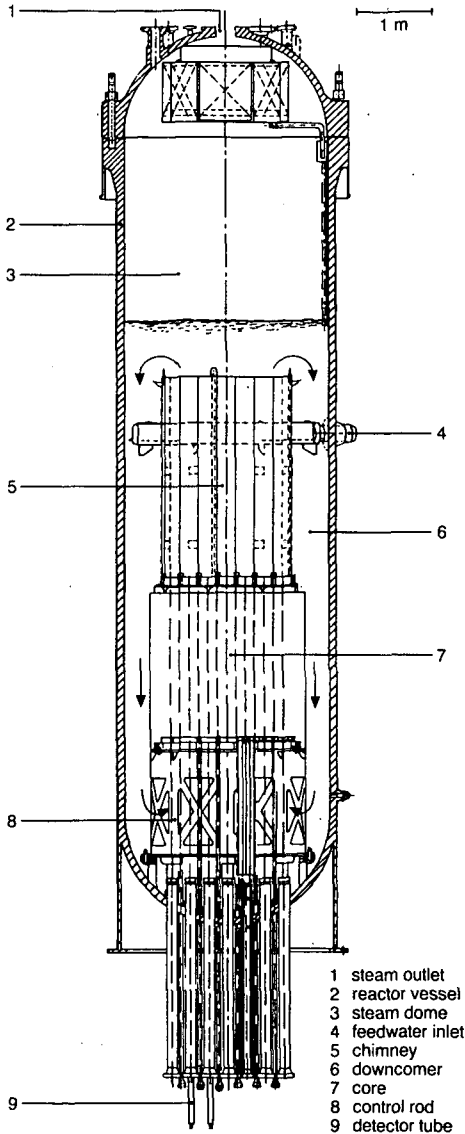


Fig. 1
Cross-section of the Dodewaard BWR vessel.

contains the fissionable fuel, coolant channels, structural components, control rods and instrumentation systems. The fuel consists of a large number of UO₂ ceramic pellets (about 1 cm in diameter) confined in long (approximately 4 m) zircaloy tubes (the fuel rods). A lattice of these rods (typically 8x8) is called a fuel bundle.

Light water, which serves as a coolant and as a moderator to slow down fast neutrons, flows upwards through the core where about 10% is converted into steam as the pressure in the vessel is low enough (about 7 MPa) to cause bulk boiling of the water in the core. The void fraction at the top of the core can be as high as 70%. The steam produced leaves the top of the vessel and is fed directly to the turbine, to generate electricity. The steam from the turbine is passed through a condenser and the condensate is returned to the reactor vessel. The remaining liquid part at the top of the core is returned to the bottom through the so-called downcomer (Fig. 1).

The coolant is pumped through the core by means of circulation pumps (forced circulation) in all but two BWRs in current operation: the Melekes VK50 (Soviet-Union) and the Dodewaard reactor (The Netherlands) (WNIH, 1988), in which the coolant flow is due to the density difference between the fluid in the core and that in the downcomer (natural circulation). An investigation of the characteristics of the latter type of reactor is of importance as new BWR designs using natural circulation are being developed nowadays. The reason for this trend is the decrease in the number of components that leads to improved safety, reliability, operability and maintainability (Kataoka et al., 1988).

The term 'control' rod is somewhat misleading as the power in a BWR is kept constant by controlling the pressure and the recirculation flow through the downcomer or the water level in the vessel. The control rods are used for flux shaping and for burn-up compensation (and, of course, safety aspects).

Characteristics of the Dodewaard reactor - The Dodewaard reactor is a small BWR. It is situated in The Netherlands and has been in operation since 1968. It is cooled by natural circulation. Table 1 gives the main features.

A core cross-section is shown in Figure 2. Radial control-rod and fuel-bundle positions are indicated using the coordinates A to G and 1 to 7 (Fig. 2). The terminology for the detector positions between four fuel bundles corresponds to the coordinates of the fuel bundle at lower left. Three ex-vessel thermal-neutron detectors (Fig. 2) are positioned in the biological shield (almost three metres from the centre of the core). These detectors are designated N5, N6 and N7.

The thirty-seven control rods can be positioned in twenty-three fixed axial positions in the core, numbered from 0 up to 22. An axial position of 0 means a completely inserted rod; whereas a position of 23 denotes a fully

Table 1

Characteristics of the Dodewaard reactor (Oosterkamp, 1987).

licensed thermal power	183	MW
operating pressure	7.5	MPa
saturation temperature	56	K
number of fuel bundles	164	
number of control rods	37	
fuel array	6x6-1	
cladding diameter	13.5	mm
pellet diameter	11.5	mm
fuel stack length	1790	mm
fuel bundle pitch	127	mm
average linear power	17.7	kW.m ⁻¹

withdrawn rod. The distance between two successive axial rod positions is 78.5 mm.

The reactor characteristics were analysed extensively by Kleiss (1983), who applied noise analysis.

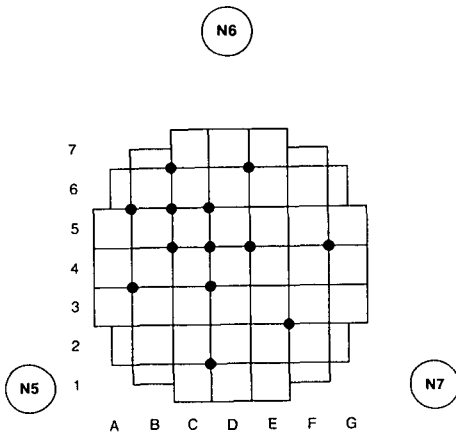


Fig. 2

Top view of the Dodewaard core with the positions of the ex-vessel neutron detectors N5, N6 and N7. The black dots indicate the in-core detector positions.

Stability

Some of the definitions concerning stability that are used in this study are presented below. No attempt was made to provide an exhaustive review on stability analysis. The reader who is not familiar with the analysis of linear systems in the frequency domain is referred to textbooks on classical servo techniques.

Consider a linear single-input/single-output system where the relation between input signal $i(t)$ and output signal $u(t)$ can be written as:

$$\left(a_n \frac{d^n}{dt^n} + a_{n-1} \frac{d^{n-1}}{dt^{n-1}} + \dots + a_0\right)u = \left(b_m \frac{d^m}{dt^m} + b_{m-1} \frac{d^{m-1}}{dt^{m-1}} + \dots + b_0\right)i \quad (\text{Eq. 1})$$

This system is termed stable when the solution of the homogeneous equation

$$\left(a_n \frac{d^n}{dt^n} + a_{n-1} \frac{d^{n-1}}{dt^{n-1}} + \dots + a_0\right)u = 0 \quad (\text{Eq. 2})$$

does not contain components which increase unlimitedly with time. This means that the system is stable when its transfer function in the frequency domain has no poles with a positive real part (a singular pole in the origin points to a stable system as well).

It should be noted that an analysis of the time behaviour of the output signal does not always give a decisive answer to the question of the system's stability: the output signal of a stable system might increase boundlessly due to a constant input signal (for instance, a pure integrator) and an unstable system might (in theory) show a constant output signal due to the absence of components with the resonance frequency in the input signal.

Two parameters are of interest for stability monitoring: the decay ratio of the system and the resonance frequency. The decay ratio is defined as the ratio between two successive maxima of the impulse response and is therefore relevant only for systems showing an oscillatory response such as those presented in Figure 3. It should be stressed here that only a second-order linear system has a constant decay ratio: i.e. the ratio between two successive maxima of the impulse response is constant during the response. When the decay ratio is equal to unity, the response is not damped but oscillates continuously with a constant amplitude; a decay ratio larger than one denotes an unstable system as the response amplitude increases with time.

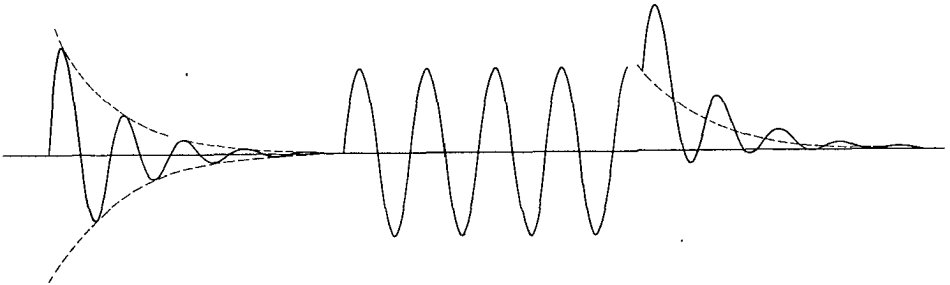


Fig. 3

Oscillatory impulse responses.

Left: complex conjugate poles with a negative real part.

Middle: purely imaginary poles.

Right: complex conjugate poles with a negative real part and a singular negative real pole.

Gradations in stability will also be referred to qualitatively in this study: a system is said to be more stable when the damping of the impulse response is stronger, i.e. when its decay ratio is smaller.

The resonance frequency is the frequency of the oscillating part of the impulse response and should not be confused with the characteristic frequency.

Second-order system - In order to clarify the conceptions mentioned above a second-order system will be treated in more detail. Consider the second-order system

$$\left(\frac{1}{(2\pi f_0)^2} \frac{d^2}{dt^2} + \frac{2\xi}{2\pi f_0} \frac{d}{dt} + 1 \right) u(t) = A i(t) \tag{Eq. 3}$$

where A is the static amplification, f_0 the characteristic frequency and ξ the damping constant.

The transfer function, $H(s)$, where s is the Laplace variable, of this system is

$$H(s) = \frac{A}{\frac{s^2}{(2\pi f_0)^2} + 2\xi \frac{s}{2\pi f_0} + 1} \tag{Eq. 4}$$

The transfer function has two conjugate poles:

$$s = 2\pi f_0[-\xi \pm j\sqrt{1 - \xi^2}] - (0 < \xi < 1) \tag{Eq. 5}$$

The position of the poles in the s -plane is given in Figure 4.

The distance of the real parts of the poles from the imaginary axis is called the rate of decay index σ , which is equal to $-\xi 2\pi f_0$ (see Eq. 5). As mentioned before, a value for σ less than zero denotes a stable system.

The impulse response, $h(t)$, of the system in question is found to be:

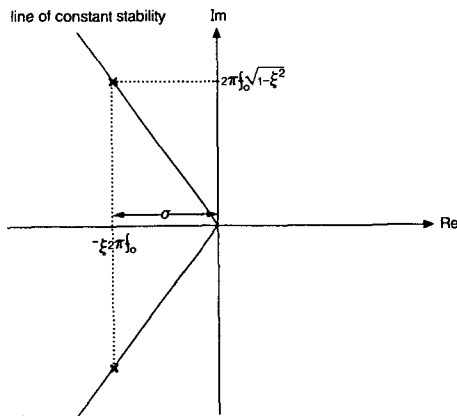


Fig. 4
Position of the two conjugate poles of a damped second-order system.

$$h(t) = \frac{A}{2\pi f_0 \sqrt{1-\xi^2}} \exp(-\xi 2\pi f_0 t) \sin(2\pi f_0 \sqrt{1-\xi^2} t) \quad (\text{Eq. 6})$$

It follows from this equation that the resonance frequency, f_R , is equal to

$$f_R = f_0 \sqrt{1-\xi^2} \quad (\text{Eq. 7})$$

The decay ratio, DR, can easily be derived from Equation (6):

$$\text{DR} = h\left(\frac{5\pi}{4\pi f_0 \sqrt{1-\xi^2}}\right) / h\left(\frac{\pi}{4\pi f_0 \sqrt{1-\xi^2}}\right) = \exp(-2\pi\xi/\sqrt{1-\xi^2}) \quad (\text{Eq. 8})$$

It should be noted that this ratio does not correspond exactly with the ratio between two successive maxima but that Equation (8) is generally used.

Note that

$$\text{DR} = \exp(\sigma/f_R) \quad (\text{Eq. 9})$$

holds. The lines of constant stability in Figure 4 are therefore the lines of a constant ratio of real part to imaginary part.

Stability analysis is of particular interest as regards systems with one or more feedback loops, such as a BWR. Consider for the purpose a system with a block diagram as shown in Figure 5. $H(s)$ is termed the 'forward loop transfer function' and $F(s)$ is termed the 'transfer function of the feedback loop'. The transfer function between input and output signal is

$$\frac{u(s)}{i(s)} = \frac{H(s)}{1-H(s)F(s)} \quad (\text{Eq. 10})$$

This system can obviously be unstable (that is $1-H(s)F(s)$ can have one or more roots with a positive real part) although $H(s)$ and $F(s)$ are stable.

This study is particularly concerned with the different feedback loops in a BWR and with methods for monitoring the stability of the system during normal operation. The decay ratio is a very convenient stability

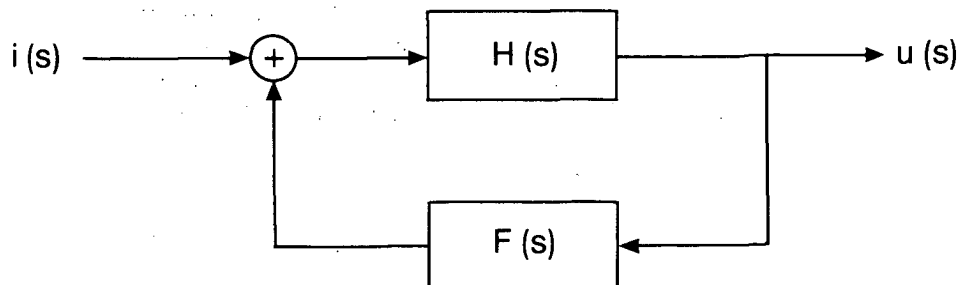


Fig. 5
Block diagram of a system with feedback.

index for the purpose as the response of a BWR to perturbations is of a damped oscillatory type (March-Leuba, 1984).

Stability of a BWR

A BWR is, from a dynamic point of view, a very complex non-linear system. Two parts are usually considered separately:

- (1) the reactor-kinetic part that describes the lock, stock and barrel of the neutrons and the fission process. This part governs the production of heat;
- (2) the thermal-hydraulic part that deals with the two-phase coolant flow through the heated channels. This part governs the removal of heat from the core.

The connection between the two parts lies in the two-fold character of the water/steam-mixture flow through the core. Water serves as a moderator to sustain the fission process (part 1) and as a coolant to transport the heat produced (part 2).

Each part has its own stability characteristics and problems. The process values in a BWR are not constant but fluctuate continuously due to the formation, transport and collapse of steam bubbles. This is on the one hand an advantage as it serves as an intrinsic input source, present during normal operation by means of which the behaviour of the system can be monitored over a large frequency range. On the other hand the fluctuations are a disadvantage as they continually excite the system and drive instabilities (if present).

It was recognized that this noise source has two effects on the signal of an in-core neutron detector (Seifritz & Cioli, 1973). The first effect is formed by the local flux disturbances caused by the steam bubbles; these result in axially correlated variations in the neutron signals as the perturbations are transported upwards. There is no correlation due to this effect between the signals in different coolant channels. This part can be used for in-core coolant-velocity determination (Chapter 3). The second effect is both axially and radially correlated and is the result of the overall (global) influence of moderator variations on the reactivity of the core (reactivity is a measure of the relative deviation from unity of the neutron multiplication factor of the reactor). This second effect occurs only at low frequencies as it is volume-integrated. These two effects led to the introduction of the 'local-global' concept (Wach & Kosaly, 1974). A theoretical basis was developed by Van Dam (1976). It was further elaborated by Behringer et al. (1977) and others.

The above-mentioned intrinsic noise source represents the dynamic status of the thermal-hydraulic part. It serves as an input for the reactor-kinetic part. The final system output is the reactor power, the variations of which are thus formed by the noise source shaped by the reactivity-to-power transfer function (Upadhyaya et al., 1982). To the author's know-

ledge, the feedback from the reactor-kinetic to the thermal-hydraulic part (a change in power results in a different flow pattern with different stability characteristics) has not been incorporated in any theoretical model. The experimental approach is preferred here because of this incompleteness of the dynamic models now available.

A third type of stability is the so-called total-plant stability that involves the dynamic behaviour of the complete reactor, including steam tubes, valves, turbine, etc.

The reactor-kinetic and thermal-hydraulic stability are discussed in more detail in the sections following.

Reactor-kinetic stability - Reactor-kinetic stability is determined by the reactivity-to-power transfer function which is defined as the transfer function between variations in reactivity and variations in power. The reactivity-to-power transfer function contains the zero-power reactivity-to-power transfer function (which is a stable system) combined with three negative feedback loops: via fuel temperature (Doppler effect), via void fraction and via moderator temperature (Figure 6). The sign of the last two feedback mechanisms depends on the design of the reactor but is almost invariably taken to be negative (a so-called under-moderated reactor). Changes of reactivity caused by, for instance, changes in the void fraction result in changes in power which in turn result in reactivity changes of opposite sign. Thus, the system is stable in principle. Less stable behaviour is due to the various time constants in the feedback mechanisms which cause phase changes.

March-Leuba (1986) has shown, by fitting the calculated reactivity-to-power transfer function, that a model for this function needs at least two negative real poles and a pair of complex conjugate poles.

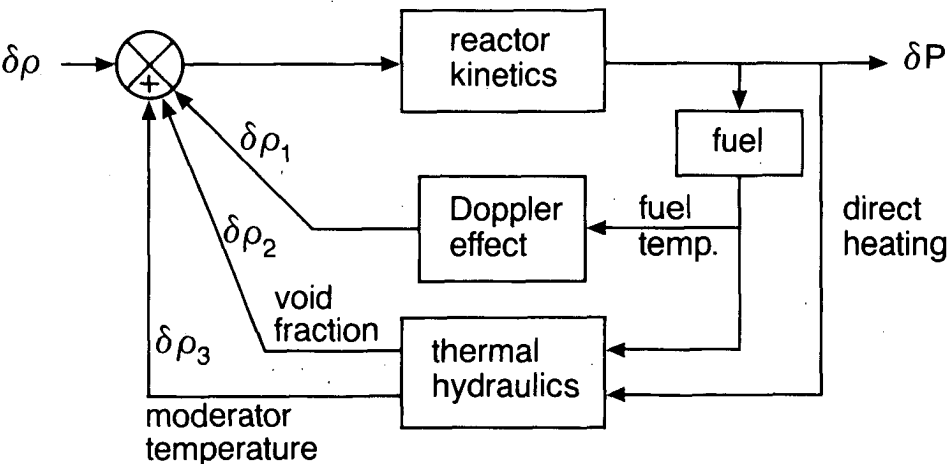


Fig. 6 Block diagram of the reactivity-to-power transfer function.

Thermal-hydraulic stability – The dynamic behaviour of two-phase flow through heated channels with a complex geometry involves a very cumbersome aspect of physics.

Only the most important types of instabilities recognized (Lahey & Moody, 1977) are treated here. They are (1) flow-pattern instability, (2) channel-flow instability and (3) recirculation instability. A detailed review can be found in the studies by Neal & Zivi (1967) and Bouré et al. (1973).

(1) Flow-pattern instability.

The flow pattern in a BWR coolant channel covers the entire flow patterns from bubbly flow up to annular flow. These flow types are not themselves unstable, although they can be periodic (slug flow). The transition from one flow pattern to another, however, can induce unstable behaviour due to the fact that the latter flow type can have a higher slip factor (i.e. steam velocity to water velocity ratio) (Lahey & Moody, 1977); the void fraction will decrease in this case and the flow will resume its original pattern.

(2) Channel-flow instability.

Channel-flow instability is the most important type of instability for BWR technology (Bouré et al., 1973; Lahey & Moody, 1977). This feature has therefore been examined thoroughly, both experimentally in test tubes and theoretically. It results in flow oscillations in one or more coolant channels. The oscillations in different channels can be either independent - in which case the downcomer flow will oscillate as well - or dependent and in counterphase (the downcomer flow is constant).

The most important type is the so-called density-wave instability, which can be described in a number of equivalent ways and which is caused by the multiple feedbacks between flow rate, steam-generation rate and pressure drop (Bouré et al., 1973). The influence of several parameters on this type of instability has been investigated; a shorter channel length, an increase in inlet resistance, a decrease in outlet resistance, inlet subcooled boiling, a pressure increase, power decrease and flow-rate increase all stabilize the flow. A change of the heat-flux distribution can either increase or reduce stability (Bouré et al., 1973).

(3) Recirculation instability.

This type of instability concerns the complete loop via the downcomer back to the core. Instabilities can occur due to the interaction between the driving force of the downcomer and the flow resistance in the core.

Scope of this study

This study encompasses experimental methods for on-line monitoring of the stability of a BWR during normal operation. Experiments for the

purpose were performed on the Dodewaard reactor, together with theoretical analyses. Normal reactor instrumentation was applied, as well as so-called twin detectors of own design and fabrication, by means of which in-core coolant velocity could be measured. Variations of this velocity reflect the thermal-hydraulic stability of the local channel flow.

The sensitivity of a detector signal to a flux perturbation at a certain position in the core - essential for proper stability monitoring - depends on the distance from the source to the detector and on core conditions. These aspects are incorporated in the so-called field-of-view of the detector (Van Dam, 1976). A theoretical analysis of this item is therefore included in the present study.

Part of the research presented deals with the fuel time constant, as this is a major parameter in the feedback loops of the reactivity-to-power transfer function and is thus of importance to the gain and the phase of the reactivity feedback. It has been shown by Kleiss & Van Dam (1985) that the dynamic behaviour of the reactor indeed depends on the value of this constant. Moreover, use of the fuel time constant in numerical models is controversial.

Outline - The next section presents the results of a theoretical analysis of the field-of-view of in-core and ex-vessel neutron detectors. This analysis makes it possible to determine the number of this type of detector necessary for monitoring the entire core.

Chapter 3 introduces the well-known technology for measuring the coolant velocity by noise analysis. The physical interpretation of the measured velocity is discussed in Chapter 4 which presents the results of experiments performed on a model of a BWR coolant channel. An entirely new method for monitoring the channel-flow stability is presented in Chapter 5. This latter method deals with the variations of the in-core coolant velocity. An increase in these variations reflects a decrease in stability.

Chapter 6 deals with the determination of the three types of stability of the Dodewaard reactor under different conditions by means of perturbation tests and noise analyses.

The effective value of the fuel time constant is considered both experimentally and theoretically in Chapter 7. This constant is important to reactor-kinetic stability because it is a dominant factor in the feedback loops (Figure 6).

Chapter 8 introduces a simple yet reliable measure for the stability of the reactor. This measure can be derived on-line from the ex-vessel neutron noise.

Finally, in Chapter 9, the methods presented for stability monitoring by means of the ex-vessel neutron flux and the in-core coolant velocity variations are applied under various conditions of the Dodewaard reactor core.

Chapter 2

The frequency-dependent field-of-view of a neutron detector

In order to insure proper stability monitoring, it is of importance to know the sensitivity of the neutron detectors used to in-core neutron-flux perturbations. The so-called field-of-view (hereafter called FOV) of the detector forms a weighting factor for flux variations. It is a function of the frequency of the variation and of the position of the detector and the source. A large FOV will result in the integration of local effects whereas a small FOV impedes surveillance of the entire core.

The results of calculations of the FOV of an ex-vessel and of an in-core neutron detector in the Dodewaard reactor are presented below. Use is made of a firm theoretical basis which was developed earlier (Van Dam, 1976), using the adjoint function technique (Bell & Glasstone, 1970) which has proved very successful (Behringer et al., 1977, 1979; Kleiss & Van Dam, 1981b).

Numerical model

The theory proposed for calculation of the detector FOV (Van Dam, 1976) is outlined below. It is subsequently shown that the calculations can be performed by a normal neutron-diffusion code.

Theory - Variations in the signal of a neutron detector are assumed to arise from small changes of the macroscopic cross-sections in the core. These changes, caused e.g. by the formation and transport of steam bubbles, are called 'parametric changes' as the cross-sections appear as parameters in the neutron-transport equations. The changes result in small fluctuations, $\delta\phi$ and δC_k , of the neutron flux and the concentration of delayed-neutron precursors of group k .

As the neutrons in a reactor have energies ranging from 10 MeV down to 0.01 eV and as the nuclear cross-sections are very sensitive to the incident neutron energy, the energy is usually divided into groups and flux-weighted average cross-sections are used for each group. The n -group diffusion equation for energy group i reads, in conventional notation:

$$\begin{aligned}
& -\frac{1}{v_i} \frac{\partial \phi_i}{\partial t} + \nabla \cdot D_i \nabla \phi_i - \Sigma_{a,i} \phi_i - \sum_{j \neq i}^n \Sigma_{s,ij} \phi_j + \chi_i (1 - \beta) \nu \Sigma_{f,i} \phi_i + \sum_k \chi_{ik} \lambda_k C_k + \\
& + \sum_{j \neq i}^n \{ \Sigma_{s,ji} \phi_j + \chi_i (1 - \beta) \nu \Sigma_{f,j} \phi_j \} = -S_i
\end{aligned} \tag{Eq. 11}$$

$$\frac{\partial C_k}{\partial t} = \beta_k \sum_j \nu \Sigma_{f,j} \phi_j - \lambda_k C_k \tag{Eq. 12}$$

where Σ denotes the summation over the delayed-neutron precursors.

The reader who is unfamiliar with the notations presented here is referred to Appendix 3; a detailed description of the derivation of Equations (11) and (12) can be found in Duderstadt & Hamilton (1976) among other references.

The adjoint function, ϕ^+ , can be derived, after Laplace transformation and combination of Equations (11) and (12), by taking the adjoint equation

$$\begin{aligned}
& \left(-\frac{s}{v_i} + \nabla \cdot D_i \nabla - \Sigma_{a,i} - \sum_{j \neq i}^n \Sigma_{s,ij} + \chi_i (1 - \beta) \nu \Sigma_{f,i} + \sum_k \chi_{ik} \frac{\beta_k \lambda_k}{s + \lambda_k} \nu \Sigma_{f,i} \right) \phi_i^+ + \\
& + \sum_{j \neq i}^n \left(\Sigma_{s,ij} + \chi_j (1 - \beta) \nu \Sigma_{f,i} + \sum_k \chi_{jk} \frac{\beta_k \lambda_k}{s + \lambda_k} \nu \Sigma_{f,i} \right) \phi_j^+ = -\Sigma_{d,i}
\end{aligned} \tag{Eq. 13}$$

where $\Sigma_{d,i}$ is the detector cross-section for energy group i .

The physical meaning of ϕ^+ can be shown by a first-order single group approximation (thus only valid for small parametric fluctuations). In the analysis of parametric fluctuations caused by, for instance, the formation of steam bubbles, the neutron source S is formed by $\delta \Sigma_a \phi$ and $\nabla \cdot \delta D \nabla \phi$, which give rise to flux variations $\delta \phi$ (the variations in $\nu \Sigma_f$ due to spectral fluctuations are neglected here). Insertion of this source term in Equations (11) and (12), Laplace transformation and multiplication of the result by ϕ^+ and of Equation (13) by $\delta \phi$ gives:

$$\delta R = \int_V dV \Sigma_d \delta \phi = - \int_V dV \{ \delta \Sigma_a \phi \phi^+ + \delta D \nabla \phi \cdot \nabla \phi^+ \} \tag{Eq. 14}$$

for the variation of the detector signal δR (neglecting the second-order terms $\delta \phi \delta \Sigma_a$ and $\delta \phi \delta D$). This representation of the response of a neutron detector in the frequency domain instead of the time domain is preferred because the parametric fluctuations are stochastic. It can be observed from Equation (14) that ϕ^+ can be considered as describing the field-of-view of the detector. It is a complex function that is dependent on the position of the detector - through the distribution of Σ_d - and on the frequency of the parametric fluctuations via the Laplace variable, s . The great advantage of using the adjoint equation instead of the forward equation is that the response of a detector can be determined for each source distribution in a single calculation.

The analogon of Equation (14) for the n-group analysis is

$$\begin{aligned} \delta R &= \int_V dV \sum_{i=1}^n \{ \Sigma_{d,i} \delta \phi_i \} = \\ &= - \int_V dV \sum_{i=1}^n \left\{ \delta \Sigma_{a,i} \phi_i \phi_i^+ + \phi_i^+ \sum_{j=1}^n (\delta \Sigma_{s,ij} \phi_j - \delta \Sigma_{s,ji} \phi_j) \right\} \end{aligned} \quad (\text{Eq. 15})$$

where the terms containing the gradient of the flux, ϕ_i , and the gradient of the FOV, ϕ_i^+ , (which are weighting factors for variations of the diffusion coefficient) are neglected as these are small in large reactor cores. Separation of ϕ_i into its real and its imaginary part leads to a set of equations that have the same structure as the multi-group diffusion equation (11). Substitution of $\phi_i^+ = \psi_i - j\eta_i$ and $s = j\omega$ in Equation (13) yields two sets of equations, one for the real and one for the imaginary part:

$$\begin{aligned} & \left(\nabla \cdot D_i \nabla - \Sigma_{a,i} - \sum_{j \neq i} \Sigma_{s,ij} + \chi_i (1 - \beta) v \Sigma_{f,i} + \sum_k \chi_{ik} \frac{\beta_k \lambda_k^2}{\lambda_k^2 + \omega^2} v \Sigma_{f,i} \right) \psi_i + \\ & + \left(- \frac{\omega}{v_i} - \sum_k \chi_{ik} \frac{\beta_k \lambda_k \omega}{\lambda_k^2 + \omega^2} v \Sigma_{f,i} \right) \eta_i + \\ & + \sum_{j \neq i} \left(\Sigma_{s,ij} + \chi_j (1 - \beta) v \Sigma_{f,i} + \sum_k \chi_{jk} \frac{\beta_k \lambda_k^2}{\lambda_k^2 + \omega^2} v \Sigma_{f,i} \right) \psi_j + \\ & - \sum_{j \neq i} \sum_k \chi_{jk} \frac{\beta_k \lambda_k \omega}{\lambda_k^2 + \omega^2} v \Sigma_{f,i} \eta_j = - \Sigma_{d,i} \end{aligned} \quad (\text{Eq. 16a})$$

and

$$\begin{aligned} & \left(\nabla \cdot D_i \nabla - \Sigma_{a,i} - \sum_{j \neq i} \Sigma_{s,ij} + \chi_i (1 - \beta) v \Sigma_{f,i} + \sum_k \chi_{ik} \frac{\beta_k \lambda_k^2}{\lambda_k^2 + \omega^2} v \Sigma_{f,i} \right) \eta_i + \\ & + \left(\frac{\omega}{v_i} + \sum_k \chi_{ik} \frac{\beta_k \lambda_k \omega}{\lambda_k^2 + \omega^2} v \Sigma_{f,i} \right) \psi_i + \\ & + \sum_{j \neq i} \left(\Sigma_{s,ij} + \chi_j (1 - \beta) v \Sigma_{f,i} + \sum_k \chi_{jk} \frac{\beta_k \lambda_k^2}{\lambda_k^2 + \omega^2} v \Sigma_{f,i} \right) \eta_j + \\ & - \sum_{j \neq i} \sum_k \chi_{jk} \frac{\beta_k \lambda_k \omega}{\lambda_k^2 + \omega^2} v \Sigma_{f,i} \psi_j = 0 \end{aligned} \quad (\text{Eq. 16b})$$

Equations (16a) and (16b) can be written as a set of $2n$ normal neutron-diffusion equations by adjusting the coefficients (the new coefficients are written with a plus sign (+) as a superscript):

$$\left(\nabla \cdot D_i^+ \nabla - \Sigma_{a,i}^+ - \sum_{j \neq i} \Sigma_{s,ij}^+ + \chi_i^+ v \Sigma_{f,i}^+ \right) \theta_i^+ + \sum_{j \neq i} \left(\Sigma_{s,ji}^+ + \chi_j^+ v \Sigma_{f,j}^+ \right) \theta_j^+ = -S_i^+ \quad (\text{Eq. 17})$$

where: $\theta_{2i-1}^+ = \psi_i$ and $\theta_{2i}^+ = \eta_i$.

Equation (17) is equivalent to Equations (16a) and (16b) when the fictitious cross-sections are taken to be:

$$D^{+2i-1} = D^{+2i} = D_i \quad (\text{Eq. 18})$$

$$S^{+2i-1} = \Sigma_{d,i}, S^{+2i} = 0 \quad (\text{Eq. 19})$$

The choice of the 'fission cross-sections' and the 'absorption cross-sections' is not unambiguously fixed. Only their difference is predetermined:

$$\begin{aligned} v\Sigma_{f,2i-1}^{+} - \Sigma_{a,2i-1}^{+} &= \sum_j (\Sigma_{s,ji} - \Sigma_{s,ij}) + \\ &+ \left\{ \chi_i(1-\beta) + \sum_k \chi_{ik} \frac{\beta\lambda_k(\lambda_k + \omega)}{\lambda_k^2 + \omega^2} \right\} \sum_j v\Sigma_{f,j} + \frac{\omega}{v_i} - \Sigma_{a,i} \end{aligned} \quad (\text{Eq. 20a})$$

$$\begin{aligned} v\Sigma_{f,2i}^{+} - \Sigma_{a,2i}^{+} &= \sum_j (\Sigma_{s,ji} - \Sigma_{s,ij}) + \\ &+ \left\{ \chi_i(1-\beta) + \sum_k \chi_{ik} \frac{\beta\lambda_k(\lambda_k + \omega)}{\lambda_k^2 + \omega^2} \right\} \sum_j v\Sigma_{f,j} - \frac{\omega}{v_i} - \Sigma_{a,i} \end{aligned} \quad (\text{Eq. 20b})$$

One degree of freedom remains for the 'fission spectrum' as well. It is required that

$$0 \leq \chi_j^{+} \leq 1 \text{ and } \sum_{j=1}^{2n} \chi_j^{+} = 1$$

Thus a factor q , expressing this degree of freedom, is introduced:

$$X^{+2i-1} = (1 - q_i)X_i, X^{+2i} = q_iX_i \quad (\text{Eq. 21})$$

where $0 \leq q_i \leq 1$.

Once the 'fission spectrum' is chosen according to Equation (21), there follows for the 'scattering cross-sections' that

$$\Sigma_{s,2i-1,2j-1}^{+} = \Sigma_{s,ji} + \left\{ \chi_i(1-\beta) + \sum_k \chi_{ik} \frac{\beta\lambda_k^2}{\lambda_k^2 + \omega^2} \right\} v\Sigma_{f,j} - (1-q_j)\chi_j v\Sigma_{f,2i-1}^{+} \quad (\text{Eq. 22a})$$

$$\Sigma_{s,2i,2j}^{+} = \Sigma_{s,ji} + \left\{ \chi_i(1-\beta) + \sum_k \chi_{ik} \frac{\beta\lambda_k^2}{\lambda_k^2 + \omega^2} \right\} v\Sigma_{f,j} - q_j\chi_j v\Sigma_{f,2i}^{+} \quad (\text{Eq. 22b})$$

$$\Sigma_{s,2i-1,2j}^{+} = \sum_k \chi_{ik} \frac{\beta\lambda_k\omega}{\lambda_k^2 + \omega^2} v\Sigma_{f,j} + \frac{\omega}{v_i} \delta_{ij} - q_j\chi_j v\Sigma_{f,2i-1}^{+} \quad (\text{Eq. 22c})$$

$$\Sigma_{s,2i,2j-1}^{+} = - \sum_k \chi_{ik} \frac{\beta\lambda_k\omega}{\lambda_k^2 + \omega^2} v\Sigma_{f,j} - \frac{\omega}{v_i} \delta_{ij} - (1-q_j)\chi_j v\Sigma_{f,2i}^{+} \quad (\text{Eq. 22d})$$

The above-mentioned degrees of freedom are of importance for the convergence rate of the computer code to be used. The balance between $v\Sigma_f^{+}$ and Σ_a^{+} strongly influences the multiplication factor k_{eff}^{+} of the (pseudo) system and thus convergence. Notice that the new coefficients can have any sign or magnitude and are a function of the radial frequency, ω . This can result in $k_{\text{eff}}^{+} < 1$ (even < 0) or $k_{\text{eff}}^{+} > 1$ (k_{eff}^{+} is also a function of ω). For small ω , the equations are nearly dependent and

vergence is therefore very low (only n independent in for $\omega = 0$).

optimal convergence, k_{eff}^+ was set to a very small quantity $^+,_{2i-1} = v\Sigma_{f^+}^+,_{2i} = 10^{-6} \text{ cm}^{-1}$ ($v\Sigma_{f^+}^+$ may not be set equal to positions and for each energy group in the computer code relating $\Sigma_a^+,_{2i-1}$ and $\Sigma_a^+,_{2i}$ from Equations (20a) and (20b).

ial cross-sections in diffusion calculations - The justification-conventional (for instance negative) cross-sections in before calculation of the FOV for the Dodewaard situation. The diffusion code used for the calculations is EXTER-

MINATOR-II (Fowler et al., 1967). This code was selected, because it does not have an internal protection for the occurrence of negative neutron fluxes, which is a shortcoming in the case of normal applications but which suits our purpose because the real part of the FOV is likely to change signs at large distances and high frequencies (phase changes larger than 90°).

Verification was done by considering the following, hypothetical, homogeneous infinite-plate reactor of extrapolated thickness a ($= 70 \text{ cm}$). Neutrons are generated in this artificial, somewhat strange reactor in the first group by fission (as in a fast reactor) and by a fixed neutron source. The neutrons are then slowed down to the second group (the lowest group number denotes the group of neutrons with the highest energy and vice versa, as is conventional). Up-scattering is neglected here. This reactor type was selected in order to allow a simple analytical derivation. The neutron-diffusion equations can be written as

$$D_1 \frac{d^2 \phi_1}{dx^2} - \Sigma_{a,1} \phi_1 - \Sigma_{s,12} \phi_1 + v\Sigma_{f,1} \phi_1 = -S(x) \quad (\text{Eq. 23a})$$

$$D_2 \frac{d^2 \phi_2}{dx^2} - \Sigma_{a,2} \phi_2 + \Sigma_{s,12} \phi_1 = 0 \quad (\text{Eq. 23b})$$

with $S(x)$ being a plate neutron source with value S for $-\frac{1}{2}b < x < \frac{1}{2}b$ and value 0 for all other conditions ($b = 1 \text{ cm}$). The reactor is subcritical in order to make a stationary solution possible.

The solution of the homogeneous diffusion equation for the first group can be written as a summation of weighted eigenfunctions, Φ_n

$$\phi_1(x) = \sum_{n \text{ odd}} A_n \Phi_n(x) \quad (\text{Eq. 24})$$

For the eigenfunctions (using the boundary condition $\phi(\pm a/2) = 0$) holds

$$\Phi_n = \cos\left(\frac{n\pi x}{a}\right) \quad (n = 1, 3, 5, \dots) \quad (\text{Eq. 25})$$

Once the neutron source is developed into eigenfunctions

$$S(x) = \sum_{n \text{ odd}} S_n \Phi_n(x) \quad (\text{Eq. 26})$$

with

$$S_n = \frac{4S}{n\pi} \sin\left(\frac{n\pi b}{2a}\right) \quad (\text{Eq. 27})$$

the coefficients A_n can be calculated. Finally

$$\phi_1 = \sum_{n \text{ odd}} A_n \Phi_n = \frac{4S}{\pi D_1} \sum_{n \text{ odd}} \frac{\sin\left(\frac{n\pi b}{2a}\right)}{n(B_n^2 - B_m^2)} \cos(B_n x) \quad (\text{Eq. 28})$$

with

$$B_n = \frac{n\pi}{a} \quad (n = 1, 3, 5, \dots) \quad (\text{Eq. 29})$$

$$B_m^2 = \frac{\nu \Sigma_{f,1} - \Sigma_{a,1} - \Sigma_{s,12}}{D_1} \quad (\text{Eq. 30})$$

The solution of the second group (Eq. 23b) can be written as a sum of eigenfunctions as well:

$$\phi_2 = \sum_n a_n \cos\left(\frac{n\pi x}{a}\right) \quad (\text{Eq. 31})$$

where a_n follows from the substitution of Equation (28) into Equation (23b). Finally:

$$\phi_2 = \frac{4S \Sigma_{s,12}}{\pi D_1 \Sigma_{a,2}} \sum_{n \text{ odd}} \frac{\sin\left(\frac{n\pi b}{2a}\right)}{(1_n^2 + B_n^2 L_2^2) n (B_n^2 - B_m^2)} \cos(B_n x) \quad (\text{Eq. 32})$$

with

$$L_2^2 = \frac{D_2}{\Sigma_{a,2}} \quad (\text{Eq. 33})$$

Equations (23a) and (23b) were solved by EXTERMINATOR-II in order to check the correctness of the computer calculations. The results were compared with the analytical solutions presented in Equations (28) and (32).

The following conditions were considered:

- (1) normal conditions: $D_1 = 13.2$ cm, $D_2 = 1.0$ cm, $\Sigma_{a,1} = 0.1$ cm⁻¹, $\Sigma_{a,2} = 0.1$ cm⁻¹, $\nu \Sigma_{f,1} = 0.32$ cm⁻¹, $\Sigma_{s,12} = 0.2$ cm⁻¹, $S = 1.0$ cm⁻³·s⁻¹. Thus

$$k_\infty = \frac{\nu \Sigma_{f,1}}{\Sigma_{a,1} + \Sigma_{s,12}} = 1.07 \quad (\text{Eq. 34})$$

$$k_{\text{eff}} = \frac{v\Sigma_{f,1}}{D_1(\pi/a)^2 + \Sigma_{a,1} + \Sigma_{s,12}} = 0.9798 \quad (\text{Eq. 35})$$

- (2) as (1) but $\Sigma_{a,1} = 0.5$ and $\Sigma_{s,12} = -0.2$ (thus $\phi_2 < 0$);
(3) as (1) but $\Sigma_{a,1} = -0.1$ and $\Sigma_{s,12} = 0.4$;
(4) as (1) but $v\Sigma_{f,1} = -0.3$ and $\Sigma_{a,1} = -0.52$ (equations identical to situation (1));
(5) as (1) but $D_2 = -0.1$, $\Sigma_{a,1} = 0.5$, $\Sigma_{s,12} = -0.2$ and $\Sigma_{a,2} = -0.1$;
(6) as (1) but $S = -1.0$.

All calculations gave satisfactory results except for case (6): the maximum difference between numerical and analytical solutions was always less than 0.5% within 300 iterations. It is therefore permitted to use negative cross-sections as long as the fixed neutron source is positive.

A second item to be dealt with here is the calculation for a system in which the flux changes signs as a function of position (the real part of the FOV is likely to change signs at high frequencies as the phase change can be larger than 90° at large distances from the detector). The same plate reactor as used earlier, but with different properties, is considered for the purpose:

$$D_1 \frac{d^2\phi_1}{dx^2} - \Sigma_{a,1}\phi_1 - \Sigma_{s,12}\phi_1 + v\Sigma_{f,1}\phi_1 = -S(x) \quad (\text{Eq. 36a})$$

$$D_2 \frac{d^2\phi_2}{dx^2} - \Sigma_{a,2}\phi_2 + \Sigma_{s,12}\phi_1 = -S(x) \quad (\text{Eq. 36b})$$

with $\Sigma_{s,12} < 0$.

The physical interpretation of this system requires the use of imagination: negative 'neutrons' are scattered from the first to the second group. The solution of the first group in this case is again independent of that of the second group, which enables a simple derivation of the analytical solution. The second group has a positive neutron source via S and a negative source via the negative down scattering $\Sigma_{s,12}\phi_1$. ϕ_2 will therefore be less than zero at a large distance from the fixed source.

The analytical method for solving this set of equations is equivalent to the method applied for Equations (23a) and (23b). As Equation (36a) is identical to Equation (23a), the solution of the first group is given by Equations (28)-(30).

$$\phi_2 = \frac{4S}{\pi\Sigma_{a,2}} \sum_{n \text{ odd}} \frac{\sin\left(\frac{n\pi b}{2a}\right)}{n(1+B_n^2L_2^2)} \left(1 + \frac{\Sigma_{s,12}}{D_1(B_n^2 - B_m^2)}\right) \cos(B_n x) \quad (\text{Eq. 37})$$

is derived for the second group. The calculations were performed with $D_1 = D_2 = 13.2$ cm, $\Sigma_{a,1} = 0.305$ cm⁻¹, $\Sigma_{a,2} = 0.1$ cm⁻¹, $\Sigma_{s,12} = -0.005$ cm⁻¹ and $v\Sigma_{f,1} = 0.32$ cm⁻¹ (for these conditions, ϕ_2 changes signs at $x = 12.37$ cm). The solution calculated with EXTERMINATOR-II agreed perfectly

well with that from Equations (28) and (37). It is thus shown that this computer code can handle neutron fluxes that change signs as a function of distance from the source.

Calculations on the field-of-view of Dodewaard detectors

This subsection deals with four aspects:

- (1) phase behaviour of the field-of-view,
- (2) two-dimensional modelling,
- (3) the field-of-view of an in-core detector,
- (4) the field-of-view of an ex-vessel detector.

Phase behaviour of the field-of-view - Insight into the phase behaviour of the FOV of a detector can be gained by a simple analysis using point reactor kinetics. Volume-averaged parameters (the so-called lumped parameters) are used in this model and spatial effects are incorporated in a shape factor, the fundamental mode. This is the flux shape under stationary conditions. It is assumed that the spatial flux shape does not change with time.

The fundamental mode is derived from the eigenvalue equation

$$\nabla^2\phi(x) + B_g^2\phi(x) = 0 \quad (\text{Eq. 38})$$

where B_g^2 is dependent on the core geometry. B_g^2 is conventionally called the geometric buckling as it is a measure of the curvature of the fundamental mode. Using this technique, the following is derived from Equation (13) for the single energy group situation with one group of delayed neutrons:

$$\phi^+ = \Sigma_d / \left(\frac{s}{v} + DB_g^2 + \Sigma_a - (1 - \beta)v\Sigma_f - \frac{\beta\lambda}{s + \lambda} v\Sigma_f \right) \quad (\text{Eq. 39})$$

It should be noted that the relation of Σ_d and ϕ^+ is identical to the source transfer function, being the transfer function between variations of a neutron source and variations of neutron density (except for a factor v which enters Eq. (39) due to the relation between flux and neutron density). The source transfer function in turn is equal to Λ times the zero-power reactivity-to-power transfer function, with Λ being the neutron-generation time $[= 1/(v\Sigma_f)]$.

Using $DB_g^2 + \Sigma_a = v\Sigma_f$ (as the core is assumed to be critical), the phase behaviour of the FOV follows from Equation (39):

$$\text{phase}(\phi^+) = -\arctan\left(\frac{\beta\lambda + \lambda^2\Lambda + \Lambda\omega^2}{\beta\omega}\right) \quad (\text{Eq. 40})$$

This is of course identical to the phase behaviour of the zero-power reactivity-to-power transfer function.

Figure 7 displays the phase behaviour of ϕ^+ for the Dodewaard reactor where $\Lambda = 35 \mu\text{s}$, $\beta = 0.62\%$ and $\Lambda = 0.0767 \text{ s}^{-1}$. It should be noted from Equation (40) and from this figure that the system behaves like a first-order system with a 90° phase lag for both low and high frequencies (an integrator and a differentiator, respectively). The phase change between event and variations of the detector signal is approximately -90° for high frequencies due to the generation time of neutrons. The phase change is close to -90° for low frequencies, also due to the influence of the delayed neutrons.

The physical reality of this point model can be extended by adding a phase change purely due to spatial effects. Use of the neutron-wave concept of Beckurts & Wirtz (1964) yields for the variation of the flux $\delta\phi$ caused by a mono-energetic sinusoidally modulated neutron point source δQ in a homogeneous multiplying infinite medium at a distance r from the source,

$$\delta\phi(r, t) = \frac{\delta Q}{4\pi r D} \exp(-r/L_\omega) \cdot \exp(j\omega t) \quad (\text{Eq. 41})$$

with

$$\frac{1}{L_\omega} = \sqrt{\frac{1}{D} \left(\Sigma_a - v\Sigma_f + \frac{j\omega}{v} \right)} \quad (\text{Eq. 42})$$

Thus, for a non-multiplying system ($v\Sigma_f = 0$), there holds for the phase lag between δQ and $\delta\phi$ (using a first-order approximation for L_ω , which is valid for low frequencies ($v\Sigma_a = 2.7 \cdot 10^4 \text{ s}^{-1}$ for the Dodewaard core))

$$\text{phase}(r, \omega) = - \frac{r\omega}{2v\sqrt{D\Sigma_a}} \quad (\text{Eq. 43})$$

It holds for a critical system ($\Sigma_a = v\Sigma_f$) that

$$\text{phase}(r, \omega) = - r \sqrt{\left(\frac{\omega}{2vD} \right)} \quad (\text{Eq. 44})$$

The phase lag due to spatial effects therefore increases with frequency and distance from the source as expected.

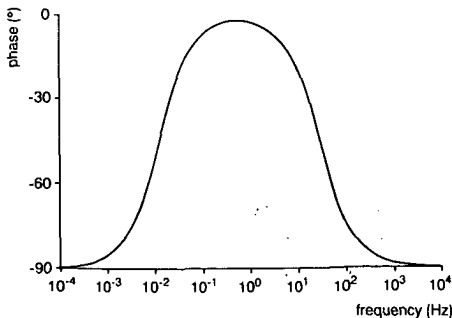


Fig. 7
Phase behaviour of the field-of-view of an in-core detector, calculated by using point reactor kinetics.

Figure 8 shows the total phase change in a critical system as a function of frequency for various detector-source distances ($\nu = 1.6 \cdot 10^6 \text{ cm} \cdot \text{s}^{-1}$, $D = 0.987 \text{ cm}$). The system dynamics are incorporated in Equation (40), whereas spatial effects are described by Equation (44).

The phase difference between the signals of two spatially separated detectors can be calculated by using only the spatial effect (Eq. 44). The phase behaviour for various distances between two neutron detectors is shown in Figure 9. It is obvious from this figure that the phase change is small at the frequencies of interest for BWR cores (below 100 Hz), which is in agreement with the numerous experimental results presented elsewhere.

Two-dimensional modelling - The FOVs of an ex-vessel and an in-core neutron detector in the Dodewaard reactor were calculated by means of the EXTERMINATOR-II computer code (Fowler et al., 1967). This code can solve the multi-group diffusion equation in a two-dimensional geometry.

It should be noted that thermal-hydraulic feedback mechanisms - that have a strong influence on system behaviour for low frequencies - are not incorporated in the analysis presented here.

As in the study by Kleiss (1983), the Dodewaard core and its reflector were modelled by an X-Y square geometry with a 63.5 mm mesh width (i.e. half a fuel-bundle width), except for the ex-vessel detector region where the mesh width was 0.5 mm. Figure 10 illustrates the geometry used. The extreme corners of the square geometry are filled with strongly

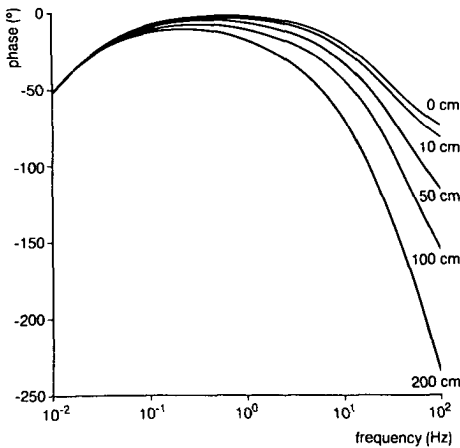


Fig. 8
Phase behaviour of the field-of-view of an in-core detector for several source-detector distances, calculated using a combination of point reactor kinetics and neutron-wave theory.

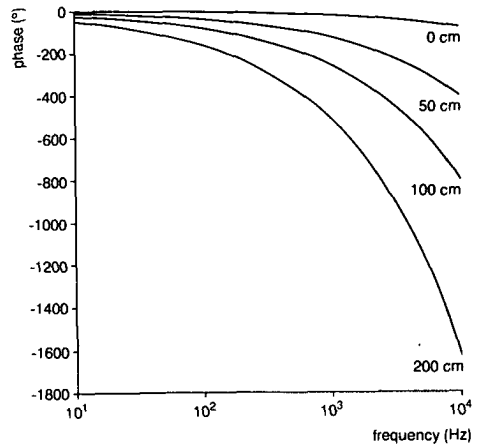


Fig. 9
Phase change between the signals of two in-core detectors for several distances, using neutron-wave theory.

absorbing concrete (region 3 in Fig. 10), as the core with its reflector (region 4 in Fig. 10) has a more or less cylindrical shape. The actual geometry had to be strongly simplified for the introduction of the ex-vessel neutron detector N6 which is positioned in the biological shield almost 3 m outside the centre of the core. As in the study by Kleiss (1983), it was modelled by a plate detector in the reflector (region 2 in Fig. 10). This representation of N6 was chosen to allow neutrons escaping from the six fuel bundles facing N6 to have an equal chance of reaching N6, more than two metres away.

The actual phase of the FOV of N6 was hardly affected as the region between reflector and detector is filled with air and 217 mm steel, which have a negligible effect on the phase. It can be calculated from Equation (43) that the phase change in steel for fluctuations of 1 Hz is equal to 0.003 degrees per centimetre. The actual water gap between core wall and detector averages 324 mm instead of the 127 mm used here. The effect on the phase is again negligible: the phase change in water of 558 K is equal to 0.012 degrees per centimetre (for 1 Hz).

Axial leakage effects were taken into account by introducing an axial buckling. Two-group calculations (group 1: 10 MeV-0.625 eV; group 2: 0.625-0. eV) were performed on a core with an average void fraction of 35%. The various fuel bundles with different burn-up states were modelled by sixteen different, homogeneous compositions. The cell calculations -

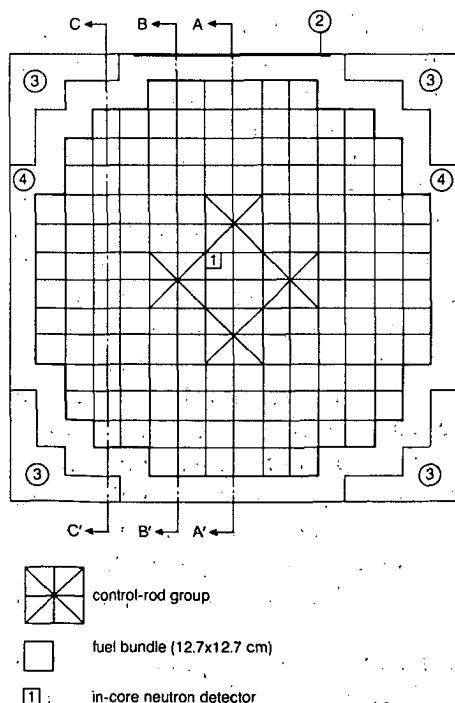


Fig. 10
 Geometry for the EXTERMINATOR-II field-of-view calculations.
 1 = in-core neutron detector; 2 = ex-vessel neutron detector N6; 3 = concrete; 4 = reflector.

necessary to obtain the neutron data for the various compositions - were done with the CASMO computer code (Edenius et al., 1986) for several burn-up states. This code uses ENDF/B-4 (Garber et al., 1975) and ENDF/B-5 (Kinsey, 1979; Magurno & Young, 1985) data as input. The cross-sections for the reflector region were determined by means of a one-dimensional calculation on a 0.15 m thick water layer adjacent to an edge fuel bundle with 35% void. The exact void percentage was of minor importance to the reflector cross-sections as was shown by the calculation of these cross-sections for the situation with 0% void in the neighbouring fuel bundle. The latter cross-sections differed by only 1% from the values mentioned before.

The actual core situation of May 1988 with the four central control rods partly inserted was taken into consideration. The cell calculations for the control groups (each group consists of four fuel bundles surrounding a control-rod blade) were performed by means of the CASMO code for a completely withdrawn and for a completely inserted control rod. The cross-sections thus obtained were interpolated to obtain a critical core. This resulted in a relative density of 46.1% for the control rods.

Figure 11 displays the flux distribution through the core along cross-sections AA', BB' and CC' (see the position of the cross-sections in Fig. 10). The influence of the control rods on the flux profile is obvious.

The field-of-view of an in-core detector - The FOV of a centrally placed neutron detector (denoted 1 in Fig. 10), sensitive to thermal neutrons only, was calculated for 1, 5, 20 and 40 Hz. The cell cross-sections mentioned in the previous subsection were used for calculation of the coefficients (fictitious cross-sections) for the field-of-view equations according to Equations (18)-(22), with $\nu\Sigma_{f^+}^+,_{2i} = \nu\Sigma_{f^+}^+,_{2i-1} = 1 \cdot 10^{-6} \text{ cm}^{-1}$ to obtain a fast convergence. The calculated FOVs are shown in Figure 12, which gives the distribution of the modulus of ϕ^+ through the core for both energy groups, with the maximum of $|\phi^+_{2i}|$ normalised to 1. A flat frequency response of the detector to thermal neutrons is thus assumed. The phase change as a function of distance from the detector is shown as well. It can be seen from this figure that the FOV peaks strongly in the neighbourhood of the detector. The actual peaking is more pronounced (Van Dam, 1976) but is not visible here due to the relatively large mesh width. The figure shows clearly that the response of an in-core detector is composed of a so-called local and a global component, as was mentioned before by several authors (see, among others, Van Dam, 1976; and Behringer et al., 1977). It is precisely this local component of the signal that enables the derivation of the in-core coolant velocity by correlation of the noise of two axially displaced in-core detectors (Chapters 3, 4 and 5 will deal with this topic in more detail).

Note that the FOV decreases with frequency, corresponding to the fact that high-frequency perturbations will be damped. The phase change

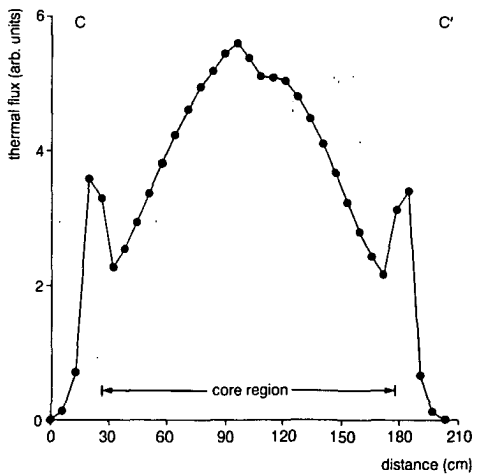
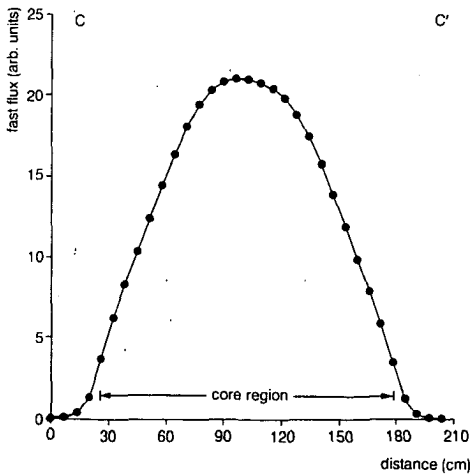
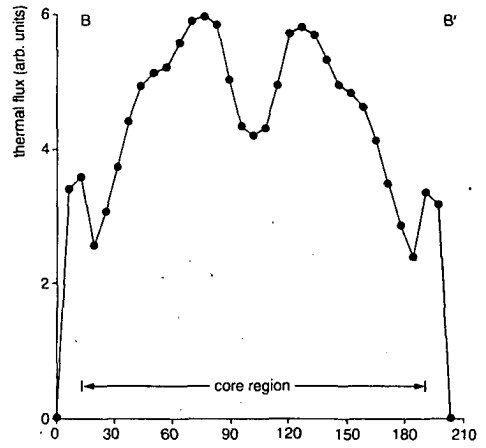
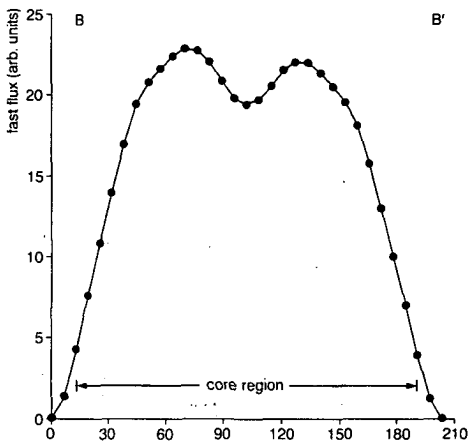
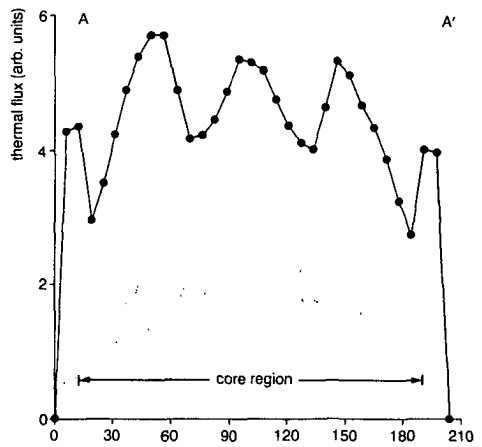
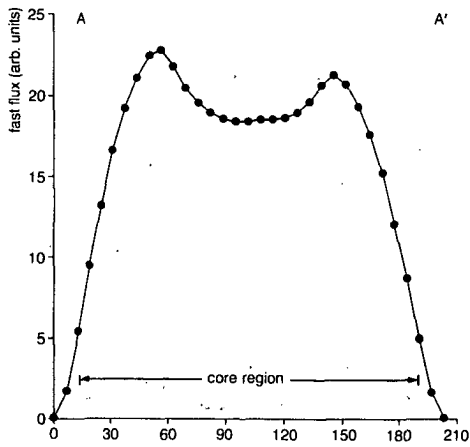


Fig. 11

Fast and thermal neutron-flux distribution through the core along cross-sections A-A', B-B' and C-C' (see Fig. 10).

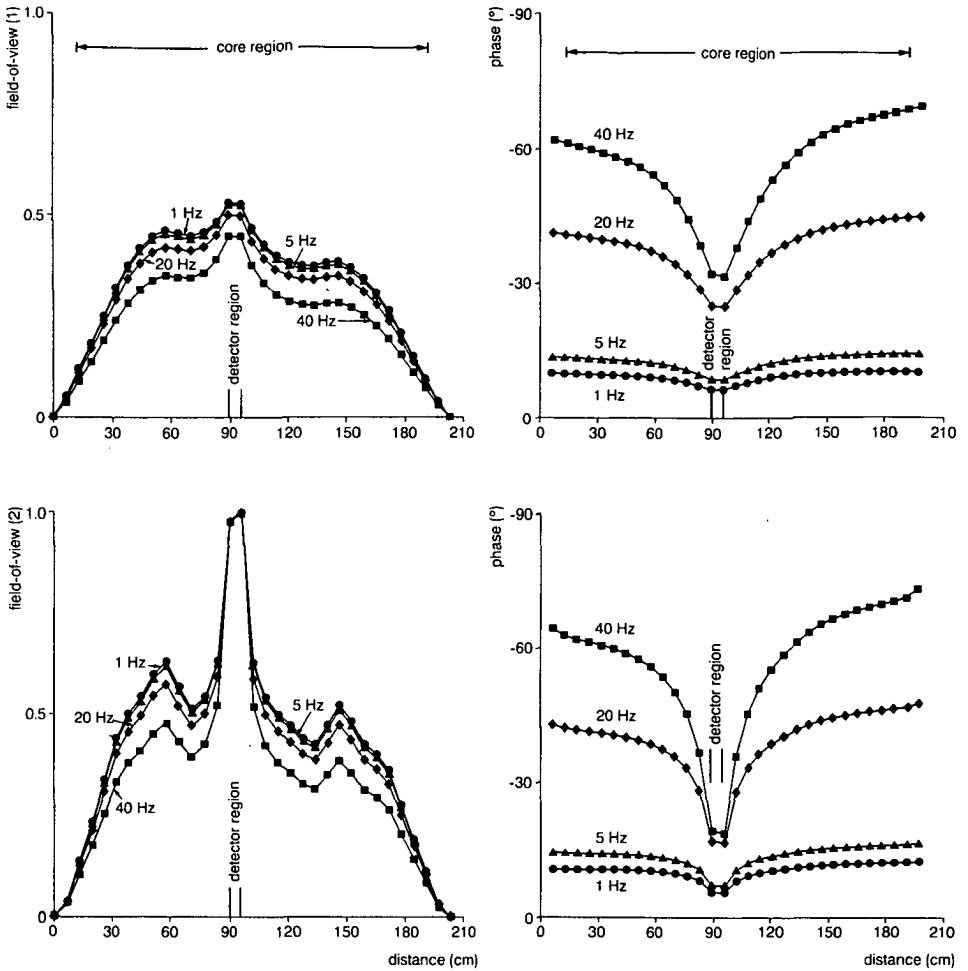


Fig. 12
 Field-of-view of an in-core neutron detector (modulus and phase) for variations in the fast and thermal group.
 circles = 1 Hz; triangles = 5 Hz; diamonds = 20 Hz; squares = 40 Hz.

increases with frequency and with distance from the detector as expected (subsection 'Phase behaviour of the field-of-view'). The phase change in the vicinity of the detector is not equal to zero as a disturbance in this region will spread itself over the core. The FOV for fast neutrons in the neighbourhood of the detector decreases with frequency as down-scattering decreases with frequency (Eq. 22).

The above-mentioned findings are in close agreement with expectations and thus validate the numerical model and method.

The field-of-view of an ex-vessel detector - The FOV of the ex-vessel detectors is of great importance for proper stability monitoring, as was

mentioned in Chapter 1. As only frequencies around the resonance frequency of the core (1 Hz) are of interest, the FOV of an ex-vessel neutron detector - sensitive to thermal neutrons only - was calculated for 1 and 5 Hz. Figure 13 displays the FOV for the fast and the thermal group and the phase behaviour. The phase behaviour for low frequencies is presented in Figure 14. It can be observed that the phase change has a minimum around a frequency of 1 Hz, which is in agreement with the results from the point model (Fig. 8). It can be seen from Figure 13 that parametric fluctuations in the core side facing the detector dominate the detector signal.

It follows from Equation (15) that fluctuations in $\Sigma_{a,1}$, $\Sigma_{a,2}$, $\Sigma_{s,12}$ and $\Sigma_{s,21}$ are weighted by $\phi_1\phi^+_{1}$, $\phi_2\phi^+_{2}$, $\phi_1(\phi^+_{1} - \phi^+_{2})$ and $\phi_2(\phi^+_{2} - \phi^+_{1})$,

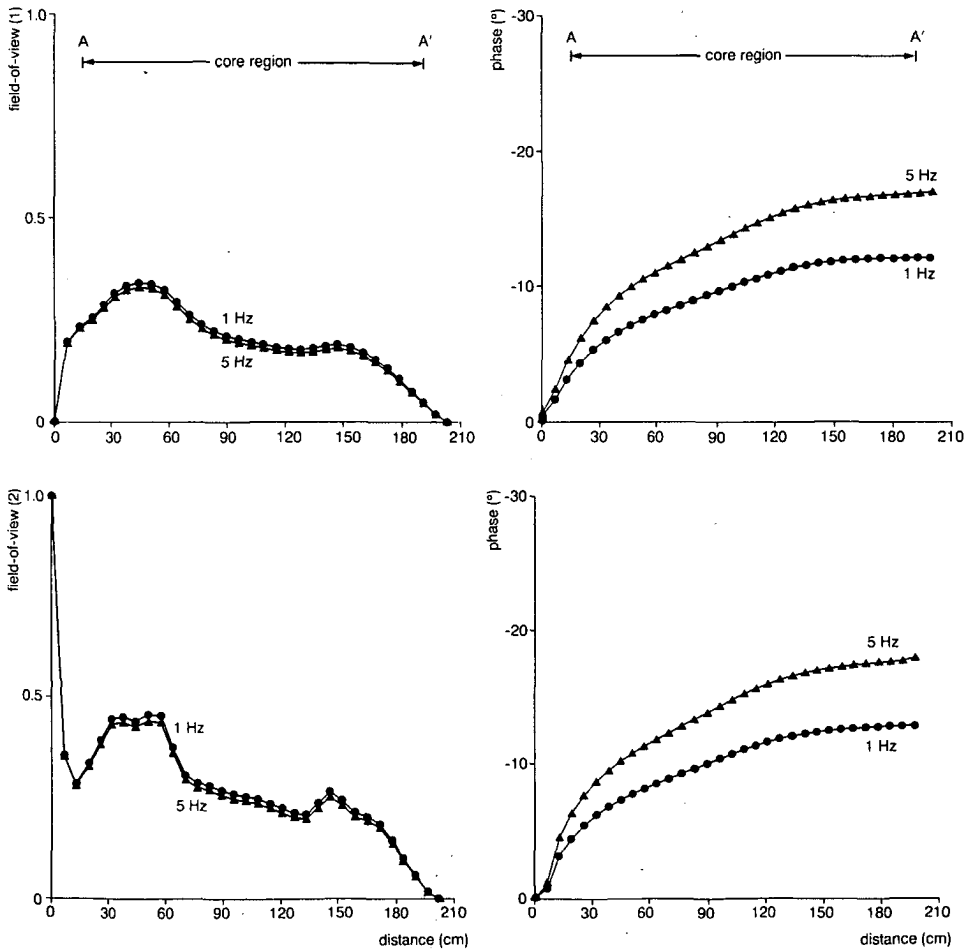


Fig. 13

Field-of-view of an ex-vessel neutron detector (modulus and phase) for variations in the fast and thermal group.

circles = 1 Hz; triangles = 5 Hz.

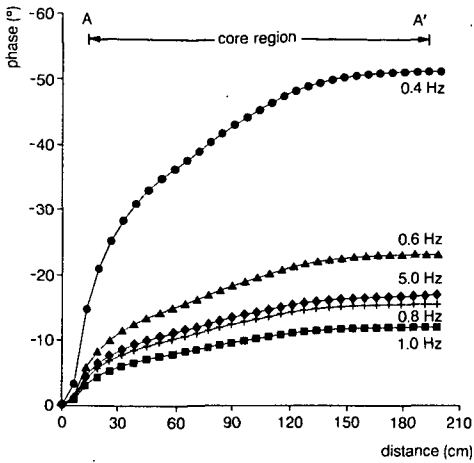


Fig. 14
Phase of the field-of-view of an ex-vessel neutron detector for variations in the thermal group.

respectively. These weighting factors are plotted in Figure 15 for a frequency of 1 Hz, the frequency of highest interest for stability monitoring of the Dodewaard BWR. The influence of the steam-bubble formation on the detector signal via these mechanisms (decrease of absorption and decrease of scattering) can be shown by plotting $\Sigma_{a,1}/\Sigma_{s,12}\Phi_1|\Phi^{+1}|$, $\Sigma_{a,2}/\Sigma_{s,12}\Phi_2|\Phi^{+2}|$, $\Phi_1|(\Phi^{+1} - \Phi^{+2})|$ and $\Sigma_{s,21}/\Sigma_{s,12}\Phi_2|(\Phi^{+2} - \Phi^{+1})|$, where the cross-sections were calculated for water in the centre of a fuel bundle: $\Sigma_{a,1} = 2.99 \cdot 10^{-4} \text{ cm}^{-1}$, $\Sigma_{a,2} = 8.9 \cdot 10^{-3} \text{ cm}^{-1}$, $\Sigma_{s,12} = 3.15 \cdot 10^{-2} \text{ cm}^{-1}$ and $\Sigma_{s,21} = 1.92 \cdot 10^{-3} \text{ cm}^{-1}$ (Fig. 16).

It is clear that the decrease in moderation [$\Sigma_{s,12}\Phi_1(\Phi^{+1} - \Phi^{+2})$] forms the dominant factor. Table 2 and Figure 17 give the distribution of the modulus of this factor, with its maximum normalised to 100%, over the core. It is obvious from these that changes in the void fraction generated in fuel bundles with high power contribute most to the detector signal (this is when the noise-source strength is equal to the strenght in the

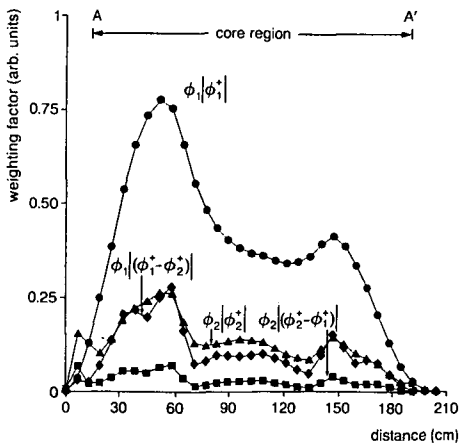


Fig. 15
Weighting factors for an ex-vessel neutron detector for parametric 1 Hz fluctuations.
circles = $\Phi_1|\Phi^{+1}|$;
triangles = $\Phi_2|\Phi^{+2}|$;
diamonds = $\Phi_1|(\Phi^{+1} - \Phi^{+2})|$;
squares = $\Phi_2|(\Phi^{+2} - \Phi^{+1})|$.

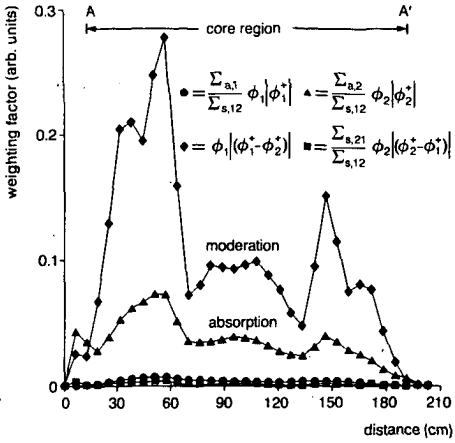


Fig. 16
Relative contribution of void-fraction variations of 1 Hz to the ex-vessel neutron signal.

Fig. 17
Distribution of the relative contribution of 1-Hz variations of the moderation cross-section to the signal of ex-vessel detector N6.

1 = 10-20%, 2 = 20-30%, ..., 9 = 90-100%.

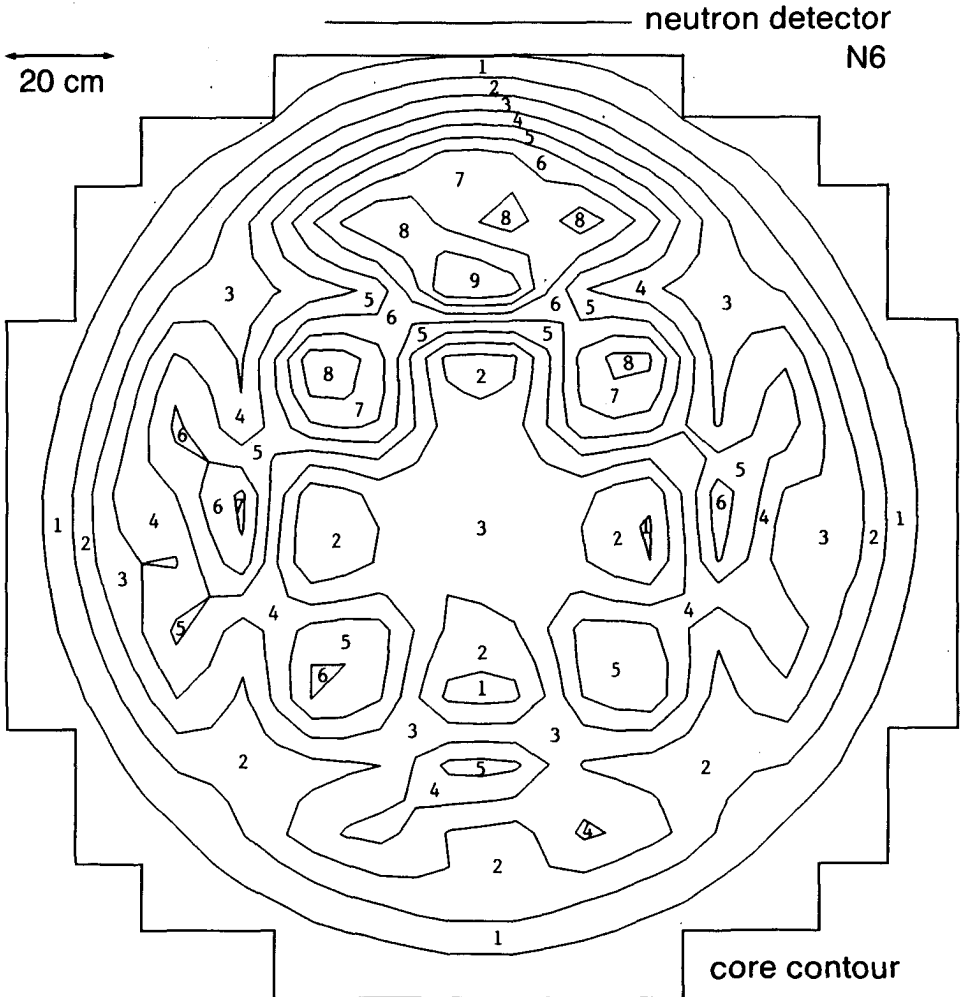


Table 2

Distribution of the relative contribution of 1-Hz variations of the moderation cross-section to the signal of ex-vessel detector N6 over the left half of the core. Values larger than 50% are printed in bold type; values larger than 75% are underlined.

										<i>detector position</i>													
										1	3	5	6	7	8	8							
										2	9	13	17	21	23	24							
										0	1	1	3	10	19	26	32	39	45	46			
										1	5	9	14	23	33	43	53	63	72	73			
										0	0	4	10	16	25	37	51	63	74	<u>78</u>	<u>78</u>	75	
										0	3	8	15	24	36	51	68	<u>81</u>	<u>90</u>	<u>86</u>	<u>77</u>	70	
										1	6	13	22	29	36	47	57	66	73	<u>83</u>	<u>92</u>	<u>89</u>	
										2	10	20	31	34	34	39	44	48	53	75	<u>98</u>	<u>100</u>	
										6	15	27	41	41	36	49	63	65	63	60	58	57	
0	3	10	20	36	52	47	39	60	<u>86</u>	<u>85</u>	75	48	28	26									
0	5	13	25	42	59	51	40	59	<u>81</u>	<u>82</u>	74	50	31	29									
1	6	16	30	47	62	54	42	54	68	71	69	51	36	34									
1	8	19	35	48	57	60	57	49	42	45	49	41	34	34									
1	9	21	39	47	50	64	72	45	23	27	33	33	32	33									
1	9	21	38	44	44	60	71	43	20	24	30	31	32	34									
1	8	20	36	40	39	55	66	41	21	25	31	31	32	35									
1	7	17	31	40	46	50	49	42	36	38	41	36	30	31									
1	6	14	26	40	52	45	34	44	54	56	54	40	29	27									
0	4	11	21	34	47	40	31	44	60	60	54	36	22	21									
0	3	8	16	27	40	35	28	43	60	59	51	32	18	17									
0	0	4	11	20	30	29	25	33	42	42	39	37	34	34									
										1	7	14	21	22	22	24	26	28	30	41	53	54	
										0	4	9	14	18	22	27	32	36	38	41	42	41	
										0	2	5	9	14	20	28	36	41	43	37	29	27	
										0	0	2	5	9	13	18	24	29	33	32	30	29	
										0	2	4	7	10	14	18	21	25	27	27			
										0	0	1	1	4	7	9	11	13	15	15			
										0	2	3	4	5	6	6							
										0	0	0	0	1	1	1							

the strength in the other bundles). The least stable channels are therefore specially monitored by the ex-vessel detector.

Another interesting issue is that the ex-vessel detector 'looks' behind the control rods although fluctuations in the control-rod region do not contribute to the detector signal (as the neutron flux is low in this region): fluctuations in remote regions are propagated around the control rods to the detector.

Evaluations

The possibility of calculating the frequency-dependent field-of-view of a neutron detector by a conventional neutron-diffusion code was demonstrated. The calculated field-of-view of an in-core neutron detector in the Dodewaard reactor is in close agreement with earlier findings and expectations.

The field-of-view of an ex-vessel detector - of great importance for proper stability monitoring of the Dodewaard reactor - was calculated for various frequencies and the result leads to the conclusions that

- (1) three detectors positioned around the core cover the entire core,
- (2) the field-of-view of a single detector is not so large that the monitoring of local effects is impeded,
- (3) fluctuations in the least stable fuel bundles dominate the variations of the detector signal.

Chapter 3

Measuring in-core coolant velocity by noise correlation

Noise analysis has become a powerful and widely used tool for obtaining information on the coolant flow through the fuel elements of a BWR. It is well known that correlating the noise signal of two axially separated in-core detectors enables the derivation of the coolant velocity because the local component of the detector noise signal, which is dominant at frequencies higher than a few hertz (see Chapter 1), is formed by the influence of passing signal disturbers, such as steam bubbles.

To explain this technique, consider the in-core detector pair as shown in Figure 18. Rising steam bubbles will first affect the signal of the lower detector and thereafter that of the upper (upstream) detector. The signals of the two detectors are therefore correlated and can be used to estimate the time of transit of the bubbles from the lower to the upper detector. The velocity of the signal disturbers can easily be derived as the distance

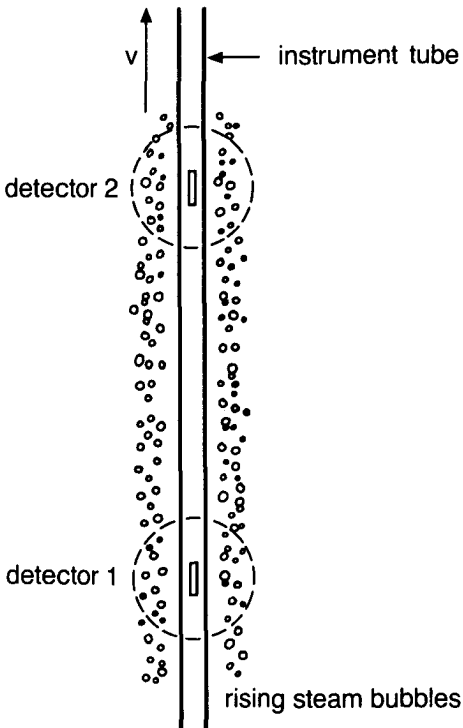


Fig. 18
An in-core detector pair.

between the two detectors is known (Wach, 1973). The accuracy of this derivation depends on the correlation of the signals due to their disturbance by bubbles: global variations of the flux hamper the velocity determination, as does a loss of correlation between the detectors (collapsing bubbles, newly formed bubbles, etc.). The interpretation of the measured velocity is not as straightforward as mentioned above; the problems associated with it are addressed in Chapter 4.

The relevant theory of noise correlation is summarised in the present chapter. The detector type which was designed and manufactured for the velocity measurements is described and the measured axial velocity profile over the Dodewaard core is presented.

Velocity determination by noise correlation

Neutron detectors are preferred for velocity determination as they have a smaller field-of-view than detectors sensitive to gammas and are therefore relatively less influenced by global variations of the flux (Van Dam & Kleiss, 1985). This small field-of-view has also a disadvantage: only velocities in the very corners of neighbouring fuel bundles can be measured (Kleiss et al., 1985).

The fluctuations of the signals of the two detectors in Figure 18 $\delta s_1(t)$ and $\delta s_2(t)$ can be split into a coherent part $c(t)$ - assumed to be purely local - and a non-coherent part $\varepsilon_1(t)$, $\varepsilon_2(t)$. Then

$$\delta s_1(t) = c(t) + \varepsilon_1(t) \quad (\text{Eq. 45a})$$

$$\delta s_2(t) = c(t - \tau) + \varepsilon_2(t) \quad (\text{Eq. 45b})$$

where τ denotes the transit time of the signal disturbers to rise from the lower to the upper detector. In this case, the cross-correlation function (abbreviated as CCF) of the two signals is equal to the auto-correlation function (abbreviated as ACF) of the coherent part ACF_c at $t - \tau$ as follows from Equation (46):

$$\begin{aligned} CCF(t) &= \langle \delta s_1(t') \cdot \delta s_2(t' + t) \rangle = \langle c(t') \cdot c(t' + t - \tau) \rangle = \\ &= ACF_c(t - \tau) \end{aligned} \quad (\text{Eq. 46})$$

where $\langle x \rangle$ denotes the time average of x .

As the $ACF_c(t)$ has its maximum at $t = 0$, the $CCF(t)$ has its maximum (equal to the variance of the coherent part) at $t = \tau$. The cross power spectral density (abbreviated as CPSD) of signals 1 and 2 is found after Fourier transformation of the CCF:

$$\begin{aligned} CPSD(f) &= \int_{-\infty}^{\infty} CCF(t) \exp(-j2\pi ft) dt = \\ &= \int_{-\infty}^{\infty} ACF_c(t - \tau) \exp(-j2\pi ft) dt = APSD_c \exp(-j2\pi f\tau) \end{aligned} \quad (\text{Eq. 47})$$

where $APSD_c$ denotes the auto-power spectral density of the coherent part, which is a real function. The phase of the CPSD is therefore a linear function of frequency, with its slope equal to $-2\pi\tau$.

Two methods of velocity determination that both use the noise signals of in-core detectors can be distinguished:

- (1) in the time domain: using the CCF of the noise signals. This function will peak at a time lag equal to the time required for the disturbers to go from the lower to the upper detector (Eq. 46); the position of the maximum can be calculated by using e.g. a parabolic fit of the maximum of the discrete CCF and its two adjacent values;
- (2) in the frequency domain: using the phase of the CPSD of the noise signals. The phase can be fitted to a straight line with its slope equal to $-2\pi\tau$ (Eq. 47). As the phase of the CPSD can only be determined from $-\pi$ to π , jumps of 2π have to be eliminated by an extrapolation procedure.

Design and manufacturing of a twin self-powered detector

The design of the detector used for the measurements is an improved version of the twin self-powered detector (TSPD) designed by Kleiss & Van Dam (1981a). The improvement does not lie in the principle of operation but results from better hardware design and fabrication techniques. Two detectors sensitive to neutrons (TSPND) were used for the velocity measurements presented in this study.

Each detector consists of two sensitive elements, the emitters, mounted in-line on three signal cables (Fig. 19). These signal cables are clad by a drive cable. Two signal wires are fixed to the emitters whereas the third signal wire serves as a compensation wire that makes it possible to subtract the parasitic part of the signal generated by neutrons and gammas in the signal cables. The signal wires are insulated from their cladding by

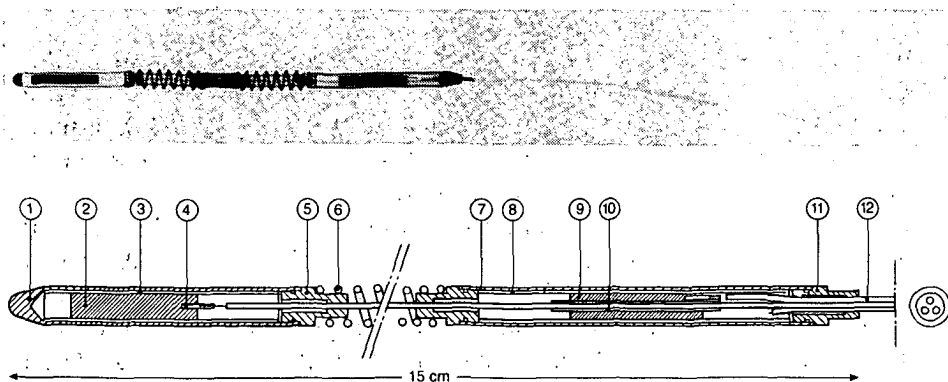


Fig. 19
Design of a twin self-powered detector.

MgO. The signal wire with jacket of the upper emitter is led through the hollow lower emitter that is insulated by a small Al₂O₃ tube.

The principle of operation of the TSPND is as follows. Incoming neutrons are absorbed by the emitter. The released gamma radiation frees electrons that travel through the insulator between emitter and detector sheath and are captured in the detector sheath. Thus a prompt electrical current is formed without any additional power supply (self-powered). The emitter material of the TSPND is a cadmium/magnesium alloy (60/40 wt%). Cadmium is a strong neutron absorber, unfortunately with a low melting point (593 K). The addition of magnesium raises the melting point to approximately 775 K (Kleiss & Van Dam, 1981a). The detector sheath is made of stainless steel, so that a relative small number of neutrons is captured in the detector sheath.

A twin detector sensitive to gammas (TSPGD) was constructed as well (Table 3). The emitters and the sheath of this detector are made of zirconium. The principle of operation is the same as that for the TSPND, except that the electrons are freed directly by the incoming gammas. The signal in this detector merely consists of the difference between the number of electrons going from the emitter to the sheath and those travelling the other way around.

Table 3
Characteristics of the twin self-powered detectors (Fig. 19).

no. description	material		dimensions (mm)
	TSPND	TSPGD	
1 sheath	stainless steel	zirconium	5.0x4.0x35
2 emitter	cadmium-magnesium	zirconium	3.0x20
3 insulator	aluminium oxide (Al ₂ O ₃)		4.0x3.0x30
4 capillary (2)	stainless steel		0.8x0.6x8
5 cap (2)	stainless steel		-
6 spring	stainless steel		5.5x2.5x50
7 sheath	stainless steel	zirconium	5.0x4.0x40
8 insulator	aluminium oxide (Al ₂ O ₃)		4.0x3.0x40
9 emitter	cadmium-magnesium	zirconium	3.0x1.8x20
10 insulator	aluminium oxide (Al ₂ O ₃)		1.7x1.1x25
11 cap	stainless steel		-
12 signal wires (3)			1.0x25000

The fabrication of the TSPGD needs further comment as zirconium is a very difficult metal to weld or to solder to stainless steel. The zirconium was therefore first welded to an aluminium partition-ring by a friction-welding technique. In this technique, one of the two objects is rotated (approx. 2000 rotations per minute) while the other object is pressed with a small preset tension towards it, so that the two adjoining surfaces are heated by friction. Rotation is stopped after approximately fifteen seconds (this value was determined experimentally) and the two objects are pressed into each other over a fixed distance (a few millimetres) and the connection is made.

Once the aluminium had been welded to the zirconium, the stainless steel could be welded to the aluminium by the same method. Finally, these stainless-steel caps were soldered to the jackets of the signal wires with gold/nickel solder. The experimental results obtained by means of this detector type are not yet available but it is hoped to present them in the near future.

The effective distance between the two emitters is 96.6 mm and 94.0 mm for the two TSPNDs and 99.5 mm for the TSPGD.

Velocity profile

The axial velocity profile of the coolant was measured with the above-mentioned neutron detectors. The detectors fit into the tubing system used in the Dodewaard reactor for the guidance of the traversing in-core probe (TIP) detector, so that the velocity profile at four radial positions could be investigated. The NAPSD of one of the emitters of the TSPND is shown in Figure 20 for various axial positions in tube 4D. The low-frequency part of the spectrum is formed by (global) reactor-power fluctuations whereas variations with frequencies higher than a few hertz are attributed to the presence of steam bubbles in the vicinity of the detector.

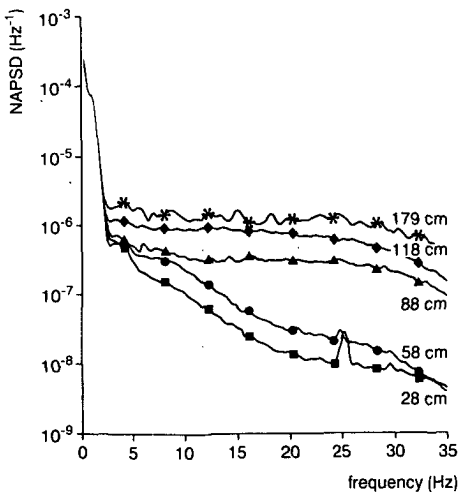


Fig. 20
Normalised auto-power spectral density of the signal of an in-core neutron detector at five axial positions in detector tube 4D.

The latter variations obviously increase with axial position due to the increase in void fraction. A resonance peak at approx. 25 Hz is seen at the two lower detector positions and is probably a sub-harmonic of the frequency of the electrical mains (50 Hz). This peak is masked at higher axial positions by the boiling noise. Figure 21 presents the coherence between the two emitter signals and the phase of the CPSD at four axial positions in detector tube 4D. A zero phase change is observable at low frequencies; it corresponds with the global character of this part of the signal. Linear phase behaviour can be seen at higher frequencies, in agreement with Equation (47).

The slope of the phase decreases with axial position due to the increase of coolant velocity. The local coolant velocity was determined from this phase slope using the procedure mentioned in an earlier subsection of the present chapter (*Velocity determination by noise correlation*). The axial velocity profile was measured at four radial detector positions: 4D, 4B, 2E and 6B (see Fig. 2). The result is shown in Figure 22. It is obvious from this figure that the axial velocity profile does not vary much between the various radial positions; only the measured outlet velocity differs considerably and, in three cases, is lower than the velocity at the next axial position. In fact, both the steam and the water velocity are expected to increase with axial height (Kleiss et al., 1985).

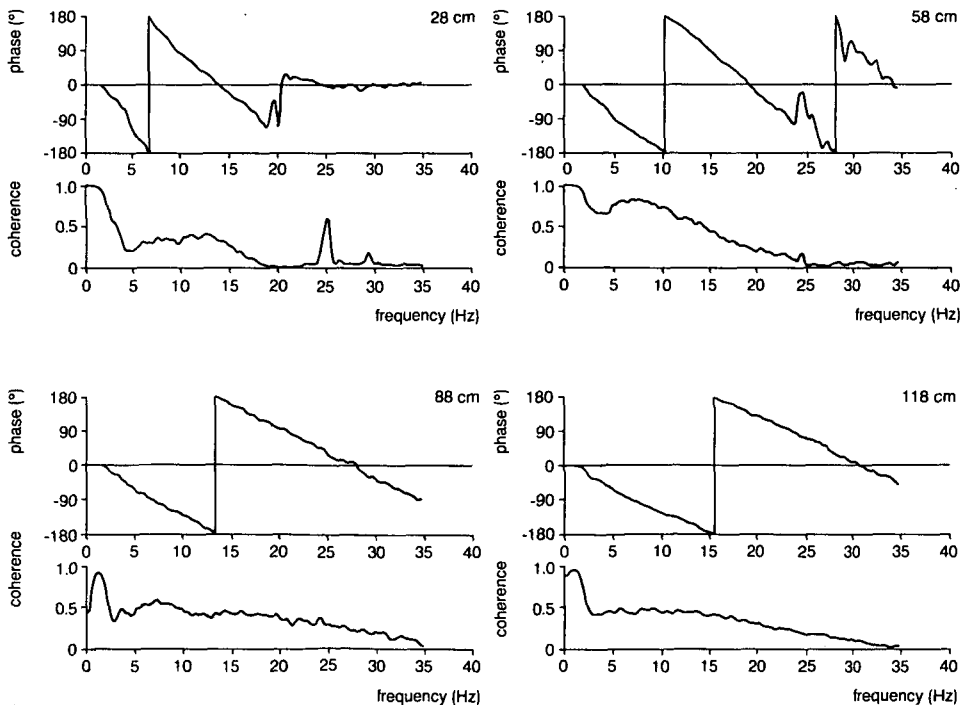


Fig. 21
Phase and coherence of the two emitter signals of a TSPND at four axial positions in detector tube 4D.

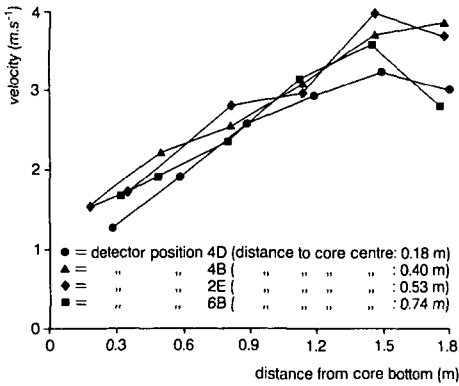


Fig. 22
Measured axial profile of the coolant velocity.

At least three sources of a discrepancy between the actual velocity and the measured velocity at the outlet of a fuel bundle can be distinguished:

- (1) The nature of the signal perturbations. In the case of a high outlet void fraction (such as at the top of a fuel bundle), it is likely that the signal perturbations are caused by passing water droplets instead of steam bubbles. These droplets rise slower than the steam since the slip factor is larger than unity.
- (2) The drift of the void towards regions with a higher velocity, i.e. the centre of the fuel bundle (Kleiss et al., 1985). As the detector has a small field-of-view, the measured velocity is formed by a combination of the water and the steam velocity in the outer subchannels of a fuel bundle. A decrease in the number of fast-rising steam bubbles results in a lower velocity measured.
- (3) turbulences due to the channel outlet.

The first two sources will result in a measured velocity lower than the average steam velocity; the influence of the last source on the velocity is not known.

The interpretation of the measured velocity is treated in Chapter 4.

Conclusions

The noise signal of a neutron detector in the Dodewaard core corresponds perfectly well with expectations and can be explained on the basis of the local/global concept (see Chapter 1).

The coolant velocity profile over the Dodewaard core was measured by means of a so-called twin self-powered neutron detector, which was designed and manufactured for the purpose.

Chapter 4

Interpretation of velocities determined by noise analysis for various void fractions and flow regimes in two-phase flow¹

T.H.J.J. van der Hagen² & J. Van der Voet²

Abstract

Experiments are performed in an air/water loop in order to gain insight into the physical interpretation of the velocities measured by noise correlation in a BWR. Thermal neutrons and detectors are modelled by visible light produced in the water and photo-transistors. Bubbly, slug and froth flow are examined. The flow type at issue in the loop can be determined from the probability density function of the photo-transistor signals.

For each flow pattern, the measured velocity is much higher than the volume-averaged water and air velocity and the volumetric flux, which are usually taken as an interpretation. However, the velocity measured for bubbly flow corresponds with the calculated velocity of bubbles without wall interaction. In the case of slug flow, application of an independent experimental method indicates that it is the average slug velocity that is measured by noise correlation. No theoretical basis is found for froth flow.

¹ This chapter is a slightly adapted version of a contribution published in *Progress in Nuclear Energy* 21: 565-573 (1988). It is included here as it clarifies the physical interpretation of the velocities measured by noise correlation in a BWR, a technique introduced in Chapter 3.

² Interfaculty Reactor Institute, Delft University of Technology, Mekelweg 15, 2629 JB DELFT, The Netherlands.

Introduction

Cross-correlation of the noise of the signals of axially separated in-core detectors is a widely used technique for obtaining information on the velocity of the two-phase mixture through the core of a BWR. The physical interpretation of the measured velocity, however, has been an important topic of discussion for some time: it is not clear whether steam velocity, water velocity or something in between (for instance the volumetric flux: Lübbesmeyer, 1983) is measured. The situation is much complicated by the existence of various flow regimes (regimes ranging from steam bubbles in water to droplets in steam are to be expected because the void fraction varies from 0% at the bottom to 70% at the top of the core). Nevertheless it is of a great importance to be able to measure the coolant velocity with satisfying accuracy for several applications:

- (1) the coolant flow in a BWR cooled by natural circulation is not known and can only be derived from thermal-hydraulic calculations or design values,
- (2) the distribution of the coolant over the core cannot be measured in any other way without disturbing the coolant flow,
- (3) a possibility would be offered to verify computer codes and input data for these codes.

Another issue is the possibility of determining the flow regime under consideration from the noise signals or from their characteristic functions (probability density function, correlation function, power spectrum, coherence) (Albrecht et al., 1982).

A clear review on both topics is given by Lübbesmeyer (1984).

The present study deals with experiments on an air/water loop that models a coolant channel of a BWR. Unlike earlier simulations, the set-up also models the moderation effect of neutrons. In the future, the set-up can be extended to study topics such as the influence of subchannel velocities, void drift, etc.

Description of the air/water loop

A coolant channel of a BWR was modelled by means of a glass tube two metres in height through which water is pumped upwards. The inner diameter of the tube is 36.6 mm. Air can be added at the bottom of the tube to obtain a void fraction as high as 70%. The air and water flow can be changed separately, thus making it possible to produce bubbly, slug or froth flow. The latter flow pattern is also called churn, wave entrainment, dispersed slug or semiannular. A detailed description of these flow types can be found in textbooks such as that by Govier & Aziz (1972).

UV-light sources (wave length ≈ 370 nm; 1 m in height) are placed at two opposite sides of the tube; their radiation excites a fluorescent powder that is dissolved in the water and that emits visible light (wave length \approx

560 nm) when shone upon: Photo-transistors fixed in rings around the tube register the visible light emitted and serve as a model for neutron or gamma detectors, depending on their field-of-view (Van Dam, 1976; Van Dam & Kleiss, 1985). They are not sensitive to UV light, analogous to neutron detectors that do not detect fast neutrons. The signal carrier - here visible light - is thus produced in the water, as thermal neutrons are in the coolant of a reactor. The UV radiation models the fast neutrons in a reactor. Figure 23 gives an impression of the set-up.

The relaxation lengths (λ) of the two types of light were adjusted by varying the concentration of the fluorescent powder and by adding a powder that absorbs the visible radiation. Values of 55 mm for the UV light and 25-30 mm for the visible light were chosen for the measurements given below. The latter value corresponds with the relaxation length, ℓ , that characterises the local field-of-view of a neutron detector in a BWR being, according to Van Dam (1976),

$$\ell^2 = \frac{1}{\frac{1}{L^2} + \frac{1}{\tau}} \quad (\text{Eq. 48})$$

where L is the thermal diffusion length and τ the Fermi age. The relaxation-lengths were checked by measuring the attenuation of the two light types with a photo-multiplier (selecting the wavelength with a monochromator). The results correspond well with the desired values:

$$\lambda_{UV} = 55 \pm 2 \text{ mm} \quad (\text{Eq. 49a})$$

$$\lambda_{\text{visible}} = 27 \pm 1 \text{ mm} \quad (\text{Eq. 49b})$$

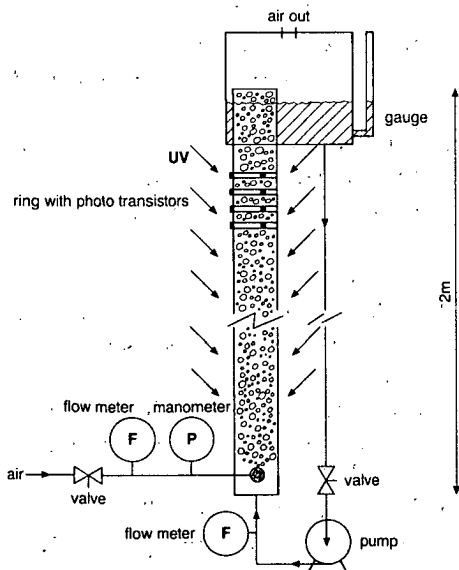


Fig. 23
The experimental set-up.

The physical properties of the water are not changed significantly by adding the powders to the water: the specific density was found to be $1000 \text{ kg}\cdot\text{m}^{-3}$ and the surface tension $70(\pm 1)\cdot 10^{-3} \text{ N}\cdot\text{m}^{-1}$ (the surface tension of water at 296 K is $72\cdot 10^{-3} \text{ N}\cdot\text{m}^{-1}$).

Characteristic functions

In order to try to identify the flow pattern at issue, the following characteristic functions from the noise signals might be considered:

- (1) the probability density function (PDF) (Albrecht et al., 1982),
- (2) the cross-correlation function (CCF),
- (3) the auto- and cross power spectral density (APSD, CPSD),
- (4) the coherence spectrum (γ^2).

For the definition and a mathematical outline of these functions, one is referred to Jenkins & Watts (1968). A similar attempt by Lübbesmeyer (1984) - covering a great number of flow regimes - met with limited success.

Figure 24 displays the characteristic functions for the three flow regimes observed: bubbly, slug and froth.

The PDFs show that bubbly flow is characterised by one peak (unimodal flow) that is due to small changes of the signal around the mean value caused by passing bubbles. As air bubbles do not contain the fluorescent powder, they do not produce visible light and the signal of the photo-transistor will decrease. In the case of slug flow, the PDF consists of one distinct peak at a negative signal value caused by air slugs that nearly fill the entire cross-section of the tube and of a broad maximum at a positive value formed by small bubbles in water. The PDF for froth flow exhibits two distinct peaks; one peak is due to the passing of a big air bubble and the other to the passing of a liquid slug (bimodal flow). Use of this unimodal/bimodal character of the PDF as an identification method in a BWR is impeded in two ways:

- (1) The low-frequency behaviour is disturbed by the global neutron noise. This problem can be overcome by subtracting the signal of an ex-core neutron detector that only measures the global noise component (Albrecht et al., 1982).
- (2) The signal of a neutron detector is influenced by the two-phase flow through the rod bundles surrounding the detector. The situation is even more complicated in the case of a gamma detector as its field-of-view is larger (Van Dam & Kleiss, 1985).

The APSD in the case of bubbly flow is flat and the coherence low. Due to this low coherence, the linearity of the phase spectrum - indicating a transit time (see a following subsection, headed '*Velocities obtained by noise correlation*') - is lost for frequencies higher than 10 Hz. The spectra for other flows decrease strongly with increasing frequency and the coherence is much higher. The difference in phase angle for the three flow

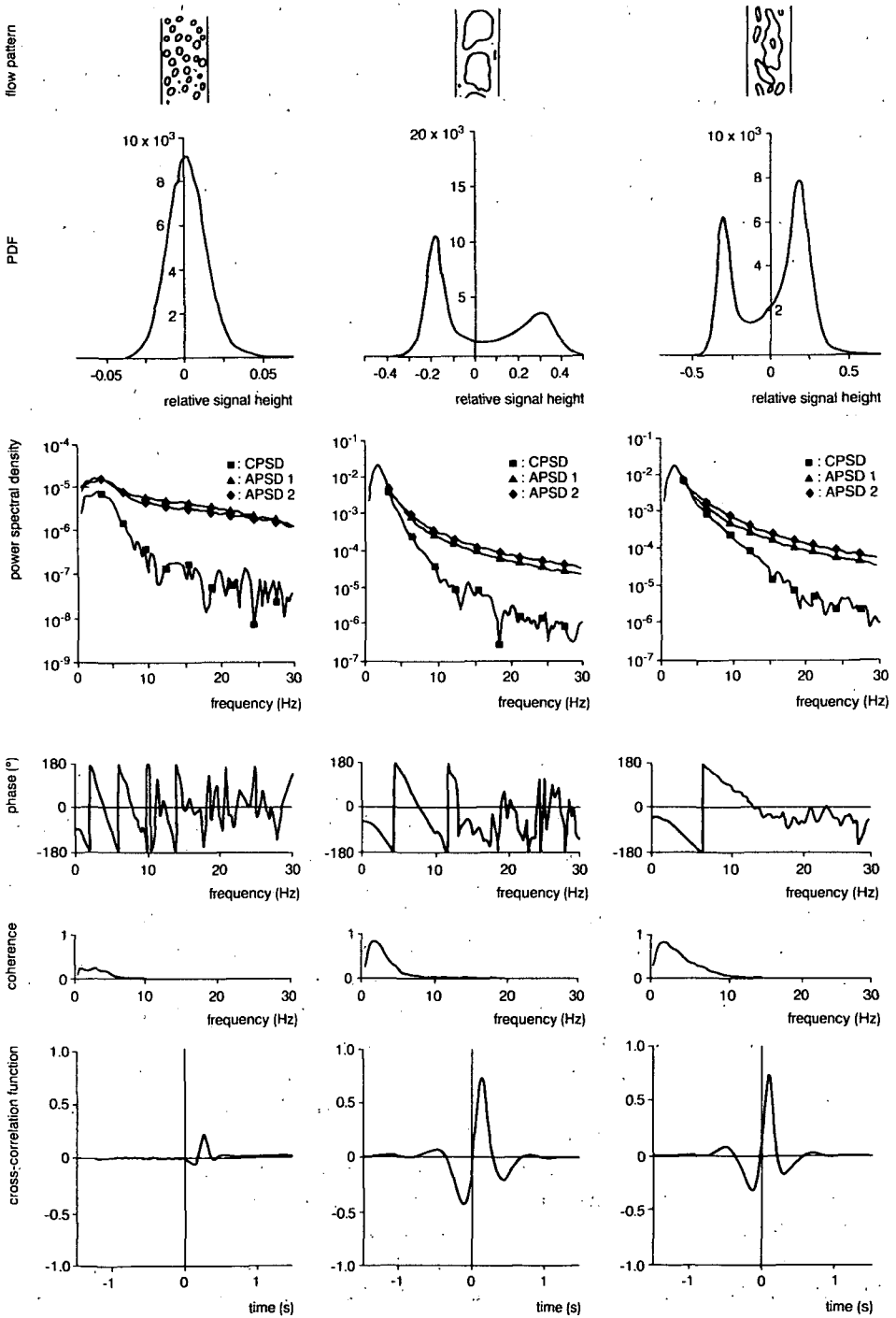


Fig. 24
Flow patterns and characteristic functions for bubbly, slug and froth flow.

types denotes different velocities. Bubbly flow yields the lowest velocity measured and froth flow the highest.

The CCF exhibits for all flow patterns a distinct maximum that can be used to determine the velocity. In the case of bubbly flow, the CCF maximum is low due to the low coherence.

In conclusion, it can be stated that the flow regime in this test loop can be distinguished by observing the PDF. In order to allow for meaningful application in a BWR, however, more research is required, using more complex set-ups. The model will therefore be extended in the future.

Theoretical velocities

Insight into the measured velocities can only be obtained if the air and the water velocity are known. The average velocities, V_a and V_w , can be derived from the void fraction α and the volumetric-flow rates of the air, Q_a , and the water, Q_w , according to

$$V_a = \frac{Q_a}{\alpha A} \quad (\text{Eq. 50})$$

$$V_w = \frac{Q_w}{(1-\alpha)A} \quad (\text{Eq. 51})$$

where A is the cross-section of the tube.

The void fraction was determined by measuring the level of the water in the reservoir by means of a gauge (Fig. 23) and comparing this with the level without air. As the total volume of the tube above the air inlet is known, the average void fraction can easily be derived. In the case of bubbly flow, the void fraction thus obtained was checked with a gamma-absorption technique. A 300 mCi ^{241}Am gamma source and a NaI scintillation detector were placed at opposite sides of the tube. The void fraction can be calculated from the measured gamma intensity if the intensities in the case of a tube filled with water and a tube filled with air are known. This measurement was performed at three axial positions. The results are reported in Table 4; the void fraction obtained from the level measurement for this case is $24 \pm 5\%$.

It can be concluded from Table 4 that the void fraction does not vary significantly along the axis of the tube and that it corresponds with the fraction obtained from the measurement based on the water level. This validates the latter method. Note: it is quite complicated to use the gamma-absorption technique to measure the void fraction for the other flow types since the void in these cases is not uniformly distributed over the cross-section of the tube. The level method was therefore used throughout.

Table 4

Void fractions obtained by means of a gamma-absorption technique
(level method: $\alpha = 24 \pm 5\%$).

distance from the air inlet (m)	α (%)	σ_α
0.36	23.72	0.05
0.635	22.51	0.10
0.91	23.04	0.53

The flow rates were measured by means of Rota-flowmeters. A pressure correction must be carried out to calculate the precise air-flow rate. A manometer was therefore installed right behind the flowmeter. The measured volumetric-flow rate must be corrected using

$$Q_a = Q_{a,m} \cdot \left(\frac{p_{cal}}{p_m}\right)^{1/2} \quad (\text{Eq. 52})$$

where Q_a is the corrected volumetric-flow rate through the flowmeter, $Q_{a,m}$ is the volumetric-flow rate indicated by the flowmeter, p_{cal} is the pressure at which the flowmeter was calibrated ($= 1.18 \cdot 10^5 \text{ N}\cdot\text{m}^{-2}$), and p_m is the pressure of the air in the flowmeter (measured by means of the manometer).

Q_a does not represent the volumetric-flow rate of the air through the tube because the pressure drops significantly in the air inlet. A second correction must be performed for the pressure of the air at the position of the photo-transistors. The pressure gradient of the air/water mixture was calculated for the purpose, using an equation of Govier & Aziz (1972: 348):

$$\frac{\Delta p}{\Delta z} = \frac{\alpha V_a \rho_a + (1-\alpha)V_w \rho_w}{V_M} g + \frac{2\rho_w(1-\alpha)^2 V_w^2}{D} f_{tp} \quad (\text{Eq. 53})$$

where $\Delta p/\Delta z$ is the pressure drop per unit length, ρ_a is the air-mass density, ρ_w is the water-mass density, g is acceleration due to gravity, D = tube diameter, f_{tp} is a two-phase friction factor, and V_M is the volumetric flux (average velocity of the mixture) with the value

$$V_M = \alpha V_a + (1-\alpha)V_w = (Q_a + Q_w)/A \quad (\text{Eq. 54})$$

This formula holds for all flow types except annular mist. The experimental data for the two-phase friction factor were obtained from Govier & Aziz (1972). The pressure at the position of the photo-transistors was

calculated using $p_{\text{out}} = 1 \text{ atm} (= 1.01 \cdot 10^5 \text{ N} \cdot \text{m}^{-2})$ and outlet velocities for V_a and V_w . The volumetric-flow rate of the air at this position, $Q_{a,p}$, is obtained with

$$Q_{a,p} = Q_a \cdot \frac{p_m}{p_{\text{out}}} \cdot \frac{p_{\text{out}}}{p_{\text{out}} + \frac{\Delta p}{\Delta z} \cdot z_p} = Q_{a,m} \cdot \frac{\sqrt{p_{\text{cat}} p_m}}{p_{\text{out}} + \frac{\Delta p}{\Delta z} \cdot z_p} \quad (\text{Eq. 55})$$

where z_p denotes the distance from the photo-transistors to the outlet of the tube.

The average air velocity, V_a , and thus V_M at the position of the photo-transistors can be calculated with Equations (50)-(55).

The velocity profile of the bubbles over the tube cross-section is not flat; bubbles near the tube wall will have a considerably lower velocity than those in the centre, due to wall interaction. Wall interaction can be neglected for bubbles in the centre of the tube (Wallis, 1969: 251). Their velocity can be calculated using the drift flux model (neglecting wall interaction):

$$V_b = C_0 V_M + V_{bs} \quad (\text{Eq. 56})$$

where V_b is the bubble velocity, C_0 is the Zuber-Findlay distribution parameter ($= \langle \alpha V_M \rangle / (\langle \alpha \rangle \langle V_M \rangle)$, where $\langle \rangle$ denotes averages over the tube cross-section) and V_{bs} is the bubble velocity in stagnant water.

For bubbly flow holds, with a most probable value of 1.2 (Wallis, 1969: 256) that $1.0 < C_0 < 1.5$. The bubble velocity must be corrected for the void fraction:

$$V_{bs} = f_a V_{bso} \quad (\text{Eq. 57})$$

where V_{bso} is the velocity of a single bubble in stagnant water, and f_a is a factor that expresses the fact that the velocity of a swarm of bubbles is significantly lower than that of a single bubble (experimental data for several void fractions were taken from Govier & Aziz, 1972).

The velocity of a single bubble in stagnant water is expressed by Govier & Aziz (1972: 367) or Wallis (1969: 250) as

$$V_{bso} = 0.33 g^{0.76} \left(\frac{\rho_w}{\mu_w} \right)^{0.52} \left(\frac{d_b}{2} \right)^{1.28} \quad (\text{Eq. 58})$$

where μ_w denotes the dynamic viscosity of water (in $\text{N} \cdot \text{s} \cdot \text{m}^{-2}$) and d_b the bubble diameter (in m). Note: all values must be expressed in SI units. The diameter of bubbles close to the wall at the position of the photo-transistors, measured using a stroboscope, was found to be 1.6-2.3 mm.

The velocity of the air slugs, V_s , in the case of slug flow is much higher than the volume-averaged air velocity, V_a , as the small bubbles

between the slugs have a much lower (or even a negative) velocity. For the derivation of V_s , Equation (56) must be adapted:

$$V_s = C_0 V_M + C_2 V_{ss} \quad (\text{Eq. 59})$$

where V_{ss} denotes slug velocity in stagnant water. C_2 describes the fact that the velocity of a slug is influenced by the wake of the preceding slug (Wallis, 1969: 292). V_{ss} can be obtained (Govier & Aziz (1972: 396) from the relation

$$V_{ss} = 0.346 \sqrt{gD} \quad (\text{Eq. 60})$$

For a circular pipe and fully developed flow holds that

$$C_0 = 1.2 \text{ (Reynolds number of } V_M = V_M D \rho_w / \mu_w > 8000) \quad (\text{Eq. 61a})$$

$$C_2 = 1 \text{ (Reynolds number of } V_M = V_M D \rho_w / \mu_w > 8000) \quad (\text{Eq. 61b})$$

The resulting slug velocity is given by

$$V_s = 1.2 V_M + 0.207 \text{ m}\cdot\text{s}^{-1} \quad (\text{Eq. 62})$$

Due to its extremely turbulent nature, froth flow is not described theoretically; no relevant experimental studies on this flow pattern are known to the authors. At present it will be regarded as a modified form of slug flow.

Table 5 shows the theoretical velocities that are considered for comparison with the velocities measured by noise correlation. The void fraction is assumed to be constant throughout the length of the tube.

Table 5
Theoretical and experimental velocities (m·s⁻¹).

flow type	α (%)	theoretical velocities				experimental velocities		
		V_w	V_a	V_M	V_b, V_s	V_{CCF}	V_{phase}	ΔV (%)
bubbly	0.33	0.20	0.27	0.22	0.38-0.45	0.416	0.414	0.34
	0.34	0.16	0.26	0.20	0.35-0.42	0.384	0.383	0.18
slug	0.38	0.21	0.48	0.31	0.58	0.628	0.633	-0.84
	0.45	0.24	0.51	0.36	0.64	0.732	0.737	-0.68
froth	0.55	0.29	1.12	0.75	(1.11)	1.35	1.38	-1.6
	0.77	0.57	1.16	0.102	(1.43)	1.73	1.77	-2.2

Thus only air velocity is affected by the difference in pressure at the tube inlet and outlet. Bubble velocity, V_b , is calculated for a bubble diameter of 1.6 and 2.3 mm, using Equations (56)-(58) and assuming the bubble diameter to be constant over the entire tube cross-section. The 'slug' velocities for froth flow are given between brackets as the equation used (Eq. 62) has not been proved to be valid for this flow pattern.

Velocities obtained by noise correlation

Two methods are commonly used to derive the velocity of the signal disturbance from the noise component of the signals of two axially separated detectors (Thie, 1981):

- (1) Determination of the CCF of the two signals. This function has its maximum at the lag-time equal to the time that it takes the signal disturbance to go from the lower to the upper detector.
- (2) Determination of the phase spectrum of the complex CPSD of the two noise signals. The transit time is given by its linear slope.

The distance between the two detectors being known, the velocity of the signal disturbance can be derived. Both methods will be used here. The maximum of the CCF is determined by fitting the maximum of the discrete CCF and its two neighbouring values to a parabola. A phase-extrapolation code is used to determine the phase for values higher than $|180|^\circ$. The phase spectrum is then fitted to a straight line by means of a least-squares method, using the variance of the phase (that can be derived from the coherence) as a weighting factor.

The linearity of the phase is strongly influenced by the type of data (or its equivalent lag) window used, a fact which is often overlooked (see Harris, 1978, for a detailed description of the use of windows). Lag windows symmetrical about $t = 0$ are in quite common use. They were designed to provide a better estimate of auto spectra. For the determination of the cross spectrum in case of a transit time, however, such a window disturbs the symmetry of the CCF and favours small delays. The estimated velocity determined from the CCF will be too high and the phase spectrum will be distorted, as only a symmetrical CCF leads to a linear phase. It is clear that a lag window symmetrical about the expected transit time must be used. The use of such a window is called alignment (Priestley, 1981). The influence of alignment on the phase and coherence spectrum is demonstrated in Figure 25.

Table 5 presents the velocities derived from the fitted phase spectrum and the fitted CCF. A Hanning data window was used in combination with alignment to determine the CCF and the CPSD. The difference between these velocities (denoted by ΔV in Table 5) is less than 1% for bubble and slug flow. However, using the phase spectrum might be disadvantageous as the choice of the frequency interval over which the phase is fitted to a straight line is subjective.

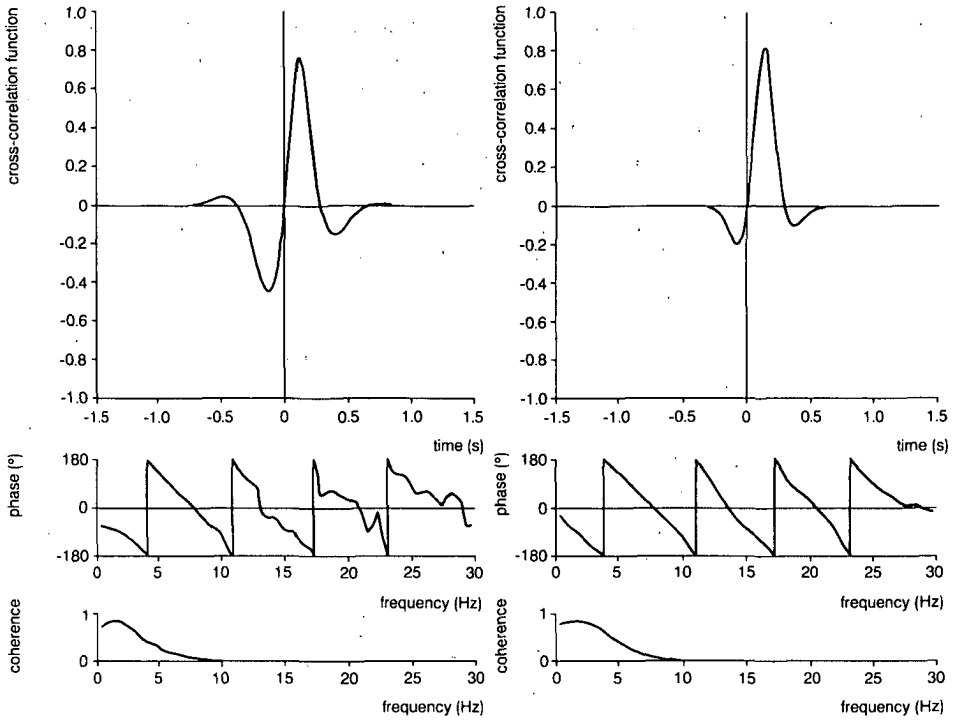


Fig. 25
 Cross-correlation function (CCF), phase and coherence (γ^2) of two photo-transistor signals.
 Left: without alignment: $V_{CCF} = 77.2 \text{ cm}\cdot\text{s}^{-1}$, $V_{\text{phase}} = 77.7 \text{ cm}\cdot\text{s}^{-1}$.
 Right: with alignment: $V_{CCF} = 74.6 \text{ cm}\cdot\text{s}^{-1}$, $V_{\text{phase}} = 75.4 \text{ cm}\cdot\text{s}^{-1}$.

A comparison of the theoretically derived velocities and the velocities obtained by fitting the CCF is given in Figure 26.

It is clear from this figure and from Table 5 that the measured velocity is considerably higher in all cases than V_w , V_a and V_M (which are

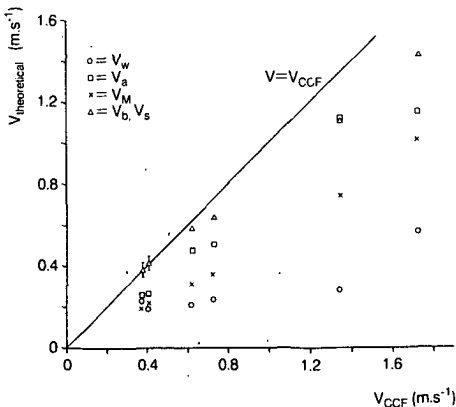


Fig. 26
 Theoretical water velocity (V_w), air velocity (V_a), volumetric flux (V_M), bubble velocity (V_b) and slug velocity (V_s) compared with the velocity derived by noise correlation (V_{CCF}).

featured as an interpretation by other authors). For bubbly flow, the measured velocity is equal to the calculated velocity of bubbles without wall interaction, V_b . Apparently the centre of the tube, where there is no wall interaction, is the dominant part for the experimental velocity which is formed from a complicated mixture of the relaxation length of the light, the detector field-of-view (the field-of-view is very narrow near the tube wall, where the slow bubbles are rising), bubble diameter and coherence between the two signals. The velocity of bubbles near the tube wall was measured visually by means of a stopwatch.

This measurement was quite accurate (standard deviation $\sigma(V_b) < 3\%$) and resulted in $V_b = 0.28 \text{ m}\cdot\text{s}^{-1}$ ($\alpha = 33\%$) and $V_b = 0.27 \text{ m}\cdot\text{s}^{-1}$ ($\alpha = 34\%$). This indicates that the velocity of those bubbles is indeed much influenced by the tube wall. The average air velocity V_a is low, due to the large contribution of the velocity of those bubbles. The unexpected fact that V_a is actually lower than V_b near the tube wall is attributed to measuring inaccuracies or to the existence of smaller bubbles whose velocity will be lower than the measured V_b .

The measured slug velocity, V_{CCF} , is higher than the theoretical velocity V_s . This is attributed to the fact that the slug pattern in the tube consists of fully developed as well as undeveloped slugs, which rise faster. The theory describes developed slugs, whereas V_{CCF} is an average of the velocities of developed and undeveloped slugs, and is therefore higher than V_s . The slug velocities were measured visually by making recordings with a video camera and by using a stopwatch. This resulted in a range of velocities ($0.53\text{-}0.66 \text{ m}\cdot\text{s}^{-1}$ for $\alpha = 38\%$ and $0.61\text{-}0.79 \text{ m}\cdot\text{s}^{-1}$ for $\alpha = 45\%$) that covers V_s and V_{CCF} .

Conclusions

The velocities measured by noise correlation in an air/water loop are much higher than the volume-averaged water and air velocity and the volumetric flux, which are usually offered as interpretation.

For bubbly flow, the velocity as obtained by noise correlation corresponds with the theoretically derived velocity of bubbles without wall interaction. For a better understanding of the measured velocity, detailed knowledge of the bubble and velocity profile over the tube cross-section is needed. Research is ongoing in this direction. An independent experimental method indicated that, in the case of slug flow, the measured velocity is the average velocity of developed and undeveloped slugs.

To obtain an insight into the coolant flow through a reactor core, one needs to know not only the steam velocity but also the distribution of the steam, i.e. the flow type. The flow type of interest in this air/water loop could be determined by using the probability density function of the photo-transistor signals; application of this method for a BWR, however, needs further study.

Acknowledgement

The simulation of a neutron field by UV-irradiated fluorescent material was originally suggested by E.B.J. Kleiss. The authors wish to express their gratitude to J.G.F. Schut and D.W. de Haas for their contribution to the hardware part of the experiments.

References

- Albrecht, R.W., R.D. Crowe, D.J. Dailey, M.J. Damborg & G. Kosaly 1982 Measurement of two phase flow properties using the nuclear reactor instrument – *Progress in Nuclear Energy* 9: 37-50.
- Govier, G.W. & K. Aziz 1972 *The flow of complex mixtures in pipes* – Van Nostrand Reinhold Company (New York): 792 pp.
- Harris, F.J. 1978 On the use of windows for harmonic analysis with the discrete fourier transform – *Proceedings of the Institute of Electrical and Electronics Engineers (IEEE, New York)* 66: 51-83.
- Jenkins, G.M. & D.G. Watts 1968 *Spectral analysis and its applications* – Holden-Day (San Fransisco): 525 pp.
- Lübbesmeyer, D. 1983 On the physical meaning of the fluid velocity measured in BWRs by noise analysis – *Annals of Nuclear Energy* 10: 233-241.
- Lübbesmeyer, D. 1984 Experimental reactor noise - a review on noise-analytic measurements of thermohydraulic parameters in operating BWRs and their interpretations – *Progress in Nuclear Energy* 14: 41-93.
- Priestley, M.B. 1981 *Spectral analysis and time series* – Academic Press (London): 890 pp.
- Thie, J.A. 1981 *Power reactor noise* – American Nuclear Society (Illinois): 208 pp.
- Van Dam, H. 1976 Neutron noise in boiling water reactors – *Atomkern-energie* 27: 8-14.
- Van Dam, H. & E.B.J. Kleiss 1985 Response of incore γ -detectors to parametric fluctuations in a reactor core – *Annals of Nuclear Energy* 12: 201-207.
- Wallis, G.B. 1969 *One-dimensional two-phase flow* – McGraw-Hill (New York): 25-134.

Chapter 5

Fast measurements of the in-core coolant velocity in a BWR by neutron noise analysis

This chapter was published in *Annals of Nuclear Energy* 15: 439-448 (1988).

It describes a novel technique for the fast determination of the in-core coolant velocity, which enables monitoring of variations in coolant velocity. This technique is important for stability surveillance of the core because a decrease in thermal-hydraulic stability will cause more coolant-velocity variations.

FAST MEASUREMENTS OF THE IN-CORE COOLANT VELOCITY IN A BWR BY NEUTRON NOISE ANALYSIS

T. H. J. J. VAN DER HAGEN and J. E. HOOGENBOOM

Interfaculty Reactor Institute, Delft University of Technology, Mekelweg 15, 2629 JB Delft, The Netherlands

(Received 3 December 1987; in revised form 18 April 1988)

Abstract—A method to determine in-core coolant velocities from neutron noise within short time intervals has been developed. The accuracy of the method was determined by using a simulation set-up and by using signals of a twin self-powered neutron detector installed in the core of the Dodewaard BWR in the Netherlands. In-core coolant velocities can be estimated within 2.5 s with a standard deviation (due to statistics) less than 2.1%. The method is suitable for velocity monitoring as is shown by the application to a stepwise velocity change of the coolant in a model of a coolant channel of a BWR.

The presented technique was applied to determine the variations of the coolant velocity in the Dodewaard core during normal operation and during pressure steps. Only minor variations of the coolant velocity were detected during normal reactor conditions. An increase of those variations with pressure lowering—indicating a lower thermal hydraulic stability—could be detected. A clear velocity response to pressure steps could be determined which was also reflected in the cross-spectrum of the velocity with the vessel pressure and with the in-core neutron flux.

1. INTRODUCTION

Correlating the noise signals of two axially separated in-core detectors is a well-known and widely used technique to obtain information on the coolant flow through the fuel elements of a boiling water reactor (BWR). Consider the in-core detector pair as in Fig. 1. Rising steam bubbles will first affect the signal of the lower detector and thereafter that of the upper one. Therefore the signals of the two detectors are

correlated and can be used to estimate the transit time of the bubbles from the lower to the upper detector. When the distance between the two detectors is known, the steam velocity can easily be derived (Wach, 1973). The accuracy of this derivation depends on the correlation of the signals due to their disturbance by bubbles: global variations of the flux hamper the velocity determination as does a loss of correlation between the detectors (collapsing bubbles, newly formed bubbles etc.).

A new application of this technique is to estimate not only the average coolant velocity, but to look at variations of this velocity as well. As instabilities of the two-phase flow of the coolant through the core of a BWR will manifest themselves as more or less periodic changes of the coolant velocity, it is of interest to develop a technique for sufficiently accurate velocity measurements in short time intervals. Moreover, it is useful to examine the responses of the coolant velocity to operational changes.

2. FAST VELOCITY DETERMINATION

Since neutron detectors have a smaller field-of-view than detectors sensitive to gammas, they are relatively less influenced by global variations of the flux (Kleiss *et al.*, 1985) and are thus preferred for fast velocity

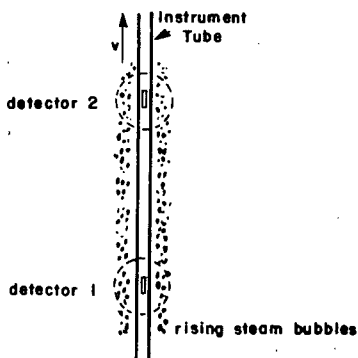


Fig. 1. An in-core detector pair.

determination. This small field-of-view has also a disadvantage: only velocities in the very corners of neighbouring fuel elements can be measured.

The fluctuations of the signals of the two detectors in Fig. 1, $\delta s_1(t)$ and $\delta s_2(t)$ can be split up in a coherent part $c(t)$ —assumed to be purely local—and a non-coherent part $\varepsilon_1(t)$, $\varepsilon_2(t)$:

$$\delta s_1(t) = c(t) + \varepsilon_1(t), \quad \delta s_2(t) = c(t - \tau) + \varepsilon_2(t), \quad (1)$$

τ denotes the transit time of the signal fluctuations to rise from the lower to the upper detector. In this case, the cross-correlation function (CCF) of the two signals is equal to the auto-correlation function (ACF) of the coherent part ACF_c at $t - \tau$ as can be seen from equation (2):

$$\begin{aligned} CCF(t) &= \langle \delta s_1(t') \delta s_2(t' + t) \rangle \\ &= \langle c(t') c(t' + t - \tau) \rangle = ACF_c(t - \tau). \end{aligned} \quad (2)$$

In which $\langle x \rangle$ denotes the time average of x .

As the $ACF_c(t)$ has its maximum at $t = 0$, the $CCF(t)$ has its maximum—equal to the variance of the coherent part—at $t = \tau$. The cross power spectral density (CPSD) of signals 1 and 2 is found after Fourier transformation of the CCF:

$$\begin{aligned} CPSD(f) &= \int_{-\infty}^{\infty} CCF(t) \exp(-j2\pi ft) dt \\ &= \int_{-\infty}^{\infty} ACF_c(t - \tau) \exp(-j2\pi ft) dt \\ &= APSD_c \exp(-j2\pi f\tau). \end{aligned} \quad (3)$$

In which $APSD_c$ denotes the auto-power spectral density of the coherent part. Thus the phase of the CPSD is a linear function of frequency.

Equations (2) and (3) lead to two methods of velocity determination using neutron noise that receive consideration for fast velocity measurements.

1. Determining the position of the maximum of the CCF of the noise of the two detector signals, since this function will peak at a time displacement equal to the time required for the signal to go from the lower to the upper detector [equation (2)]. The position of the maximum can be calculated by using e.g. a parabolic fit of the maximum of the discrete CCF and its two adjacent values.
2. Fitting the phase of the CPSD of the noise of the two detector signals to a straight line. The slope of this line is equal to $2\pi\tau$ [equation (3)]. As the phase of the CPSD can only be deter-

mined from $-\pi$ to π , jumps of 2π have to be eliminated by an extrapolation procedure.

Figures 2a, b give a comparison between the two methods for different values of the coherence between the signals of the two detectors. The signals were not derived from neutron detectors but were obtained by delaying white noise and adding (disturbing) noise to lower the coherence. In this way, a flat coherence function was obtained. The averaged coherence (bandwidth 0–30 Hz) and the computed delay times are given below each graph. From these figures it is clear that—even for low coherence—both methods are satisfactory for stationary velocity measurements.

For fast velocity measurements, however, the measuring time must be short and therefore the number of records is limited to a few (it is quite common to divide the sampled data in series of consecutive samples, called records, in order to obtain better spectral estimates). Thus the uncertainty in the phase and the CCF will be high.

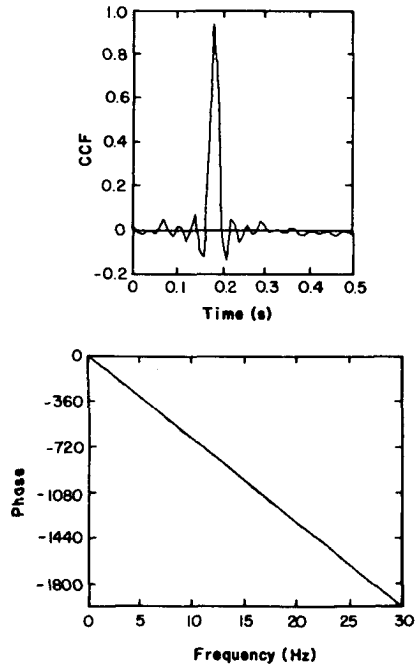


Fig. 2a. Transit time determination by means of the CCF and the phase of the CPSD (40 records of 512 samples) in case of an averaged coherence of 0.892. $\tau_{CCF} = 181.0$ ms (parabolic fit); $\tau_{phase} = 181.2$ ms.

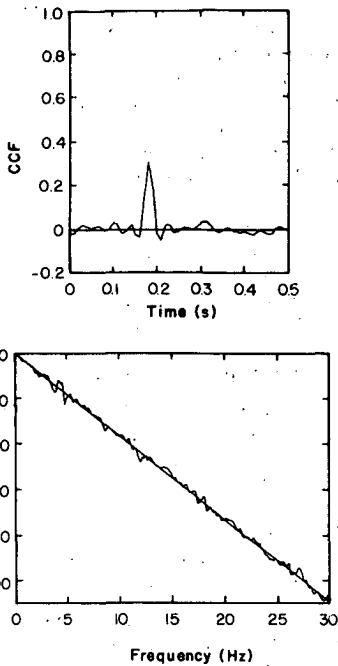


Fig. 2b. As Fig. 2a—averaged coherence = 0.121. τ_{CCF} = 180.9 ms (parabolic fit); τ_{phase} = 181.3 ms.

Figures 3a–d give the coherence, the phase and the CCF for the signals of the two detectors of a twin self-powered neutron detector (TSPND), installed in the core of the Dodewaard reactor. The TSPND consists of two self-powered neutron detectors mounted in line to a common signal/drive cable, positioned 10.0 cm from each other. A more extensive description of this detector set was given by Kleiss and van Dam (1981). The first two figures are based on an analysis of 1000 records; the last two use only one record (sampling time = 6 ms, 256 samples record⁻¹). It can be clearly seen that the global component, which is mainly present below a few Hz, hampers the determination of the transit time by the CCF. This problem is relaxed by high-pass filtering, as can be seen in Fig. 3b (this filtering nullifies the advantage of using the coherence function (Kostic, 1980); moreover, using this function needs much more computing time).

The sharpness of the CCF-maximum can be judged by calculating the second-order coefficient of the parabolic fit, that is A in $y = Ax^2 + Bx + C$. The higher the

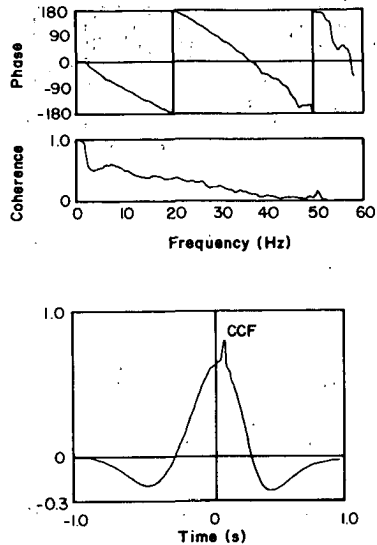


Fig. 3a. Phase of the CPSD, coherence and CCF of TSPND signals—1000 records.

absolute value of A , the sharper the CCF peak. This coefficient and a comparison between the transit time determination are given in Table 1. When only record is used, that is the analysis time is reduced to 1.5 s, the information on the velocity in the phase diagram is scattered. This hinders a correct elimination of the 2π phase jumps and the determined transit time depends therefore strongly on the chosen frequency interval. The CCF however, has its information concentrated, as it consists of an integration of the total spectrum (Fig. 3d).

An aspect of considerable importance is the computing time involved, as it is desirable to determine

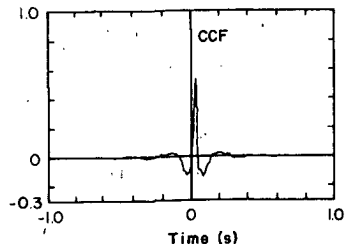


Fig. 3b. CCF after high-pass filtering (break frequency = 4 Hz).

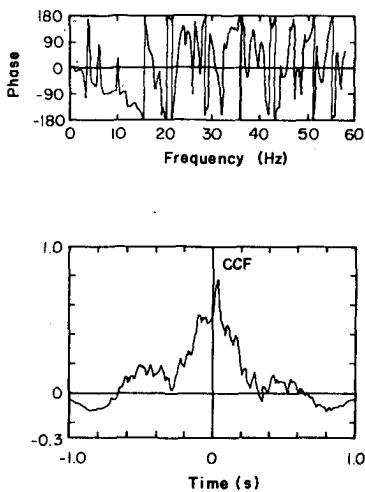


Fig. 3c. Phase of the CPSD, coherence and CCF of TSPND signals—1 record.

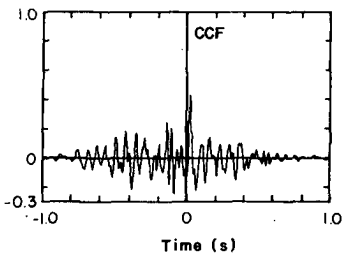


Fig. 3d. CCF after high-pass filtering (break frequency = 4 Hz).

the velocity in real-time. Since only the time delay of the maximum of the CCF is of interest, it suffices to determine the CCF for time displacements around the expected transit time (hereafter called CCF-interval). As a fast Fourier transformation is necessary for method 2, much more computing time is needed than in the case of the straightforward CCF-determination.

The above mentioned findings lead to the conclusion that method 1, using the CCF, is preferred for fast velocity measurements.

In order to get an impression of the variation of the velocity as a function of time, the velocity must be calculated as fast and as accurately as possible. These two conditions are of course contradictory, therefore a compromise must be used.

Each velocity point is determined by:

- Averaging the CCF of the sampled data over a certain time interval T ; in formula:

$$CCF(k) = \frac{\Delta}{T} \sum_{i=1}^{T/\Delta} s_1(i\Delta) s_2[(i+k)\Delta], \quad (4)$$

Δ denotes the sampling time.

- Calculating its maximum by a parabolic fit.
- Repeating the procedure for data Δ_v seconds later.

As Δ_v can be chosen equal to the sampling time Δ , the velocity can be determined after every new sample. However, the averaging of the CCF over T seconds is in fact an averaging of the velocity and acts like a low-pass filter. The transfer function of the averaging is:

$$H(f) = \int_{-\infty}^{\infty} h(t) \exp(-j2\pi ft) dt = \frac{T \sin(2\pi f T)}{\pi f T}, \quad (5)$$

with: $h(t) = 1$ for $-T/2 \leq t \leq T/2$,

= 0 elsewhere.

It is clear that frequencies higher than $1/T$ Hz hardly pass this filter. Therefore a suitable sampling frequency of the velocity is $2/T$ Hz ($\Delta_v = T/2$ s): lower

Table 1. Results of transit time determination from the phase of the cross-spectrum and from the cross-correlation function (see Fig. 3a-d)

Number of records	Filtering	Phase fitting Frequency band	τ (ms)	Parabolic fit of CCF	
				A (s^{-2})	τ (ms)
1000	—	0-40	25.2	-7×10^2	25.2
		0-30	24.5		
1000	High-pass	0-40	26.3	-26×10^2	26.7
		0-30	25.7		
1	—	0-15	28.8	-8×10^1	27.7
		0-12	29.8		
1	High-pass	0-15	34.8	-33×10^2	25.6
		0-12	21.2		

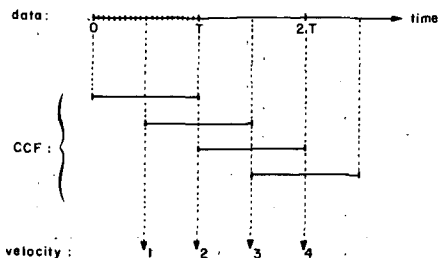


Fig. 4. Scheme of the technique for fast velocity determination.

sampling frequencies will give aliasing of frequencies higher than the corresponding Nyquist frequency, higher sampling frequencies will give no extra information; only interpolated velocity values will be added. This optimum sampling frequency produces a velocity point every $T/2$ s (Fig. 4).

3. VELOCITY MONITORING

3.1. Accuracy

Software was written for velocity monitoring. For this application the velocity is determined after every new sample, that is $\Delta v = \Delta$ instead of $T/2$. This introduces an extra correlation between successive velocity values (Section 2) but makes it easy to discover velocity trends. By using this program, the influence of the coherence on the accuracy of the determined velocity was observed.

For this reason the set-up as in Fig. 5 was used. Signal 1 consists of low-pass filtered white noise whereas the other is a mixture of this signal and

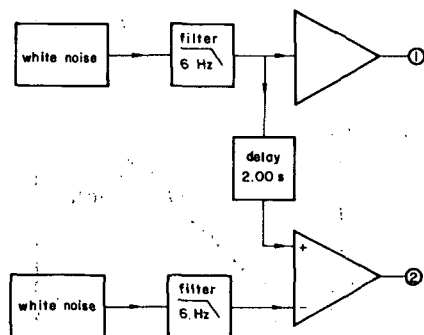


Fig. 5. Block-diagram of the set-up for determining the influence of the coherence on the accuracy of the velocity.

additional noise. The strength (r.m.s.-value) of this latter noise source could be varied in order to vary the coherence between the two signals. The used sampling time was 60 ms and the number of points over which the CCF was averaged was 128.

Figures 6a-c present the CCF (normalized to 1 at maximum value) used to obtain a certain velocity value and the determined velocity as a function of time for an averaged coherence (0-6 Hz) $\langle \gamma^2 \rangle = 0.93$, 0.44 and 0.07, respectively. In order to obtain an accurate value of the coherence, much more analysis time was used than for the determination of the CCF: 100 records of 128 samples of 60 ms. The CCF was determined only for a time interval around the delay time ($\tau = 2.00 \pm 0.01$ s). The distance between the simulated detectors was taken arbitrarily 1 m to obtain a velocity of 0.5 m s^{-1} .

There is a remarkable difference between the velocity plot for $\langle \gamma^2 \rangle = 0.07$ and the other two. The velocity jumps from one value to another for this low coherence (Fig. 6c). In this case the CCF consists of several high peaks: the maximum of the CCF jumps therefore from one peak to another. Due to the inter-

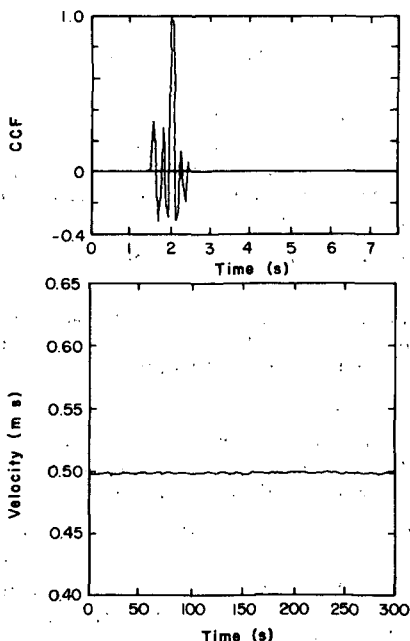


Fig. 6a. CCF used to obtain a certain velocity value and the velocity as a function of time for $\langle \gamma^2 \rangle = 0.93$.

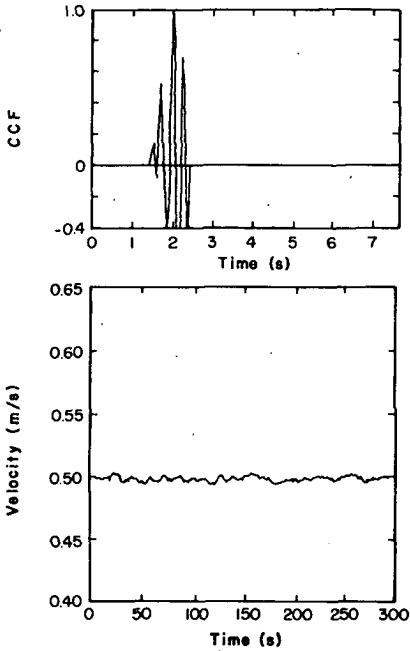


Fig. 6b. As Fig. 6a. $\langle \gamma^2 \rangle = 0.44$.

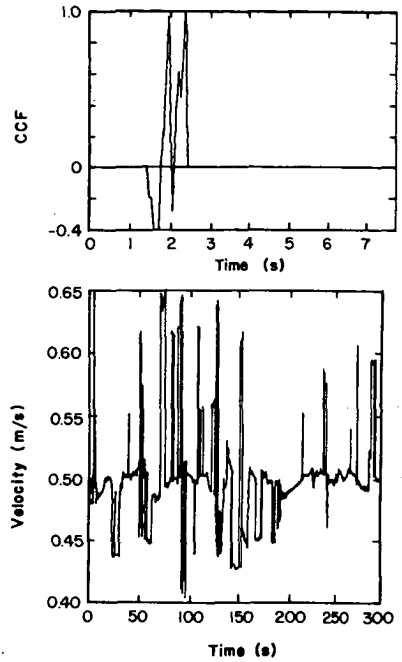


Fig. 6c. As Fig. 6a. $\langle \gamma^2 \rangle = 0.07$.

polation of velocity values, the velocity does not jump very wildly, but has a tendency to stay at a certain mean value. The standard deviation (σ) of the phase of the cross-spectrum depends on the coherence (γ^2) (Jenkins *et al.*, 1968):

$$\sigma_{ph}(f) \propto \sqrt{1/\langle \gamma^2 \rangle - 1}, \quad \propto = \text{proportional to.} \quad (6)$$

Since the coherence function is in this case flat for the analyzed frequency band, there holds for the standard deviation of the determined delay time:

$$\sigma_s \propto \sqrt{1/\langle \gamma^2 \rangle - 1}. \quad (7)$$

On the assumption that both methods (phase-fitting and CCF-maximum) have the same relation between standard deviation and coherence it is derived:

$$\sigma_v \propto \sqrt{1/\langle \gamma^2 \rangle - 1} \quad (V \text{ is considered to be constant}). \quad (8)$$

The estimated standard deviation s as a function of $1/\langle \gamma^2 \rangle - 1$ is given in Fig. 7 (the velocity was re-sampled using $\Delta_v = T/2$ in order to get rid of the extra correlation; $\gamma(f)^2$ was averaged over 0-6 Hz). Indeed relation (8) holds for $\langle \gamma^2 \rangle \geq 0.11$. For lower

coherences s increases enormously due to the several high peaks in the CCF and does not correspond with relation (8) anymore. (NB: $\sigma_s/s \approx 1/\sqrt{2n} \approx 8\%$, n is the number of velocity points).

The above mentioned results show the importance

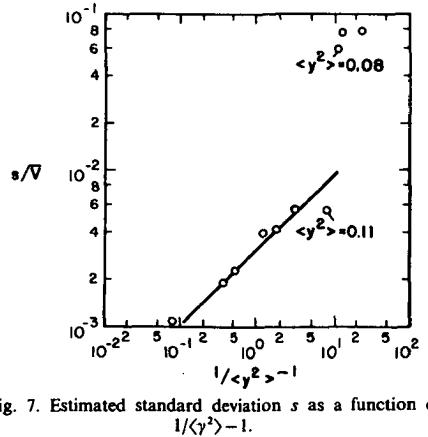


Fig. 7. Estimated standard deviation s as a function of $1/\langle \gamma^2 \rangle - 1$.

of the CCF-interval: a narrow interval will increase the accuracy but will not allow large velocity changes. This limitation can be overcome by using a moving CCF-interval: the delay time corresponding with the maximum of the CCF is the centre of the next interval. A disadvantage is that once the CCF-interval is—due to statistics—shifted outside the range of the delay time, it is purely accidental whether the interval will be shifted into this range again (a conservativity factor can be built in to minimize this effect: determine the ratio of the old CCF maximum and the new maximum and decide on this ratio where to place the next CCF-interval).

3.2. Velocity monitoring in practice

A nice example of velocity monitoring can be found in the application of fast velocity measurements to the velocity of an air-water mixture in a model of a coolant channel of a BWR. The model consists of a glass tube 2 m in height through which water is pumped upwards. At the bottom of the tube, air can be added to get a void fraction as high as 80%. The radiation from u.v.-light sources outside the tube excites a fluorescent powder that is dissolved in the water and that emits visible light when shone upon. In this manner visible light is produced in the water as are thermal neutrons by slowing down in the coolant of a reactor. Photo-transistors outside the tube register the emitted visible light and serve as a model for neutron or γ detectors, depending on their field-of-view (Kleiss *et al.*, 1985). They are not sensitive to the u.v.-light analogous to neutron detectors that merely detect the thermal neutrons.

The variations of the signals of two axially-separated photo-transistors were correlated to obtain the velocity of the air-water mixture. The physical interpretation of the measured velocity is not straightforward (Van der Hagen *et al.*, 1988). By keeping the water flow constant at 1050 l h^{-1} and suddenly increasing the air flow from 500 to 750 l h^{-1} , a stepwise change in the velocity could be created. Stationary measurements indicate a velocity of 0.73 m s^{-1} at 500 l h^{-1} and 1.15 m s^{-1} at 750 l h^{-1} air flow. The coherence of the signals of the two photo-transistors (at a distance of 10.0 cm above each other) at 500 l h^{-1} air flow is shown in Fig. 8. This sudden change in velocity is quite well detected applying fast velocity measurements ($\Delta = 30 \text{ ms}$, $128 \text{ samples record}^{-1}$, $\Delta_v = \Delta$) as can be seen, in Fig. 8. The determined velocity at the higher air flow is fluctuating more than at the lower flow due to the turbulent nature of the flow type at these operating conditions.

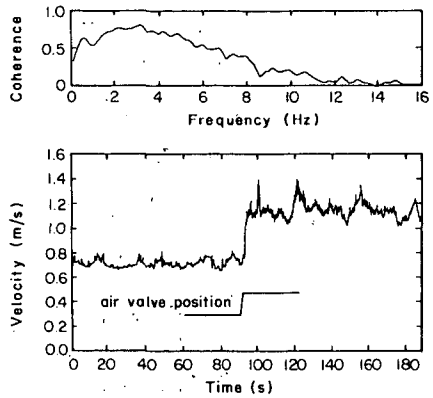


Fig. 8. Coherence of the two photo-transistor signals and the measured velocity response to a stepwise increase of the air flow.

4. ESTIMATED ACCURACY IN A BWR

A lower limit of the accuracy of the method can be found by fitting the phase of the cross-spectrum to a straight line by the least-squares method and determining the standard deviation of this fit. This standard deviation is partly formed by statistics which represent the accuracy of the method and partly by true changes of the velocity.

When the number of records N used for the analysis is decreased, the importance of velocity changes to the standard deviation decreases (only low-frequency velocity changes are expected) whereas the statistical standard deviation increases ($\sigma \propto 1/\sqrt{N}$). The limit of the standard deviation for one record forms an upper limit of the inaccuracy of the method.

Figure 9 gives the phase of the cross-spectrum of the two signals of a TSPND used in the Dodewaard core (174 MWth) for a decreasing number of records ($\Delta = 10 \text{ ms}$, $256 \text{ samples record}^{-1}$). The inverse variance of the phase was used as a weighting factor for phase fitting. This variance depends on the coherence according to equation (6); the most accurate value of the coherence, that is the one obtained by a 1000 records-analysis was used. Table 2 summarizes the results. The determined standard deviation for one record $\sigma^* = \sigma\sqrt{N}$ is indeed decreasing with the number of records (decreasing influence of velocity changes), as is expected.

As a conclusion it can be stated that the standard deviation for transit time determination by using the CCF ($\Delta = 10 \text{ ms}$, $256 \text{ samples record}^{-1}$, $\Delta_v = 1.28 \text{ s}$)

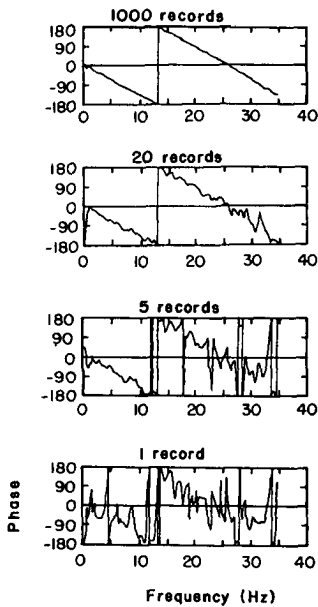


Fig. 9. Phase of the CPSD of TSPND signals for a decreasing number of records.

is less than 2.1% ; it will in fact be less than this value because there will still be some velocity changes in a time interval of 2.56 s that give a higher standard deviation than that due to pure statistics.

5. APPLICATIONS IN THE DODEWAARD BWR

5.1. Averaged velocity response

In the last two years experiments concerning signal responses to changes of the vessel pressure have been performed in the Dodewaard BWR (Van der Hagen

et al., 1986). In these cases the averaged responses of several reactor signals to vessel pressure and control rod steps were determined. Neither the feedwater nor the pressure was controlled during these measurements.

For the determination of the averaged response of the coolant velocity to a pressure step, two paths can be followed :

1. Calculate the CCF of TSPND-signals over a short time period for each response. Determine for each response the velocity by parabolic fitting of the CCFs maximum. Average the velocities. Repeat the procedure for the next time period.
2. Average the CCFs instead of the velocities and determine the maximum of the averaged CCF and thus the averaged velocity.

Since the main difference between the two methods is the computing time involved, method 2 was chosen.

Figure 10 displays velocity responses to a pressure step obtained in this way. The number of responses used for the averaging was 20, 276 samples per CCF, $\Delta = 10$ ms, $\Delta_v = 2.76$ s (thus not equal to $T/2$ in this case). The averaged velocity responses were smoothed over 3 points, this gives an effective sampling time for the velocity Δ_v of 8.28 s. A clear response to pressure steps can be distinguished : a pressure increase leads to a velocity decrease and *vice versa*. For an evaluation of the velocity trends see Van der Hagen *et al.* (1986).

5.2. Fast velocity measurements

5.2.1. *During normal operation.* Fast velocity measurements were performed under two conditions :

at normal power and pressure : 174 MWth, 75.5 bar,

at normal power and lower pressure : 172 MWth, 70.5 bar.

The pressure and feedwater control were switched off in both situations. The pressure and the signals of a TSPND were sampled with $\Delta = 10$ ms. Using the

Table 2. Standard deviation of the transit time derived by phase-fitting. σ^* is the standard deviation for one record $= \sigma\sqrt{N}$

Number of records (N)	τ (ms)	σ (%)	σ^* (%)
1000	38.1	0.07	2.21
500	38.1	0.10	2.21
200	38.1	0.16	2.21
100	38.2	0.22	2.20
50	38.2	0.31	2.20
20	38.3	0.49	2.20
10	38.4	0.69	2.19
5	39.3	0.96	2.14
2	39.7	1.50	2.12
1	40.4	2.09	2.09

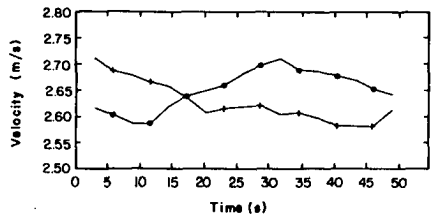


Fig. 10. Averaged in-core coolant velocity response to a pressure step change at $t = 0$. (+) 69 \rightarrow 72.5 bar; (O) 72.5 \rightarrow 69 bar.

CCF method described in Section 2, the coolant velocity was calculated from the TSPND signals (128 samples CCF^{-1} , $\Delta_v = 640$ ms). The pressure and the in-core neutron flux were averaged over 128 samples also.

The auto power spectral density of the in-core coolant velocity (71 records of 128 samples) for the situation at normal pressure is given in Fig. 11. The coherence between the velocity and the pressure was found to be very low: averaged coherence (0–0.5 Hz) = 0.013. The standard deviation of the estimated velocity is 3.3%. The standard deviation of the method in the case of 256 samples CCF^{-1} was determined to be less than 2.1% (Section 4). Thus for this case:

$$\sigma_{\text{method}} \leq \sqrt{256/128} \cdot 2.1\% = 3.0\% \quad (9)$$

Thus the standard deviation found (3.3%) gives rise to assume a small contribution of velocity variations to the spectrum.

When the two processes—statistical inaccuracy and velocity variations—are assumed to be independent, the standard deviation of the velocity σ_v is given by:

$$\sigma_v = \sqrt{\sigma^2 - \sigma_{\text{method}}^2} \geq 1.4\% \quad (10)$$

As stability decreases with vessel pressure an increase of the standard deviation of the coolant velocity is expected for the situation at 70.5 bar. The standard deviation found with fast velocity measurements is 4.0%; thus—with equation (10)— $\sigma_v \geq 2.3\%$. This is indeed higher than for the normal situation. The averaged coherence between the velocity and the pressure is slightly higher than in the previous case

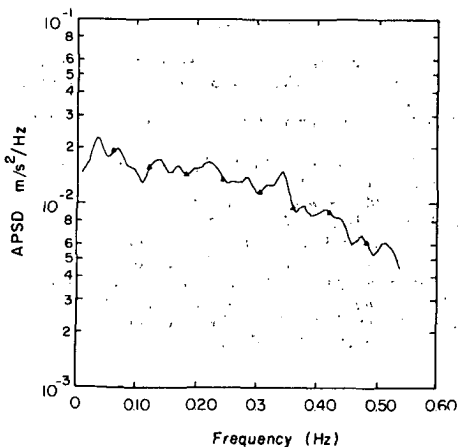


Fig. 11. Auto power spectral density of the in-core coolant velocity at normal reactor conditions.

(0.024). This points to more pressure-induced velocity variations.

Assuming that the accuracy of the method does not decrease with this pressure lowering, it can be argued that the lower stability of the system at low pressure is reflected in an increase of the standard deviation of the coolant velocity.

In order to obtain the spectrum of the velocity variations for frequencies around the core resonance frequency, being 1.1 Hz, the CCF of the TSPND signals was also estimated using 64 samples CCF^{-1} ($\Delta_v = 320$ ms). However, a strong decrease in accuracy of the velocity was found due to the influence of peaks in the CCF not originating from transit time phenomena (see also Section 3.1).

5.2.2. *During pressure steps.* As a clear velocity response was found to pressure steps it seems promising to apply fast velocity measurements to the signals of a TSPND during this experiment. The pressure was varied between 74.5 and 71.5 bar with a frequency of 2 mHz. The standard deviation of the velocity was determined using $\Delta = 10$ ms; 128 samples CCF^{-1} ($\Delta_v = 640$ ms) and found to be 3.5% ($\sigma_v \geq 1.8\%$); this is higher than the deviation at normal reactor conditions.

The spectra of the velocity, the pressure and the in-core neutron flux were determined using 256 samples CCF^{-1} ($\Delta_v = 1.28$ s). Figures 12a and b give the corresponding results (34 records of 128 samples). The coherence between velocity and pressure is high for frequencies below 20 mHz. This coherence was absent in the results at normal operating conditions. Notice that the phase of the cross-spectrum for this low-frequency region is -180° as is expected from the velocity responses dealt with in Section 5.1.

Also the in-core neutron flux shows a significant coherence with the velocity: Due to the twofold response character of the neutron flux to pressure change [a pressure increase leads to an increase of the flux during the first 20 s and thereafter to a decrease (Van der Hagen *et al.*, 1986)] the phase of the cross-spectrum is more complex.

6. CONCLUDING REMARKS

The ability to determine variations of the in-core coolant velocity is shown. The application of this method is twofold:

- When used for velocity monitoring, its field of application goes far beyond reactor physics. Two examples are mentioned: (a) a stepwise change of the velocity of the coolant through a model of a

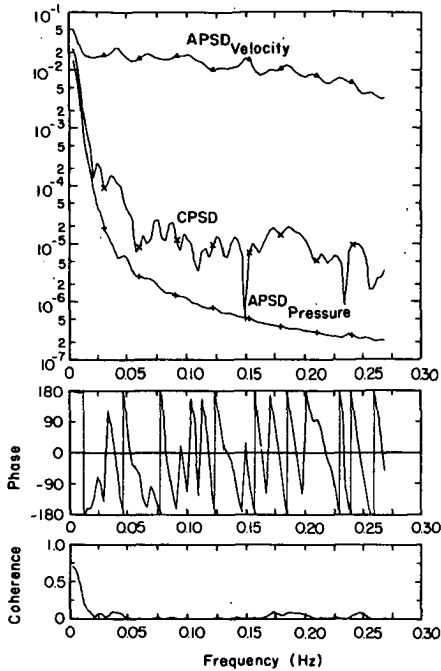


Fig. 12a. Spectra of the in-core coolant velocity ($\text{m}^2 \cdot \text{s}^{-2} \text{Hz}^{-1}$) and the vessel pressure (Hz^{-1}) during pressure steps.

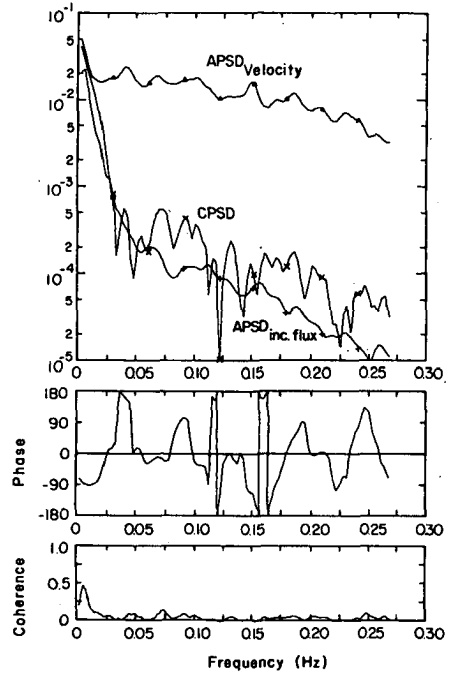


Fig. 12b. Spectra of the in-core coolant velocity ($\text{m}^2 \cdot \text{s}^{-2} \text{Hz}^{-1}$) and the in-core neutron flux (Hz^{-1}) during pressure steps.

BWR coolant channel could be detected very well; (b) the response of the coolant velocity in the core of the Dodewaard BWR to a pressure change could be determined.

- When applied to estimate the variance of the in-core coolant velocity, the thermal hydraulic stability of the core can be judged. The decrease in stability of the Dodewaard BWR at pressure lowering is reflected in an increase of this variance.

Acknowledgement—The authors wish to express their gratitude to W.H.M. Nissen for his assistance during the Dodewaard experiments.

REFERENCES

- Jenkins G. M. and Watts D. G. (1968) *Spectral Analysis and its Applications*. Holden-Day, San Francisco, California, U.S.A.
- Kleiss E. B. J. and Dam H. van (1981) *Nucl. Technol.* **53**, 250.
- Kleiss E. B. J., Oosterkamp W. J. and Nissen W. H. M. (1985) *Prog. Nucl. Energy* **15**, 735.
- Kostic L. (1980) *Atomkernenergie* **35**, 20.
- Wach D. (1973) *Atomwirtschaft* **18**, 580.
- Van der Hagen T. H. J. J., Dam H. van, Hoogenboom J. E., Kleiss E. B. J., Nissen W. H. M. and Oosterkamp W. J. (1986) *Proc. of the 6th Power Plant Dynamics, Control & Testing Symposium*, Knoxville, Tennessee, U.S.A. 8.
- Van der Hagen T. H. J. J. and Voet J. van der (1988) To be published in *Prog. Nucl. Energy*.

Chapter 6

Determination of reactor stability by deterministic and stochastic methods

An extensive set of measurements was performed on the Dodewaard nuclear power plant in order to examine plant stability and other plant characteristics. The experiments were carried out during the cycle start-up and at nominal reactor power. They comprised both stochastic and deterministic methods: noise analysis and analyses of responses of relevant process variables to stepwise changes in control-rod position and steam-flow control-valve position, respectively.

As was mentioned in Chapter 1, three types of reactor stability can be distinguished which could be observed separately in the above-mentioned experiments: reactor-kinetic stability, thermal-hydraulic stability and total-plant stability. It should be stressed that the term 'stability' as used here refers to the phenomenon of a damped oscillatory response to system perturbations; smaller damping means lower stability (see Chapter 1).

A decrease of reactor-kinetic stability has its origin in the interaction of neutron dynamics and the thermal-hydraulic feedback mechanism. This type of stability is reflected in the reactivity-to-power transfer function (see Chapter 1).

The reactivity-to-power transfer function was measured in two ways: from the response to control-rod steps and by using the frequency- and space-dependent coherence of the signals of three ex-vessel neutron detectors.

Thermal-hydraulic stability (also called 'channel-flow stability' or 'local stability') deals with the two-phase flow dynamics of a heated channel. A decrease in this type of stability manifests itself as an increased noise-source strength, but does not affect the reactivity-to-power transfer function of the core (see Chapter 1).

Thermal-hydraulic stability was also measured in two ways: it was derived both from the shape of the noise spectrum of neutron-detector signals and from the damping ratio of the impulse response of the ex-vessel neutron flux as obtained by autoregressive (AR) analysis methods.

Finally, total-plant stability was studied by measuring the responses of several signals to steam-flow control-valve steps.

Experimental conditions

The pressure control was switched off throughout all the experiments.

The set of deterministic experiments consisted of control-rod steps aimed at causing a reactivity disturbance, and of steam-flow control-valve steps that excited the core as a whole via the reactivity effect of the pressure.

The central control rod D4 (Fig. 2) was chosen to obtain a maximum reactivity effect. This rod was moved periodically between two positions in the core around the flux maximum. The movement had a range of 8 cm and caused a change of 1 MW peak-to-peak in thermal reactor power. Its period was 4 minutes. The control valve was moved at the same time intervals as the rod and caused pressure fluctuations of 400 kPa (from 7.4 to 7 MPa and vice versa).

The central fuel bundles were surrounded by two detectors: a twin self-powered neutron detector (see Chapter 3) positioned at detector position 4D at an axial position 1.03 m above the core bottom and a neutron

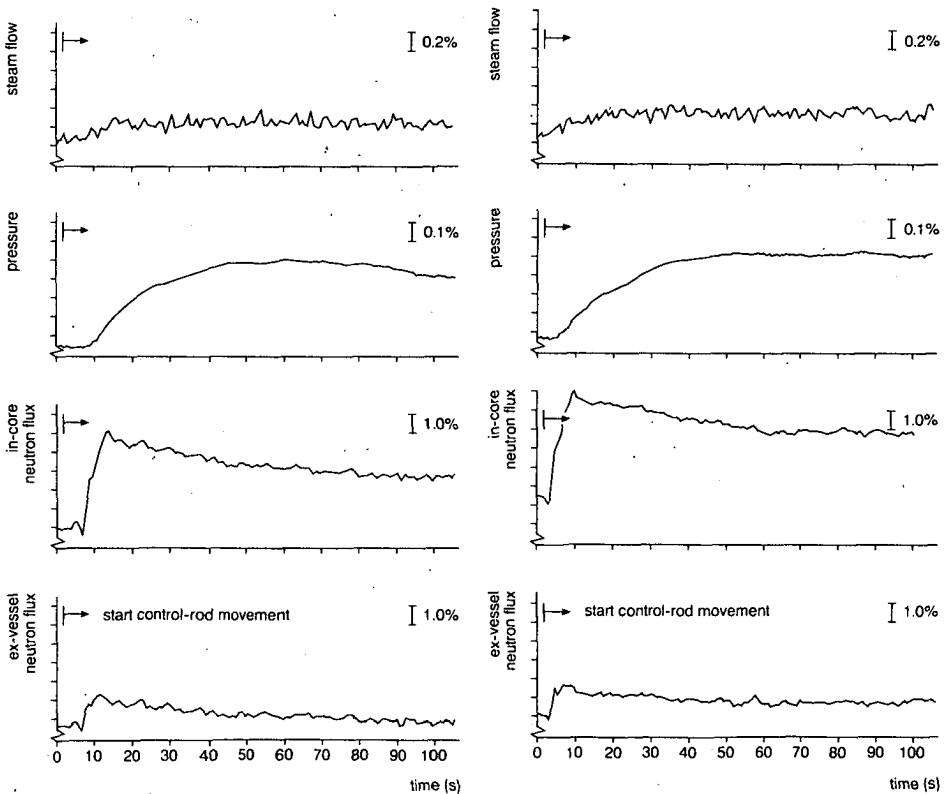


Fig. 38
Averaged signal responses to a control-rod withdrawal.
Left: at 7.4 MPa vessel pressure.
Right: at 7.0 MPa vessel pressure.

detector positioned at the same axial position as the top of control rod D4 (i.e. 0.56 m above the core bottom) at detector position 4C (Fig. 2).

Evaluation of the experimental results

This section deals with

- (1) reactor-kinetic stability,
- (2) thermal-hydraulic stability,
- (3) total-plant stability,
- (4) stability during the cycle start-up phase.

Reactor-kinetic stability – The reactivity-to-power transfer function (RTF) is defined as the transfer function between reactivity input and power output. It can be obtained from the results of the control-rod experiments.

Figure 38 gives the responses of several signals averaged over 35 to 40 steps, to control-rod insertion at a reactor pressure of 7.4 and 7.0 MPa.

The reactivity input signal caused by the movement of the control rod was not measurable directly as the exact movement of the rod in the Dodewaard reactor is not known, but it could be estimated from the local component of the in-core neutron-detector signal, as this reflects the flux changes near the control rod. Figure 39 shows the two-fold effect of control-rod movement with respect to the detector responses. The coefficients a , b , c and d in this figure are constant for small rod movements.

The local component was derived from the difference between the in-core signal and the signal of an ex-vessel neutron detector, as the last is influenced only by the global (reactivity) effect of the movement. The signals were normalised to their steady-state values in order to obtain relative responses. The RTFs obtained after Fourier transformation of this input signal and the ex-vessel flux, which served as the output signal, are represented in Figure 40 (dots with 2σ error bars). It is obvious that these RTFs do not exhibit a resonance peak. This is an indication of proper reactor-kinetic stability. Furthermore, the conclusion can be drawn that lowering the pressure from 7.4 to 7.0 MPa has no significant effect on the RTF.

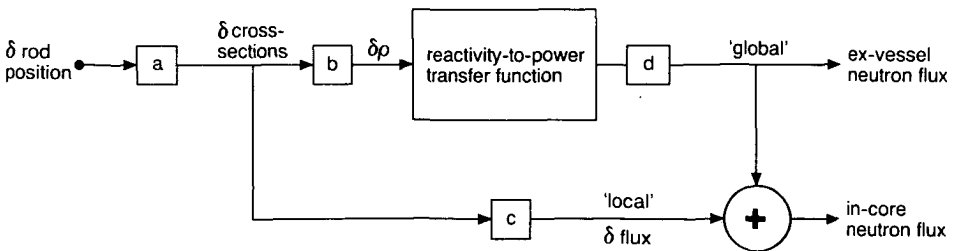


Fig. 39

Block diagram of the effect of a control-rod movement on the neutron flux. For small movements a , b , c and d are constants.

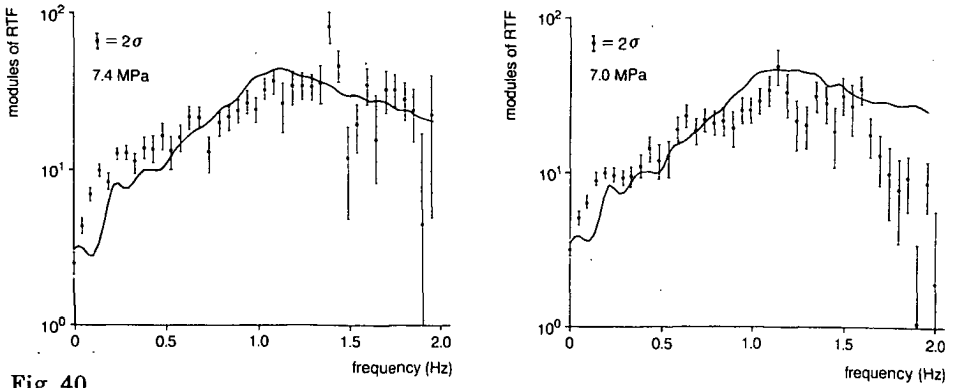


Fig. 40

Modulus of the reactivity-to-power transfer function, determined from the response to control-rod steps (dots) and from the space-dependent coherence of the ex-vessel neutron flux (curves). Note the (vertical) logarithmic scale (arbitrary units).

The RTF can also be estimated from the space dependence of the coherence of the neutron noise in the reactor core. The coherence is determined by the field-of-view of the detectors, that is in turn dependent on the RTF (Kleiss, 1982). The coherence between the noise signals of three ex-vessel detectors, situated as in Figure 2, was used for this purpose. The resulting RTFs are given in Figure 40 (curves). Again, the RTFs lack a resonance peak and the influence of pressure is slight. The above-mentioned results indicate good reactor-kinetic stability.

Thermal-hydraulic stability – The noise spectrum of an ex-vessel neutron detector is formed by a noise source, which reflects thermal-hydraulic stability, shaped by the RTF. Information on both types of stability can therefore be obtained by analysing the shape of the neutron noise spectrum (see also Upadhyaya et al., 1982).

Figure 41 shows the normalised auto-power spectral density (NAPSD) of the ex-vessel neutron flux (detector N6) measured at a vessel pressure



Fig. 41

Normalised auto-power spectral density of the ex-vessel neutron flux under normal reactor conditions.

of 7.4 MPa. This spectrum exhibits a peak at approximately 1.1 Hz, which peak is related to the thermal-hydraulic stability as the frequency corresponds with the time required by the two-phase coolant to travel from the bottom to the top of the core (Van der Veer, 1982). At least two significant peaks can be observed at lower frequencies: 0.017 Hz (Van der Veer, 1982) and 0.05 Hz. The origin of these peaks is not known but could lie in the total recirculation loop of the coolant. The total recirculation time of the coolant via the downcomer is approx. 19 s (see Chapter 8), corresponding with a resonance frequency of 0.05 Hz. The recirculation time of the flow through the by-pass between the fuel bundles (with a velocity of about $0.05 \text{ m}\cdot\text{s}^{-1}$: Oosterkamp, 1987) is approx. 54 s (36 + 18 s), which corresponds with a resonance frequency of 0.019 Hz.

Stability is much better at 0.017 and 0.05 Hz than at 1.1 Hz as can be seen from the relative full width at half maximum, which is approx. 1.2, 1.1 and 0.17, respectively. The peak at 1.1 Hz is the sharpest and indicates the worst stability, so that the stability analysis in this study was concentrated on this frequency range. Moreover, it is not necessary to use sophisticated means to survey the stability of the reactor in the low-frequency region, as such long-period oscillations will easily be detected by the safety channels.

It is obvious from Figure 42, which shows the NAPSD of the ex-vessel neutron flux for two vessel pressures, that the neutron-flux signal exhibits a broad peak at approx. 1.1 Hz, the height of which is dependent on the pressure. This is an indication of a decreased stability at lower pressure.

A better impression of the thermal-hydraulic stability is obtained by modelling the noise of the ex-vessel neutron flux with an autoregressive technique and then using this model to calculate the impulse response. This method is dealt with in detail in Chapter 8. It follows from the analysis described there that the decay ratio of the system is 0.17 at normal pressure (7.4 MPa) and 0.21 at lowered pressure (7.0 MPa). Damping of the system is thus lower at a lower pressure but reactor

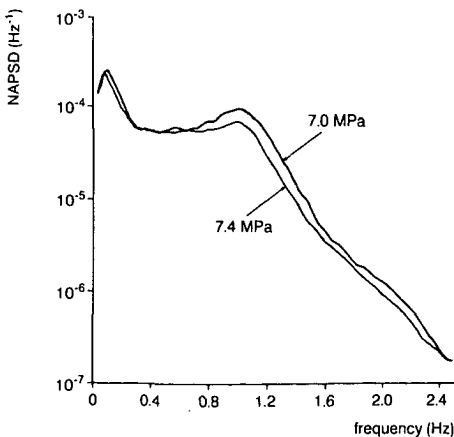


Fig. 42
Normalised auto-power spectral density of the ex-vessel neutron flux at 7.4 and 7.0 Mpa vessel pressure.

behaviour is still very stable. This effect is due to the larger void reactivity coefficient at lower pressures (Lahey & Moody, 1977).

Total-plant stability - Total-plant stability can be deduced from the response of the reactor to the pressure fluctuations caused by the control-valve movement. Figure 43 gives the main (averaged) signal responses to lowering of the pressure from 7.3 to 6.9 MPa at 172-MW reactor power. As a pressure decrease leads to a higher void fraction, which in turn leads to a power decrease, a positive pressure coefficient is to be expected. The neutron-flux response in Figure 43 indeed corresponds with this expectation during the first twenty seconds after movement of the control valve but gives an opposite indication of the pressure coefficient after this time. This surprising phenomenon, which improves load following, is attributed to the colder feedwater that reaches the core and increases reactivity and thus reactor power. This topic is taken up in more detail in Chapter 8.

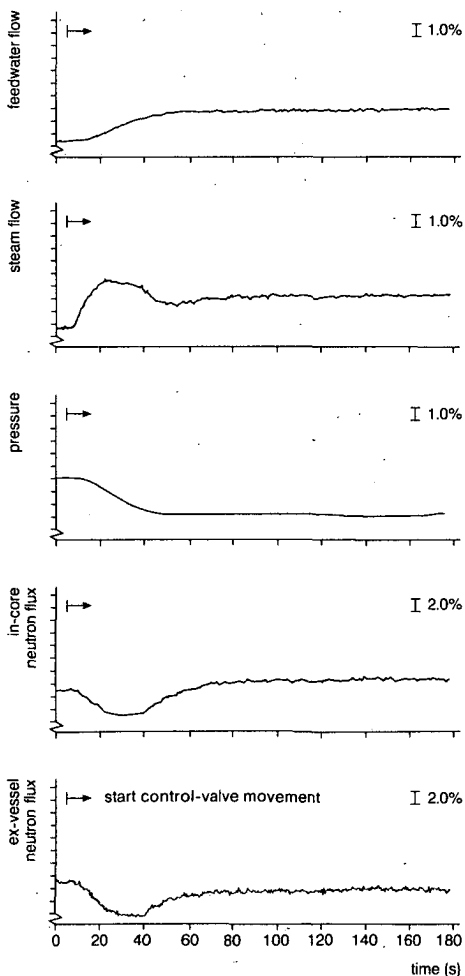


Fig. 43
Averaged signal responses to pressure lowering from 7.3 to 6.9 MPa.

Notice that the ex-vessel flux does not reach its initial level whereas the in-core flux stabilises at a higher level after a control-valve opening. This is due to an alteration of water density in the downcomer. A 1-K decrease in temperature leads to less carry-under and a lower density, therefore to more neutron absorption and consequently to a decrease of 1% in ex-vessel flux (W.H.M. Nissen, private communication, 1985).

Stability during the cycle start-up phase - Recordings were made during the start-up of cycle 18, February 1987, to examine the stability during this phase. Figure 44 presents the normalised auto-power spectral density of the signal of the ex-vessel neutron detector N5 for three situations during the start-up phase: 55% of nominal power and 7.0 MPa vessel pressure, 70% power and 7.5 Mpa, and 81% power and 7.5 MPa. It can be seen that, although the reactor was extremely stable during this phase, the spectrum increased with increasing power. This is due to the increase of the noise source formed by the turbulent two-phase flow through the core (see also Chapter 1).

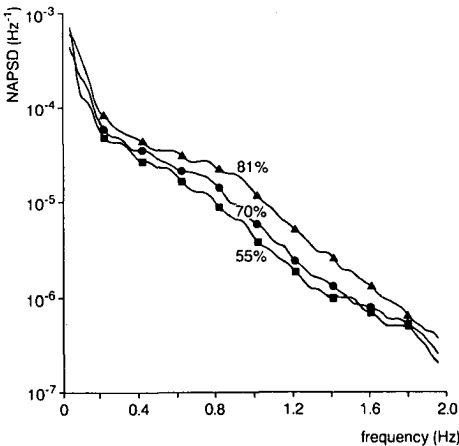


Fig. 44
 Normalised auto-power spectral density of the ex-vessel neutron flux during several phases of the start-up.
 Triangles: 81% power, 7.5 MPa.
 Dots: 70% power, 7.5 MPa.
 Squares: 55% power, 7.0 MPa.

Conclusions

A combination of noise measurements and analysis of responses to control-rod steps is a good means to study both reactor-kinetic and thermal-hydraulic stability.

Each type of stability was analysed in two ways. A satisfactory stability margin was assured at normal reactor power and vessel pressures of 7.0 and 7.4 MPa. Total-plant stability was observed in the response of the reactor to pressure fluctuations caused by pressure-control-valve steps. It appeared that, as expected, the reactor has a positive short-term pressure coefficient but a negative long-term pressure coefficient. This negative coefficient improves load following.

The reactor is extremely stable during the start-up phase; the strength of the noise source formed by the two-phase flow through the core increases with power and is reflected in an increasing ex-vessel neutron noise spectrum.

Chapter 7

Experimental and theoretical evidence for a short effective fuel time constant in a BWR

This chapter was published in *Nuclear Technology* 83: 171-181 (1988).

It describes the research performed on the effective fuel time constant. This constant is of vital importance for reactor-kinetic stability as it is a major parameter in the reactivity feedback loops.

It is shown that heat transfer from fuel to coolant contains a spectrum of fuel time constants and that reduction to a theoretical model with a single effective fuel time constant can yield erroneous results regarding the proper modelling of system dynamics.

EXPERIMENTAL AND THEORETICAL EVIDENCE FOR A SHORT EFFECTIVE FUEL TIME CONSTANT IN A BOILING WATER REACTOR

TIM H. J. J. van der HAGEN *Interfaculty Reactor Institute
Mekelweg 15, 2629 JB Delft, The Netherlands*

Received February 27, 1987

Accepted for Publication April 28, 1988

The effective time constant related to heat transfer from fuel to coolant is a very important parameter for the dynamic behavior and thus the stability of a nuclear reactor. Usually a single time constant of a lumped parameter model is used. Both experimentally, via two independent methods of analysis, and theoretically, it is determined that a more elaborate model, using two or three time constants, is necessary.

Heat transfer for high frequencies is governed by the small fuel time constants that stem from the outer region of the fuel. The bulk follows slow variations with time constants of >5 s.

I. INTRODUCTION

One of the important parameters for the system dynamics of a boiling water reactor (BWR) is the time constant related to time-dependent heat transfer from fuel to coolant—the fuel time constant. This constant becomes a dominant factor in all feedback loops of reactivity disturbance, such as feedback via fuel temperature, moderator temperature, and void fraction, and therefore plays an important role in the stability of the system. Moreover, it determines the temperatures of the fuel and its cladding during a transient, which are important values concerning system safety.

Whereas the low-frequency behavior of the system can be described using a single time constant, a more elaborate model must be used for time scales smaller than this lumped time constant.¹ Experiments indicated the necessity of a multitime constant model for the BWR of the Dodewaard nuclear power plant,² so the fuel time constant was examined both experimentally and theoretically.

II. LUMPED PARAMETER MODEL

In evaluating responses of the heat current from fuel to coolant to power changes in the fuel, the lumped parameter technique is often useful. This technique assumes the internal thermal resistance of a fuel rod to be negligibly small compared to the external resistance to heat transfer between the fuel rod and the coolant. This means that the fuel rod has a uniform temperature when axial effects are neglected.³ The transfer function H_f between power variations δP in the fuel and variations of the heat current δq from fuel to coolant can be derived using the heat balance:

$$\delta P(t) = c_f \rho_f V_f \frac{d\delta T_f(t)}{dt} + \delta q(t), \quad (1)$$

in which

c_f = specific heat capacity of the fuel (J/kg·°C)

ρ_f = density of the fuel (kg/m³)

V_f = fuel volume (m³),

with

$$\delta q(t) = \alpha A_f (\delta T_f - \delta T_c), \quad (2)$$

where

α = fuel-to-coolant heat transfer coefficient (J/m²·s·°C)

A_f = heat transfer area (m²)

T_c = coolant temperature (°C).

All variations are taken relative to their stationary values.

Variations of the coolant temperature can be neglected compared to fuel temperature fluctuations as the coolant in a BWR is at saturation temperature (the changes of the saturation temperature due to pressure

variations are very small as the pressure derivative of the saturation temperature is $0.9^{\circ}\text{C}/\text{bar}$ at 76-bar pressure):

$$\delta T_c = 0 \quad (3)$$

After Laplace transformation, one obtains

$$H_f(s) = \frac{\delta q(s)}{\delta P(s)} = \frac{1}{1 + s\tau_f} \quad (4)$$

in which

$$\tau_f = \frac{c_f \rho_f V_f}{\alpha A_f} \quad (5)$$

is the fuel time constant (in seconds) and s denotes the Laplace variable. Thus, this simple model results in a single time constant that describes the rate of heat current change after a power change.

For the heat transfer coefficient, α holds

$$\alpha = \frac{q''}{\Delta T} \quad (6)$$

where

ΔT = difference between the average fuel temperature and the temperature of the coolant

q'' = heat flux per unit of surface area ($\text{J}/\text{m}^2 \cdot \text{s}$).

The time constant for the Dodewaard fuel can be calculated using core-averaged plant data for ΔT (Ref. 4) and literature values for c_f and ρ_f (Refs. 5 and 6):

$$\tau_f = 4.6 \text{ s (beginning of cycle)}$$

and

$$\tau_f = 6.5 \text{ s (end of cycle)} \quad (7)$$

The time constant at the end of a fuel cycle is higher due to the increase of thermal resistance with increasing fuel exposure.

In Secs. III.A and III.B, it is pointed out that the *effective* lumped fuel time constant is much smaller than the time constant derived in the above-mentioned manner.

III. EXPERIMENTAL RESULTS

In this section, extensive use has been made of reactor noise analysis techniques. The reader who is not familiar with these techniques is referred to the references given in this section.

III.A. Peaking of the Reactor Transfer Function

The reactivity-to-power reactor transfer function (RTF) depends on the fuel time constant. Using a

model for the dynamics of a BWR developed by Kleiss and van Dam,⁷ the RTF could be calculated for different fuel time constants (see Fig. 1). This model uses the transfer function between power variations and variations of the heat current as represented in Eq. (4).

An experimental estimation of the RTF was obtained in two ways: by analyzing the response of the neutron flux to control rod steps and by using the space-dependent noise characteristics as reflected in the coherence spectrum of the signals of ex-core neutron detectors.⁸ This latter method needs further explanation. The noise of the ex-core neutron detectors of the Dodewaard reactor is for frequencies below a few hertz, purely due to reactivity fluctuations.⁹ The coherence between the noise of several detectors is determined by their field of view. As this field of view depends on the RTF, this function can be determined by measuring the coherence between neutron noise signals.¹⁰ The resulting RTFs are presented for two vessel pressures in Fig. 2. A slight peaking of the RTF at ~ 1 Hz can be observed. From Fig. 1 it is clear that the position of this maximum of the transfer function calls for an *effective* fuel time constant of 1 to 2 s.

III.B. Transfer Function from Power to Pressure

The open-loop transfer function from power to pressure consists of two parts: One part relates power variations to variations in the steam production rate

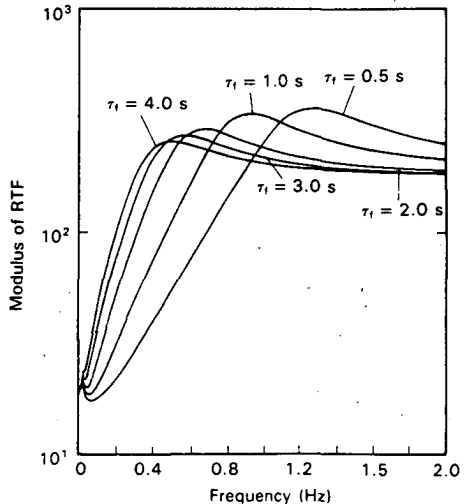


Fig. 1. Modulus of the RTF for different fuel time constants, calculated by a reactor dynamics model.

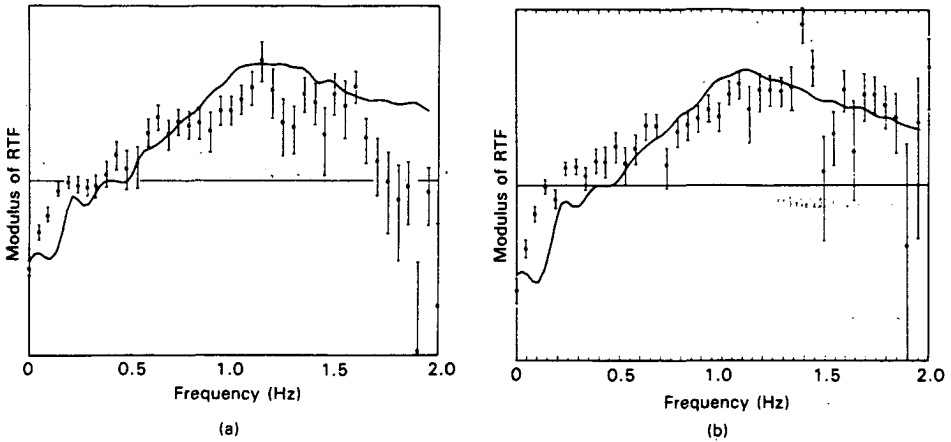


Fig. 2. Modulus of the RTF determined from control rod step response (dots with 2σ error bars) and from the space-dependent coherence of the ex-core neutron flux (curves) for two vessel pressures at (a) 70 bar and (b) 74 bar (logarithmic scale, arbitrary units).

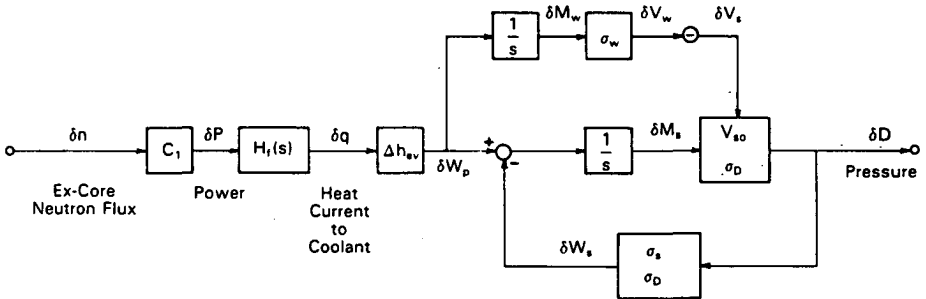


Fig. 3. Block diagram of the open-loop transfer function between variations of the ex-core neutron flux and pressure variations ($\sigma_D = d\sigma_s/dD$).

and a second part relates the latter variations to pressure variations; for the block diagram see Fig. 3 in which c_1 is a constant.

Using the lumped parameter model, the transfer function between power variations and variations of the heat current to the coolant is given by Eq. (4).

If the small time constant related to the evaporation process is neglected, variations of the steam mass production rate δW_p are related to variations of the heat current δq as

$$\delta W_p = \frac{\delta q}{\Delta h_{ev}}, \quad (8)$$

in which Δh_{ev} is the evaporation enthalpy of the water per mass unit, including the energy needed to heat the water from the feedwater temperature to the boiling temperature.

Because the pressure control is switched off during the experiments, the steam mass flow W_s from the vessel to the (vacuum) condenser is driven by the vessel

pressure D . As the pressure drop for turbulent flow is generally proportional to the density and the square of the velocity, we find

$$W_s \propto v_s \sigma_s \propto (\sigma_s D)^{1/2}, \quad (9)$$

in which

v_s = steam velocity

σ_s = steam density.

Thus, for variations of the steam flow

$$\frac{\delta W_s}{W_{s0}} = \frac{1}{2} \left(\frac{\delta \sigma_s}{\sigma_{s0}} + \frac{\delta D}{D_0} \right). \quad (10)$$

The subscript 0 refers to steady-state values.

The pressure in the vessel is related to the steam density as

$$\delta D = \frac{dD}{d\sigma_s} \delta \sigma_s, \quad (11)$$

where $dD/d\sigma_s$ represents the total differential from pressure to steam density at saturation temperature.

As the steam density is equal to the total mass M_s of the steam in the vessel divided by the volume V_s occupied by it,

$$\sigma_s = \frac{M_s}{V_s}. \quad (12)$$

Equation (11) can be written as

$$\delta D = \frac{dD}{d\sigma_s} \sigma_{s0} \left(\frac{\delta M_s}{M_{s0}} - \frac{\delta V_s}{V_{s0}} \right). \quad (13)$$

As in Ref. 7, we assume that the feedwater flow is constant; thus, variations of the steam volume arise from variations of the evaporation rate of the water. Denoting the water mass in the vessel by M_w and the (constant) water density by σ_w , variations of the water volume in the vessel V_w can be described by

$$\delta V_w = \frac{\delta M_w}{\sigma_w} = - \frac{\delta W_p}{s\sigma_w}. \quad (14)$$

For variations of the steam volume, as the total vessel volume is constant, we find

$$\delta V_s = -\delta V_w = \frac{\delta W_p}{s\sigma_w}. \quad (15)$$

Neglecting the mean residence time of the steam in the core compared with the residence time of the steam in the vessel (0.34 and 12 s, respectively⁷), variations of the steam mass in the vessel can be described by

$$s\delta M_s = \delta W_p - \delta W_s. \quad (16)$$

Substitution of Eqs. (8) and (10) in Eq. (16) gives

$$s\delta M_s = \frac{\delta q}{\Delta h_{ev}} - \frac{1}{2} W_{s0} \left(1 + \frac{D_0}{\sigma_{s0}} \frac{d\sigma_s}{dD} \right) \frac{\delta D}{D_0}. \quad (17)$$

Combining Eqs. (13), (15), and (17) gives

$$s\delta D = \frac{dD}{d\sigma_s} \frac{\sigma_{s0}}{V_{s0} \Delta h_{ev}} \left[\frac{1}{\sigma_{s0}} - \frac{1}{\sigma_w} \right] \delta q - \frac{1}{2} \frac{W_{s0}}{M_{s0}} \left(1 + \frac{\sigma_{s0}}{D_0} \frac{dD}{d\sigma_s} \right) \delta D, \quad (18)$$

from which the transfer function from heat current to vessel pressure can be derived.

The transfer function can be written as

$$\frac{\delta D}{\delta q} = \frac{\Gamma}{1 + s\tau_s}, \quad (19)$$

with

$$\Gamma = \frac{2D_0}{W_{s0} \Delta h_{ev}} \frac{1 - \sigma_{s0}/\sigma_w}{1 + \frac{d\sigma_s}{dD} \frac{D_0}{\sigma_{s0}}} \quad (20)$$

and

$$\tau_s = \frac{2M_{s0}}{W_{s0}} \frac{1}{1 + \frac{dD}{d\sigma_s} \frac{\sigma_{s0}}{D_0}} \quad (21)$$

being the mean residence time of the steam in the vessel.

For nominal conditions

$$\tau_s \approx 12 \text{ s}. \quad (22)$$

The combination of Eqs. (4) and (19) gives the transfer function from power to pressure:

$$H(s) = \frac{\delta D(s)}{\delta P(s)} = \frac{K}{(1 + s\tau_s)(1 + s\tau_f)}, \quad (23)$$

where K is the amplification factor.

Modeling the noise of the neutron flux and the pressure signals by an autoregressive (AR) technique,¹¹ the open-loop transfer function as presented in Fig. 4 is obtained. This function was fitted to the theoretical model [Eq. (23)] by the program FATAL, which uses a combination of Newton-Raphson, Steepest Descent, and Marquardt algorithms for minimizing a sum of squares.¹² This leads to the effective fuel time constant

$$\tau_f = 2.0 \pm 0.4 \text{ s}. \quad (24)$$

Although the fitting of a function of two exponentials is in general quite cumbersome (especially when the two time constants involved are of the same order of magnitude), the determined value of τ_f is very accurate as the value of τ_s is much larger. Another estimation, in fact based on the same derivation, can be obtained by using the response of the pressure to a power step.

Denoting the step response by $h(t)$, we obtain from Eq. (23)

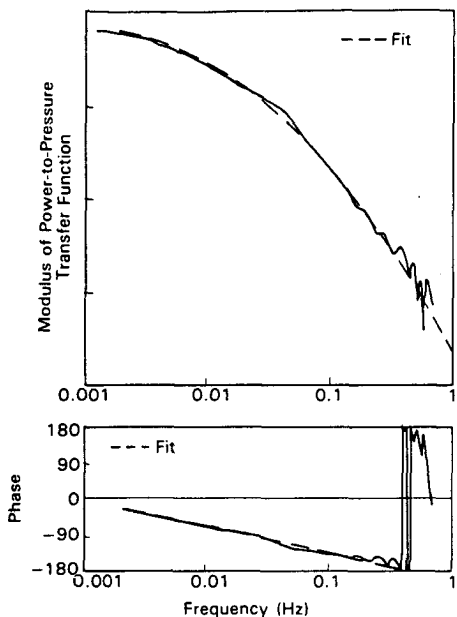


Fig. 4. Experimentally determined open-loop transfer function from power to pressure with its best fit.

$$h(t) = \frac{K}{\tau_s - \tau_f} [\tau_f \exp(-t/\tau_f) - \tau_s \exp(-t/\tau_s) + \tau_s - \tau_f] \quad (25)$$

Figure 5 gives the step response from the AR-modeled experimental data. Its fit, again calculated by FATAL (Ref. 12), is also shown. The resulting effective fuel time constant is

$$\tau_f = 2.11 \text{ s} \quad (\sigma = 3\%) \quad (26)$$

III.C. Fuel Elongation

The Dodewaard power plant is equipped with a device that measures the elongation of the cladding of a fuel rod relative to the elongation of the channel of the fuel assembly. Measurements of the elongation at the end of 1984 (cycle 15) on an assembly with a high burnup [31.2 MWd/kg (U + Pu)] show a significant response after a power increase. It is not only the increase of the cladding temperature that causes the elongation of the cladding. As the temperature of the UO₂ is changing more than that of the cladding and as the linear expansion coefficient of UO₂ is considerably larger than that of Zircaloy (10 and 6.3 × 10⁻⁶ °C⁻¹, respectively), the pellet/clad interaction forces the cladding to an additional expansion. Fig-

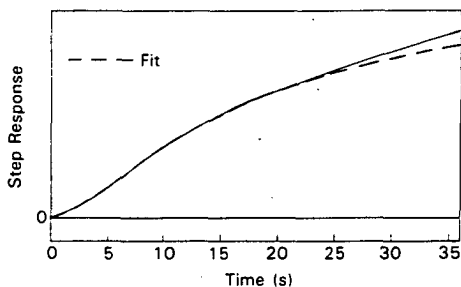


Fig. 5. Step response of pressure fluctuations to flux fluctuations determined by an AR model with its best fit (linear scale, arbitrary units).

ure 6 displays the response of the elongation meter to a control rod insertion. The response was averaged over 40 rod insertions. It is clear that a large part of the response is achieved within a few seconds after the rod movement. After 20 s the colder recirculation water reaches the core and compensates the reactivity disturbance by the control rod via the moderation effect.¹³ A second experiment was performed at the end of 1985 (cycle 16) on a low-burnup assembly [6.7 MWd/kg (U + Pu)]; the elongation meter showed no significant response in this case, probably due to the absence of pellet/clad interaction.

To extract the effective fuel time constant from the measured response, one needs to take into account several reactivity feedback loops, such as void, pressure, and Doppler feedback. Using the above-mentioned model of BWR dynamics developed by Kleiss and van Dam,⁷ the closed-loop transfer function from reactivity to fuel temperature was calculated for different fuel time constants (Fig. 7). It can be seen that the frequency of the maximum of this function strongly depends on the fuel time constant. Thus, a good opportunity for determining the fuel time constant is provided by calculating this transfer function from the measured response of the elongation meter to a control rod insertion. Unfortunately, this analysis was impeded due to the fact that the spectrum of the control rod movement hardly contains frequencies around 0.6 Hz (the frequency range of our interest). This is due to the fact that the control rods in the Dodewaard reactor can only be moved from one notch to another, with the velocity of the movement predetermined by the control rod drive mechanism. Another hindering factor is the unknown relation between variations of the fuel temperature and cladding length.

In conclusion, it can be stated that the experimental results, based on two independent methods of analysis, lead to a much smaller effective lumped fuel time constant than the one derived in Sec. II.

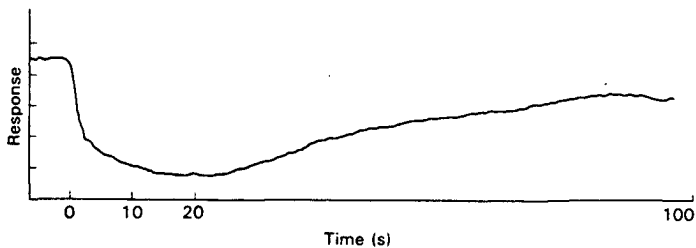


Fig. 6. Response of the fuel elongation meter to a control rod insertion (vertical scale divisions correspond to 9 μm).

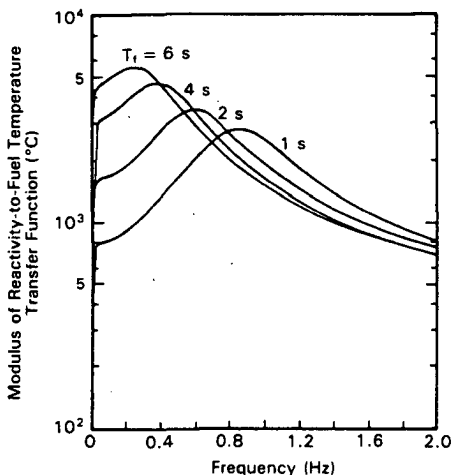


Fig. 7. Calculated closed-loop transfer function between reactivity variations and variations of the fuel temperature.

IV. NUMERICAL ANALYSIS

IV.A. Stationary Temperature Profile

Heat removal from the fuel is a complex transport process through four zones: the fuel, the gap between the fuel and the cladding, the cladding, and a boiling layer. Assuming rotational symmetry and neglecting axial effects, the heat transfer from fuel to coolant can be described by the differential equation¹⁴

$$\rho c_p \frac{\partial T}{\partial t} = \frac{1}{r} \frac{\partial}{\partial r} \left(rk \frac{\partial T}{\partial r} \right) + q''', \quad (27)$$

with

q''' = heat generation rate density ($\text{J}/\text{m}^3 \cdot \text{s}$)

k = thermal conductivity ($\text{J}/\text{m} \cdot \text{s} \cdot ^\circ\text{C}$).

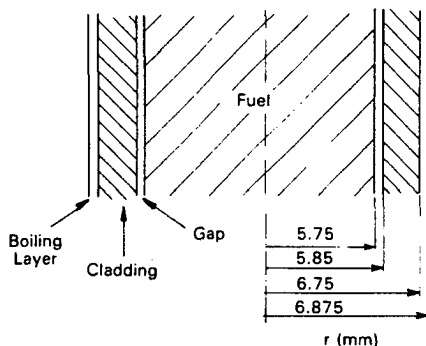


Fig. 8. Fuel pin geometry (not to scale).

Equation (27) was solved numerically for the Dodewaard geometry (Fig. 8) using the data presented in Table I (midcycle conditions). This equation is also valid for gap conductance, provided that an equivalent heat transfer coefficient is used.¹⁴

The resulting temperature profile under nominal conditions can be seen in Fig. 9. The average fuel temperature of 580°C corresponds to the design value; this validates the model and the data used. A realistic end-of-life situation that improves the heat transfer is the situation in which the gap is closed due to thermal expansion and swelling of the pellets. The average fuel temperature for this case is lower: 470°C.

IV.B. Dynamic Behavior

The dynamic behavior of the fuel pin can be studied by varying quantities or coefficients of Eq. (27) with time. For instance, the relaxation of the temperature after a change of the heat generation q''' can be observed. For the situation of an infinitely long unclad cylindrical fuel element, Eq. (27) can be solved analytically by separating the variables. If the coolant

TABLE I
Derivation and Values of the Input Data for the Numerical Model

Fuel: $q'' = 153 \times 10^6 \text{ J/m}^3 \cdot \text{s}$ (averaged over the entire fuel)
The thermal conductivity k and the specific heat c_p of the fuel are strongly dependent on the temperature T (Ref. 6):
$k = \frac{k_1}{k_2 + T} + k_3 \exp(k_4 T) \text{ (J/m} \cdot \text{s} \cdot ^\circ\text{C)}, \quad T \leq 1650^\circ\text{C},$
where
$T = \text{temperature (}^\circ\text{C)}$
$k_1 = 4040 \text{ J/m} \cdot \text{s}$
$k_2 = 464^\circ\text{C}$
$k_3 = 1.216 \times 10^{-2} \text{ J/m} \cdot \text{s} \cdot ^\circ\text{C}$
$k_4 = 1.867 \times 10^{-3} ^\circ\text{C}^{-1}$;
$c_p = \frac{C_1 \theta^2 \exp(\theta/T)}{T^2 [\exp(\theta/T) - 1]^2} + C_2 T + \frac{C_3}{RT^2} \exp\left(\frac{C_4}{RT}\right) \text{ (J/kg} \cdot ^\circ\text{C)},$
where
$T = \text{temperature (K)}$
$C_1 = 296.7 \text{ J/kg} \cdot ^\circ\text{C}$
$C_2 = 2.43 \times 10^{-2} \text{ J/kg} \cdot ^\circ\text{C}^2$
$C_3 = 1.379 \times 10^{13} \text{ J}^2/\text{kg} \cdot \text{mol}$
$C_4 = 1.577 \times 10^5 \text{ J/mol}$
$\theta = \text{Einstein temperature} = 535.285 \text{ K}$
$R = \text{gas constant} = 8.3143 \text{ J/}^\circ\text{C} \cdot \text{mol}$;
$\rho = 10.0 \text{ kg/m}^3$ (95% thermal density)
Gap: $q'' = 0$
Using an equivalent heat transfer coefficient based on conduction and radiation $\alpha = 4 \times 10^3 \text{ J/m}^2 \cdot \text{s} \cdot ^\circ\text{C}$ (Ref. 4) and a gap thickness d_g of 0.1 mm, an equivalent thermal conductivity can be defined ¹⁴ as
$k = \alpha d_g = 4 \times 10^3 \times 1 \times 10^{-4} = 0.4 \text{ J/m} \cdot \text{s} \cdot ^\circ\text{C};$
$\rho c_p = 0$
Cladding: $q'' = 0$
$k = k_0 + k_1 T + k_2 T^2 + k_3 T^3 \text{ (J/m} \cdot \text{s} \cdot ^\circ\text{C)} \text{ (Ref. 6)},$
where
$T = \text{temperature (K)}$
$k_0 = 7.51 \text{ J/m} \cdot \text{s} \cdot ^\circ\text{C}$
$k_1 = 2.09 \times 10^{-2} \text{ J/m} \cdot \text{s} \cdot ^\circ\text{C}^2$
$k_2 = -1.45 \times 10^{-3} \text{ J/m} \cdot \text{s} \cdot ^\circ\text{C}^3$
$k_3 = 7.67 \times 10^{-9} \text{ J/m} \cdot \text{s} \cdot ^\circ\text{C}^4$
for $T = 560 \text{ K}$: $k = 16 \text{ J/m} \cdot \text{s} \cdot ^\circ\text{C}$;
$c_p = 280 \text{ J/kg} \cdot ^\circ\text{C}$ (Ref. 15);
$\rho = 6.51 \text{ kg/m}^3$ (Ref. 15)

(Continued)

TABLE I (Continued)

Boiling Layer: $q'' = 0$	
The equivalent thermal conductivity k is defined as the heat transfer coefficient α times the thickness d_b of the boiling layer. The heat transfer coefficient is composed of the heat transfer coefficients of the oxide zone on the Zircaloy α_o , the crud layer α_c , and the boiling film α_f :	
$\alpha_b = \frac{1}{\frac{1}{\alpha_o} + \frac{1}{\alpha_c} + \frac{1}{\alpha_f}} = 1.40 \times 10^4 \text{ J/m}^2 \cdot \text{s} \cdot ^\circ\text{C} \quad (\text{Ref. 4})$	
$(\alpha_f \text{ was determined using the Jens-Lottes' correlation}^{14}).$	
The thickness of the boiling layer was taken one mesh width = 0.125 mm. The actual value does not greatly influence the results.	
$k = \alpha_b d_b = 1.40 \times 10^4 \times 1.25 \times 10^{-4} = 1.75 \text{ J/m} \cdot \text{s} \cdot ^\circ\text{C}$	
The specific heat capacity and the density of the two-phase mixture are calculated using an averaged void fraction of 30%.	
$c_p = [\alpha \rho_{\text{steam}} c_{p,\text{steam}} + (1 - \alpha) \rho_{\text{water}} c_{p,\text{water}}] / \rho$ $= 5.5 \times 10^3 \text{ J/kg} \cdot ^\circ\text{C} ;$ $\rho = \alpha \rho_{\text{steam}} + (1 - \alpha) \rho_{\text{water}} = 524 \text{ kg/m}^3$	

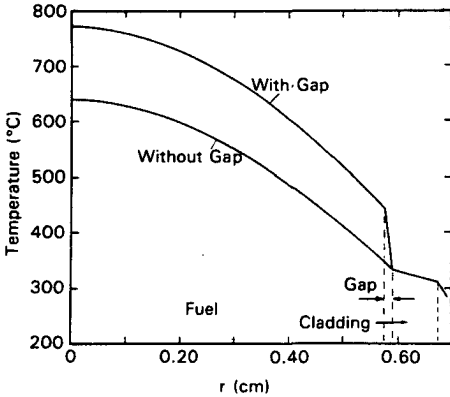


Fig. 9. Radial temperature profile of a fuel pin.

temperature T_c is constant and using the boundary condition

$$-k \frac{dT}{dr} \Big|_{r=R} = \alpha(T - T_c) \quad (28)$$

and the initial condition $T(r, t = 0) = T_c$, then the normalized fuel temperature after a sudden start of heat generation q'' is³

$$T'(r', t') = \sum_{n=1}^{\infty} \frac{2\text{Bi}}{\lambda_n^2(\lambda_n^2 + \text{Bi}^2)} \cdot \frac{J_0(\lambda_n r')}{J_0(\lambda_n)} \times [1 - \exp(-\lambda_n^2 t')] \quad (29)$$

in which

T' = dimensionless fuel temperature = $(T - T_c) \times (k/R^2 q'')$

r' = normalized radius = r/R

t' = dimensionless time = $t(k/\rho_f c_f R^2)$

Bi = Biot number = $\alpha R/k$

λ_n = n 'th root of $\text{Bi} = \lambda_n [J_1(\lambda_n)/J_0(\lambda_n)]$

J_0 = Bessel function of the zero order, first kind

J_1 = Bessel function of the first order, first kind

R = radius of the fuel pellet.

Thus, the response function contains a spectrum of fuel time constants instead of the single value from the lumped parameter technique.

Using core-averaged plant data⁴ and literature values^{5,6} for α , k , c_f , and ρ_f (resulting in $\text{Bi} = 2.5$), the following time constants for the Dodeward fuel are obtained³:

$$\tau_n = \frac{1}{\lambda_n^2} = 8.3, 1.3, 0.44, 0.22, 0.13, \dots \text{ s} \quad (30)$$

The case of the pellet with a cladding (with or without gap) is much more complex and does not allow an analytical solution. The time constants related

to the transfer function between power and heat current can be determined by calculating the relaxation of the linear heat flux (that is, the heat flux per unit of length) from the cladding to the boiling layer after, for instance, a 5% power decrease from nominal conditions using a computer code. The response for the case with an open gap is presented in Fig. 10. Treating the fuel pellet as a first-order system, like using the lumped parameter method, a graphical fit of the slope of the linear heat flux response corresponds with a time constant

$$\tau_f = 6.0 \pm 0.5 \text{ s} \quad (31)$$

This agrees with the result of the lumped parameter model [Eq. (7)].

The calculated step response can be described in a similar way as Eq. (29), which was a result of the response for the unclad situation

$$\phi(t) = \sum_i A_i [1 - \exp(-t/\tau_i)] \quad (32)$$

in which $\phi(t)$ denotes the linear heat flux from cladding to coolant.

A more accurate value of the spectrum of time constants can be obtained by differentiating the step response, that is, to examine the impulse response (see Fig. 11). From Eq. (33) it can be seen that small time constants will gain importance in this case:

$$\frac{d\phi(t)}{dt} = \sum_i \frac{A_i}{\tau_i} \exp(-t/\tau_i) \quad (33)$$

After fitting the impulse response to a second-order model, the time constants presented in Table II

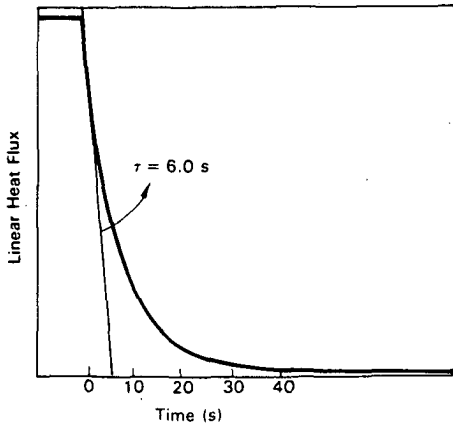


Fig. 10. Response of the linear heat flux from cladding to boiling layer after a 5% stepwise power decrease.

were derived. The case in which the gap between the fuel and the cladding is closed is also examined (Table II).

A comparison with the results of Sec. II leads to the conclusion that the two time constants model exhibits a component with a considerably smaller time constant than the lumped time constant from Sec. II [Eq. (7)]. Gap closure even decreases this value. This results in a small effective lumped fuel time constant and corresponds with the experimental results of Secs. III.A and III.B.

The response of the heat flux from the fuel to the cladding was decomposed in a three time constants model in order to compare the resulting time constants with the values derived by Iriarte.¹ From his graphs three time constants for the heat transfer from bare fuel to the coolant under Dodewaard conditions were derived. They are presented in Table III together with the time constants from our numerical model. The values correspond remarkably well.

It should be stressed here that the thermohydraulic properties of the materials depend strongly on the

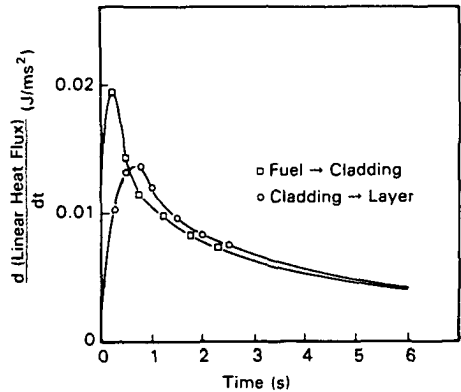


Fig. 11. Time derivative of the linear heat flux after a 5% stepwise power decrease.

TABLE II

Fuel Time Constants Determined from the Impulse Response of the Linear Heat Flux from Cladding to Boiling Layer

	Fuel Time Constants (s)	
	Gap	1.0
No gap	0.77	5.4

TABLE III
Comparison of Fuel Time Constants from the Numerical Model and from Iriarte¹

	Fuel Time Constants (s)		
Numerical model	0.77	1.1	7.9
Iriarte	0.4 ± 0.3	1.3 ± 0.2	7 ± 1

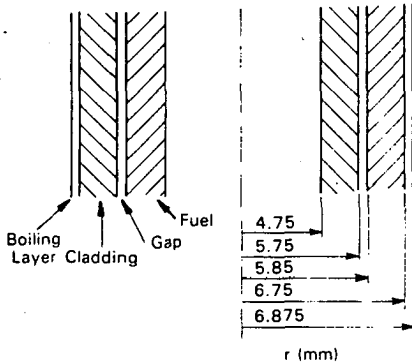


Fig. 12. Geometry for a ring-type fuel (not to scale).

burnup: The coefficient for thermal conductivity of UO_2 decreases 60% after 4 MWd/kg at 91°C (Ref. 3). No dependence of the other parameters on burnup was found in the literature.

The effective lumped fuel time constant depends on the frequencies involved. Heat transfer for high frequencies is governed by small fuel time constants that stem from the outer region of the fuel. As an example, the effective lumped fuel time constant of a ring-type fuel pellet (geometry as in Fig. 12) was calculated. The numerical model leads to a time constant of 1.18 s, whereas a description by a first-order model gives 1.17 s.

V. CONCLUDING REMARKS

It is clear from experimental and theoretical analyses that the heat transfer from fuel to coolant contains components with a small time constant that allow high frequencies in the reactivity feedback. The outer ring of the fuel reacts quickly to power variations, whereas the bulk follows slow variations.

Theoretical analyses have determined that the spectrum of time constants related to the heat transfer from an unclad pellet contains infinitely small components.

Experiments performed in the Dodewaard BWR have resulted in an effective fuel time constant as short as 2 s.

REFERENCES

1. M. IRIARTE, Jr., "An Accurate Transfer Function for the Dynamic Analysis of Temperature and Heat Release in Cylindrical Fuel Elements," *Nucl. Sci. Eng.*, 7, 26 (1960).
2. E. B. J. KLEISS, "On the Determination of Boiling Water Reactor Characteristics by Noise Analysis," Thesis, Delftse Universitaire Pers, Delft (1983).
3. M. M. EL-WAKIL, *Nuclear Heat Transport*, pp. 104, 200-203, and 221-228, American Nuclear Society, La Grange Park, Illinois (1978).
4. J. HOEKSTRA, Private Communication (1983).
5. W. R. van ENGEN and W. H. M. NISSEN, "Elongation Measurements on Fuel Assemblies During Irradiation in the Dodewaard Boiling Water Reactor," *Proc. Enlarged Halden Program Group Mtg. Water Reactor Fuel Performance*, Hankö, Norway, June 15-19, 1981, HPR-286, No. 4, Institutt for Energiteknikk, OECD Halden Reactor Project.
6. H. FENECH, *Heat Transfer and Fluid Flow in Nuclear Systems*, p. 15, Pergamon Press, New York (1981).
7. E. B. J. KLEISS and H. van DAM, "A Simplified Model for the Dynamics of a BWR," *Ann. Nucl. Energy*, 12, 5, 233 (1983).
8. T. H. J. J. van der HAGEN, H. van DAM, J. E. HOOGENBOOM, E. B. J. KLEISS, W. H. M. NISSEN, and W. J. OOSTERKAMP, "Analysis of Natural Circulation BWR Dynamics with Stochastic and Deterministic Methods," *Proc. 6th Power Plant Dynamics, Control and Testing Symp.*, April 14-16, 1986, p. 48.01, The University of Tennessee, Department of Nuclear Engineering (1986).
9. J. H. C. van der VEER, "Noise Analysis of the Dodewaard Boiling Water Reactor: Characteristics and Time History," *Progr. Nucl. Energy*, 9, 607 (1982).
10. E. B. J. KLEISS and H. van DAM, "Incore Power Feedback Effects Deduced from Neutron Noise Measurements," *Ann. Nucl. Energy*, 8, 205 (1981).
11. B. R. UPADHYAYA, M. KITAMURA, and T. W. KERLIN, "Multivariate Signal Analysis Algorithms for Process Monitoring and Parameter Estimation in Nuclear Reactors," *Ann. Nucl. Energy*, 7, 1 (1980).

12. L. SALMON and D. V. BOOKER, "FATAL—A General Purpose Computer Program for Fitting Experimental Data to Any Required Function," Health Physics and Medical Division, U.K. Atomic Energy Authority Research Group, Atomic Energy Research Establishment, Harwell (1972).

13. T. H. J. J. van der HAGEN, W. H. M. NISSEN, W. J. OOSTERKAMP, H. van DAM, and J. E. HOOGENBOOM, "Application of Noise Analyses to Stability Deter-

mination of a Natural Circulation Cooled BWR," *Progr. Nucl. Energy*, **21**, 753 (1988).

14. R. T. LAHEY, Jr. and F. J. MOODY, *The Thermal-Hydraulics of a Boiling Water Nuclear Reactor*, pp. 147, 254, and 266, American Nuclear Society, La Grange Park, Illinois (1977).

15. *Handbook of Chemistry and Physics*, 60th ed., pp. B-26 and D-182, CRC Press, Boca Raton, Florida (1979).

Chapter 8

Application of noise analyses to stability determination of a natural-circulation-cooled BWR

T.H.J.J. van der Hagen², W.H.M. Nissen³,
W.J. Oosterkamp⁴, H. van Dam² & J.E. Hoogenboom²

Abstract

Experiments were performed on the Dodewaard natural-circulation-cooled BWR under different conditions. Absolute stability was determined by measuring the system responses to control-rod and steam-flow valve steps. Changes in core stability were studied using the signal of an average power range monitor (APRM) in the time domain (auto-correlation function and impulse response) and in the frequency domain (power spectral density and rms ratio), and the outlet void fraction and variations of the in-core coolant velocity.

It is shown that the reactor is very stable and that cooling by natural circulation improves load following. Stability monitoring can be performed by all mentioned methods, but using APRM signals in the frequency domain is preferred.

-
- ¹ This chapter is a slightly adapted version of a contribution published in *Progress in Nuclear Energy* 21: 753-761 (1988). It reviews the analysis of system responses to control-rod steps and vessel pressure changes which was mentioned in Chapter 6. It is included here as it deals in detail with stability monitoring using the noise signals of ex-vessel neutron detectors.
 - ² Interfaculty Reactor Institute, Delft University of Technology, Mekelweg 15, 2629 JB DELFT, The Netherlands.
 - ³ N.V. Gemeenschappelijke Kernenergiecentrale Nederland, P.O. Box 9035, 6800 ET ARNHEM, The Netherlands.
 - ⁴ N.V. KEMA, P.O. Box 9035, 6800 ET ARNHEM, The Netherlands.

Introduction

Stability monitoring of a BWR is of great interest for safety aspects and for an efficient use of the reactor. Therefore the Dodewaard nuclear power plant has been subject to experiments concerning stability determination. An important feature of the Dodewaard BWR is that it is cooled by natural circulation.

Earlier measurements have shown some striking results regarding the stability of the reactor (Van der Hagen et al., 1986). By determining the reactivity-to-power transfer function (RTF), it was shown that the reactor-kinetic stability, which has its origin in the reactivity feedback via the void fraction, is not significantly influenced by pressure changes. The neutron noise spectrum of an average power range monitor (APRM), however, did show some variation. This is due to variations of the input reactivity noise, which reflects thermal-hydraulic stability. Upadhyaya et al. (1982) have shown that the neutron noise spectrum gives indeed information about changes in core stability. However, a perturbation test is needed for absolute measurement of the stability.

This study deals with application of methods and criteria that might be considered for monitoring stability during operation. Several ways of getting information on stability from the neutron noise signal are in use:

- (1) in the time domain:
 - calculation of the auto-correlation function (March-Leuba & King, 1987);
 - calculation of the impulse response, using an autoregressive model (Upadhyaya et al., 1982).

The decay ratio, defined as the ratio between two consecutive maxima, can be obtained from these functions.

- (2) in the frequency domain:
 - fitting of the normalised auto-power spectral density (NAPSD). Most authors use a second-order model (a.o. Gialdi et al., 1985; Federico & Ragona, 1986). March-Leuba (1986) proposes a functional form with three zeros and four poles as a model for the RTF; this indicates that a higher-order model might be more successful;
 - calculation of the root mean square (rms) value over a certain frequency interval.

Changes of the spectrum that are linked with changes in stability can be observed on the basis of these findings.

Other possible stability criteria are the outlet void fraction of the hottest channel (presently in use for the Dodewaard BWR) and the standard deviation of the in-core coolant velocity.

Experiments were performed on the Dodewaard nuclear power plant in order to examine the validity of the above-mentioned criteria. The absolute stability of the reactor was observed by measuring system responses to control-rod and steam-flow control-valve steps.

Table 11
Experimental conditions.

experiment	power (MWth)	pressure (MPa)	cycle
1	164	7.4	EOC 15
2	161	6.95	EOC 15
3	173.5	7.55	EOC 16
4	172	7.05	EOC 16
5	170.5	7.6	EOC 16
6	170.5	7.0	EOC 16

Experimental conditions

Stability measurements were performed under six different experimental conditions, all at maximum power and nominal or lowered pressure. Table 11 lists the relevant process parameters.

The pressure control was switched off during all the experiments. For experiments 5 and 6, the normal neutron-flux profile was distorted by withdrawing the central control rods (all other rods were already withdrawn as the reactor was at the end of its cycle). A radial peaking factor as high as 1.82 was thus created at the centre of the core (normal value = 1.6). The central channel was therefore considerably less stable than under normal reactor conditions. The stability margin was even further reduced by lowering the reactor pressure in experiment 6.

Noise recordings of relevant signals at stationary conditions were performed during all experiments. During experiments 1-4, the responses of the system to control-rod steps and to steam-flow control-valve steps were also recorded.

Stability evaluations

This section deals with two topics: absolute stability and monitoring of the changes in stability.

Absolute stability – An indication of the absolute stability of the reactor was obtained by measuring the signal responses to control-rod and steam-flow control-valve steps. A control-rod step causes a local reactivity disturbance and thus enables the observation of the reactor-kinetic stability. In order to obtain a maximum reactivity effect, the central control rod was selected and was moved periodically between two positions in the core around the neutron-flux maximum. The movement had an amplitude of four centimetres; its period was four minutes during experiments 1 and 2 and eight minutes during experiments 3 and 4. A detailed description of the evaluation of rod and valve step responses during experiments 1 and 2 is given by Van der Hagen et al. (1986).

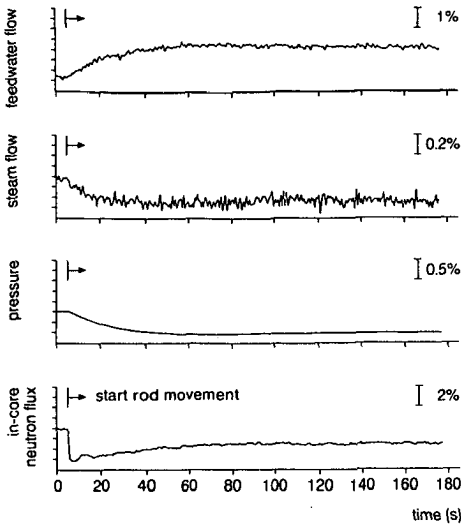


Fig. 56
Signal responses to control-rod insertion at experiment 4. Vertical scale-division values are shown.

Figure 56 displays the responses of the most relevant signals to control-rod insertion in the least stable situation at which step responses were determined, that is highest power and lowest pressure: experiment 4. The responses were averaged over twenty insertions in order to reduce the noise level. It is clear from this figure that good reactor-kinetic stability is assured.

The steam-flow control-valve steps excite the core as a whole via the pressure-reactivity effect. The total-plant stability can therefore be observed from the responses to these steps. Figure 57 gives the main averaged responses to a valve opening during experiment 4. The first 20-30 seconds correspond with a positive pressure-reactivity coefficient, as

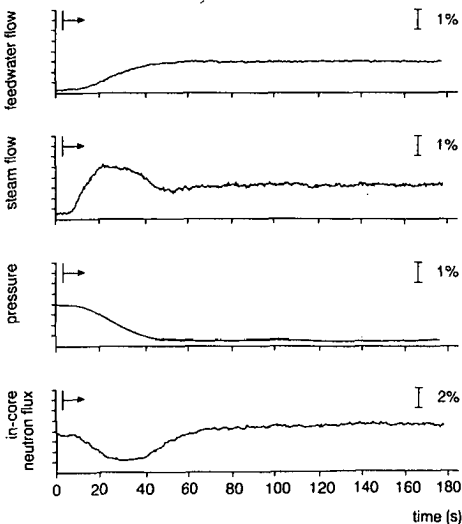


Fig. 57
Signal responses to valve opening at experiment 4. Vertical scale-division values are shown.

expected: a decrease in pressure leads to a higher void fraction which in turn leads to moderation and thus a power decrease. The neutron flux then increases to a level even higher than its initial value. This surprising effect that arises from cooling by natural circulation improves load following.

The increase in power is due to the colder recirculation water that reaches the core and increases reactivity in two ways: it reduces the void fraction and its density is higher. The time lag of this cold recirculation water can be calculated using the coolant volumes reported in Table 12.

For nominal conditions, the steam density is $35.6 \text{ kg}\cdot\text{m}^{-3}$ and the water density $740 \text{ kg}\cdot\text{m}^{-3}$ (Kleiss & Van Dam, 1985). The averaged void fraction is 0.3 in the core and 0.5 in the chimney. The resulting coolant weights are also presented in Table 12. Assuming a recirculation flow of $1400 \text{ kg}\cdot\text{s}^{-1}$ one obtains a time lag of $26000/1400 \text{ s} = 19 \text{ s}$. The time lag measured is larger; this is due to the fact that the recirculation flow through the bypass is very low and has a significant effect on core reactivity.

Table 12
Volumes and weight of the coolant in the reactor vessel.

	volumes (m^3)	coolant weight (kg)
reactor core (channels)	1.96	1040
bypass	2.37	1750
chimney	7.87	3060
downcomer above sparger	2.73	2020
downcomer below sparger	12.50	9230
lower plenum	12.00	8880
total	39.40	26000

The response of the steam velocity in the core was measured using a twin self-powered thermal-neutron detector. It was found that the velocity increases twenty seconds after a valve opening (Van der Hagen et al., 1986). A thermal-hydraulic analysis will be performed in order to understand this velocity effect.

In conclusion it can be stated that the Dodewaard reactor, due to natural circulation, is more self-regulating than BWRs cooled by forced circulation. The above mentioned findings indicate good stability under experimental conditions 1-4.

Monitoring changes in stability – The methods mentioned previously for determining changes of the core stability will now be presented for the different experimental conditions. The methods in the time domain will be considered first.

Figure 58 shows the normalised auto-correlation function of the signal of an APRM for two experimental conditions: experiment 1 (considered to be the most stable of the situations investigated) and experiment 6 (the least stable one). The functions show a damped oscillatory behaviour with a frequency of approximately 1.1 Hz. The best damping can be observed for experiment 1, as expected. However, the functions show a behaviour other than was observed by others (a.o. Fry et al., 1984; March-Leuba, 1984, 1987): in the present case the decay ratio can clearly not be found by simply calculating the quotient of two consecutive maxima. It can be concluded that the auto-correlation function reflects stability but that its use for stability monitoring is limited.

The impulse response of the APRM signal can be estimated from the AR model by using an initial value response of the form

$$h_i = \sum_{k=1}^p A_k h_{i-k} \quad (\text{Eq. 96})$$

with initial conditions either (Fry et al., 1984; March-Leuba, 1984)

$$h_0 = 1 \quad (\text{Eq. 97a})$$

$$h_{-k} = 0 \quad (\text{Eq. 97b})$$

or (Upadhyaya & Kitamura, 1981)

$$h_1 = 1 \quad (\text{Eq. 98a})$$

$$h_0, h_{-k} = 0 \quad (\text{Eq. 98b})$$

where h_i is the impulse response, p is the AR model order and A_k indicates the AR parameters.

The actual derived impulse response depends strongly on the initial values chosen as the response at $t=0$ is forced to be either 1 or 0. The choice depends on the system in question; using the conditions from

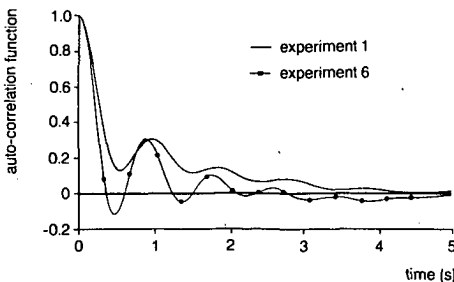


Fig. 58
Auto-correlation function of the signal of an APRM for experiment 1 (most stable situation investigated) and experiment 6 (least stable situation).

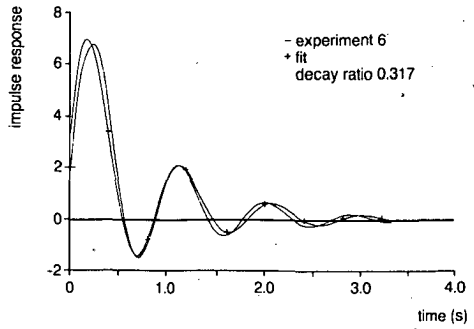
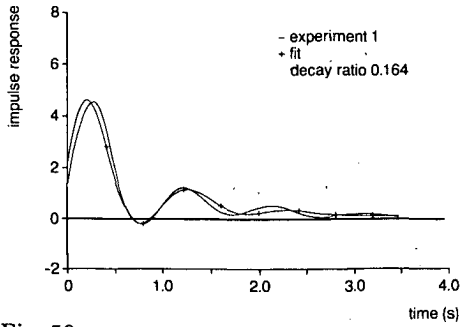


Fig. 59

Impulse response using initial conditions from Equation (97) derived by AR modelling of the APRM signal. The third-order fits are also shown (+).

Equation (97) lacks physical reality at $t=0$, as it implies an instantaneous response.

Figure 59 gives the impulse responses for experiments 1 and 6 following Fry et al. (1984) and March-Leuba (1984). The initial values mentioned by Upadhyaya & Kitamura (1981) were used for Figure 60. It is clear that the system under consideration is not of the second-order type as the oscillatory behaviour is superimposed on an exponential decay. This leads to an at least third-order system.

The first 3.5 seconds of the impulse responses using the conditions from Equation (97) were fitted to the third-order model

$$h(t) = A \exp(-\xi 2\pi f_0 t) \cdot \sin(2\pi f_0 \sqrt{1-\xi^2} t) + B \exp(-t/\tau) \quad (\text{Eq. 99})$$

(where t is time, ξ is the damping constant, f_0 is the characteristic frequency and τ is a time constant) by using the programme FATAL, which uses a combination of Newton-Raphson, Steepest Descent and Marquardt algorithms for minimizing a sum of squares (Salmon & Booker, 1972). It can be seen from Figure 59 that the impulse response corresponding with the least stable situation is fitted best; a similar result was mentioned by Fry et al. (1984), who performed second-order fits.

The decay ratio (DR) can be calculated from the model according to:

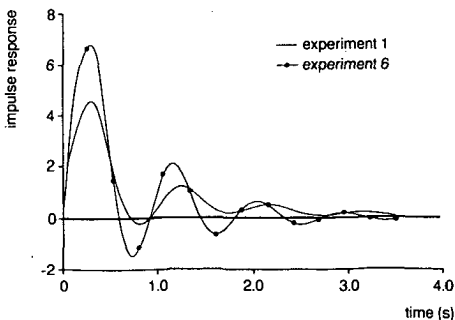


Fig. 60

Impulse response using initial conditions from Equation (98) derived by AR modelling of the APRM signal.

Table 13

Decay ratios and resonance frequencies obtained by fitting the impulse response and the NAPSD.

experiment	power (MWth)	pressure (MPa)	impulse response		NAPSD	
			DR	f _R	DR	f _R
1	164	7.4	0.164	0.92	0.170	1.01
2	161	6.95	0.233	0.97	0.205	1.05
3	173.5	7.55	0.197	0.96	0.213	1.09
4	172	7.05	0.257	1.00	0.261	1.13
5	170.5	7.6	0.238	1.03	0.229	1.14
6	170.5	7.0	0.317	1.06	0.306	1.14

$$DR = \exp(-2\pi\xi/\sqrt{1-\xi^2}) \quad (\text{Eq. 100})$$

The resulting decay ratios and resonance frequencies $f_R = f_0\sqrt{1-\xi^2}$, are reported in Table 13.

It can be seen from this table that a decrease in pressure leads to a higher decay ratio (worse stability) as does a higher power. The power distribution also contributes as can be seen from the decay ratios for experiments 5 and 6 where the strong flux peaking leads to a high value.

In spite of the good final results, an on-line determination of the core stability using the former-mentioned method is strongly impeded by the computer work involved: data acquisition, spectrum determination, AR modelling, calculation of the impulse response, fit of the impulse response, calculation of the decay ratio. An additional problem is the fact that only the asymptotic decay ratio reflects core stability (March-Leuba, 1984). This ratio can differ considerably from the apparent decay ratio.

The second part to be dealt with is the stability determination using the APRM signal in the frequency domain. Changes in stability influence the NAPSD in the frequency range around the break-frequency of the global neutron-noise component (Upadhyaya & Kitamura, 1981). For the Dodewaard reactor, this break-frequency is 1.1 Hz (Van der Veer, 1981). The spectrum was therefore fitted from 0.65-2.0 Hz, using the inverse variance of the NAPSD, given by

$$\sigma^{-2} = N/\text{NAPSD}(f) \quad (\text{Eq. 101})$$

(σ^2 denotes the variance and N the number of records used) as a weighting factor. The model used corresponds with the model used for fitting the impulse response

$$\text{NAPSD}(f) = \left| \frac{A'}{1 - \frac{f^2}{f_0^2} + 2j\xi\frac{f}{f_0}} + \frac{B'}{1 + j2\pi f\tau} \right|^2 \quad (\text{Eq. 102})$$

Figure 61 presents the NAPSD and its fit for experiments 1 and 6.

The decay ratio can be computed from the fits, using Equation (100). The result is found in Table 13. The decay ratios determined correspond well with those derived from the impulse response; the resonance frequency is, however, invariably higher. This is due to the fact that the oscillation frequency from the impulse response increases with time (Fig. 59). This points to a higher model order; the present model, however, is suitable for our purposes.

The rms value of the APRM signal is formed by the noise-source strength multiplied by the reactivity-to-power transfer function (both frequency-dependent), integrated over a certain frequency interval. As this value is easy to compute, one obviously tries to extract information on the core stability from it. Figure 61 shows clearly that the rms value (regardless of the frequency range) cannot be representative for the core stability; it is the relative height of the 1.1-Hz peak that reflects stability. This peaking of the spectrum can be expressed as the quotient of the rms value from 0.8-1.3 Hz and 0.4-0.8 Hz. These frequency ranges are chosen somewhat arbitrarily; the rms value from the first interval is taken to be influenced by stability changes, whereas that from the latter interval serves as a normalisation value. Figure 62 displays this quotient - the rms ratio - as a function of the decay ratio derived by spectrum fitting. It can be seen that the relation is remarkably linear for the experimental conditions investigated. Thus, the rms ratio is a convenient stability criterion for such situations.

Note: the signal of an in-core neutron detector was also investigated by the methods described above. Due to its large field-of-view around 1.1

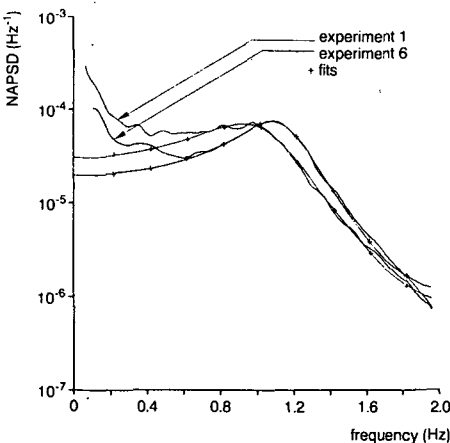


Fig. 61
The NAPSD of the APRM signal and a third-order fit for the two extreme situations.

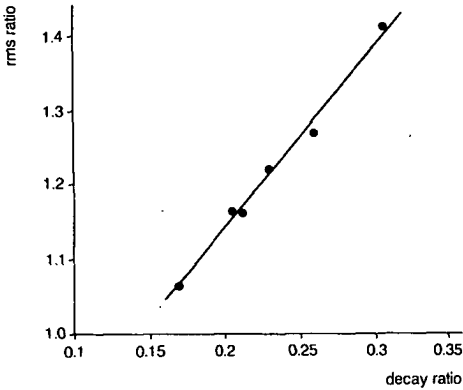


Fig. 62

The rms ratio (the ratio of the rms value of the APRM signal of 0.8-1.3 and 0.4-0.8 Hz) as a function of the decay ratio derived by spectrum fitting.

Hz (Kleiss, 1983), the results were identical to those obtained by using APRM signals.

Three criteria regarding safety aspects are in current use for the Dodewaard reactor:

- (1) the outlet void fraction of the hottest channel < 70%,
- (2) the maximum heat flux < $136 \text{ W}\cdot\text{cm}^{-2}$,
- (3) the ratio of the minimum heat flux for film-boiling and the actual heat flux > 1.5.

These criteria hold for 15% overpower.

In practice, only the first criterion limits operating power. The outlet void fraction cannot be measured but is calculated by the process computer of the power plant. A plot of this fraction as a function of the decay ratio derived by spectrum fitting shows that the relation is linear (Fig. 63) and can thus be used as a stability criterion. However, an upper limit of 70% seems conservative for the system responses evaluated earlier. Moreover, it is clear that the outlet void fraction criterion does not account for changes of the axial void-fraction profile that can influence core stability. The total void fraction of the hottest channel is that more likely to be reliable.

As thermal-hydraulic instability is characterised by large fluctuations of the coolant flow (especially in BWRs cooled by natural circu-

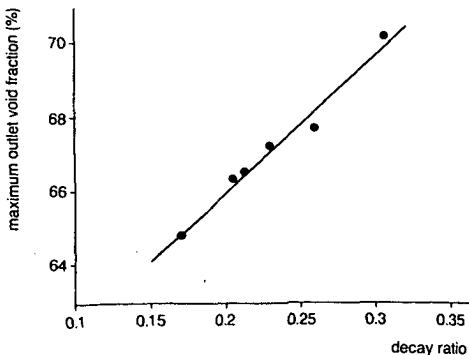


Fig. 63

The maximum outlet void fraction as a function of the decay ratio derived by spectrum fitting.

lation), variations of the in-core coolant velocity were measured by correlating the noise of two axially displaced in-core neutron detectors (see Kleiss & Van Dam, 1981a). It was found possible to estimate the steam velocity with a standard deviation of 3.0% within 1.3 s (Van der Hagen & Hoogenboom, 1988). The standard deviation of the estimated velocity was 3.3% for experiment 3 and 4.0% for experiment 4. Thus almost no significant velocity variations were found, which points to a stable reactor. The standard deviation was somewhat greater for experiment 4 than for experiment 3, corresponding with the lower stability.

It is clear that this method - under the conditions now investigated - is not sensitive enough to monitor core stability. An advantage in less stable situations is that it is the only method which allows separate channel-flow stability to be observed.

Concluding remarks

System responses to control-rod and steam-flow valve steps indicate a good core and total-plant stability. Cooling by natural circulation improves load following.

The variations in coolant velocity are too small to serve as a criterion for stability monitoring. Determining stability changes by calculation of the outlet void fraction of the hottest channel corresponds with the results of monitoring by using APRM signals, but it is felt that the first method is not always reliable and that the maximum allowable fraction of 70% (presently in use for the Dodewaard BWR) is conservative. The use of APRM signals in this reactor is complicated by the fact that the system cannot be described by a second-order model, as is usually done. Results obtained with a third-order model are in close agreement. Use of the rms ratio (the ratio between the rms value of 0.8-1.3 and 0.4-0.8 Hz) is a convenient and reliable method for the conditions now investigated.

References

- Federico, A.G. & R. Ragona 1986 Presentation at the 19th Informal Meeting on Reactor Noise (Rome, 4-6 June 1986).
- Fry, D.N., J. March-Leuba & F.J. Sweeney 1984 Use of neutron noise for diagnosis of in-vessel anomalies in light-water reactors - United States Nuclear Regulatory Commission (USNRC, Washington) Report NU-REG/CR-3303; Oak Ridge National Laboratory (Oak Ridge, Tennessee) Report ORNL/TM-8774; University of Tennessee (Knoxville): 88 pp.
- Gibaldi, E., S. Grifoni, C. Parmeggiani & C. Tricoli 1985 Core stability in operating BWR: operational experience - Progress in Nuclear Energy 15: 447-459.

- Kleiss, E.B.J. 1983 On the determination of boiling water reactor characteristics by noise analysis – Ph.D. thesis Delft University of Technology; Delftse Universitaire Pers: 147 pp.
- Kleiss, E.B.J. & H. van Dam 1981a A twin self-powered neutron detector for steam velocity determination in a boiling water reactor – Nuclear Technology 53: 250-256.
- Kleiss, E.B.J. & H. van Dam 1985 A simplified model for the dynamics of a BWR – Annals of Nuclear Energy 12: 233-245.
- March-Leuba, J. 1984 Dynamic behaviour of boiling water reactors – Ph.D. thesis University of Tennessee (Knoxville): 277 pp.
- March-Leuba, J. 1986 A reduced-order model of boiling water reactor linear dynamics – Nuclear Technology 75: 15-22.
- March-Leuba, J. & W.T. King 1987 Development of a real-time stability measurement system for boiling water reactors – Transactions of the American Nuclear Society 54: 370-371.
- Salmon, L. & D.V. Booker 1972 FATAL - a general purpose computer program for fitting experimental data to any required function – Atomic Energy Research Establishment (Harwell) Report AERE-R 7129: 37 pp.
- Upadhyaya, B.R. & M. Kitamura 1981 Stability monitoring of boiling water reactors by time series analysis of neutron noise – Nuclear Science and Engineering 77: 480-492.
- Upadhyaya, B.R., J. March-Leuba, D.N. Fry & M. Kitamura 1982 Application of noise analysis methods to monitor stability of boiling water reactors – Progress in Nuclear Energy 9: 619-630.
- Van der Hagen, T.H.J.J. & J.E. Hoogenboom 1988 Fast measurements of the in-core coolant velocity in a BWR by neutron noise analysis – Annals of Nuclear Energy 15: 439-448.
- Van der Hagen, T.H.J.J., H. van Dam, J.E. Hoogenboom, E.B.J. Kleiss, W.H.M. Nissen & W.J. Oosterkamp 1986 Analysis of natural circulation BWR dynamics with stochastic and deterministic methods – Proceedings of the 6th Power Plant Dynamics, Control & Testing Symposium (Knoxville, 14-16 April 1986): 48.01-48.17.
- Van der Veer, J.H.C. 1982 Noise analysis of the Dodewaard boiling water reactor: characteristics and time history – Progress in Nuclear Energy 9: 607-618.

Chapter 9

Stability monitoring by means of the rms ratio and variations of the in-core coolant velocity

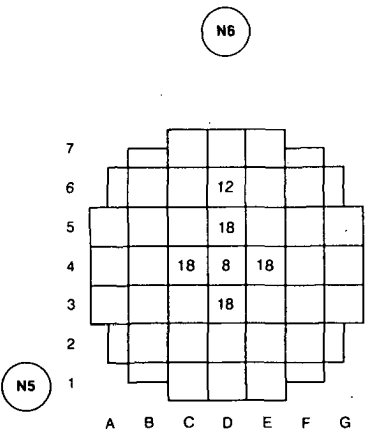
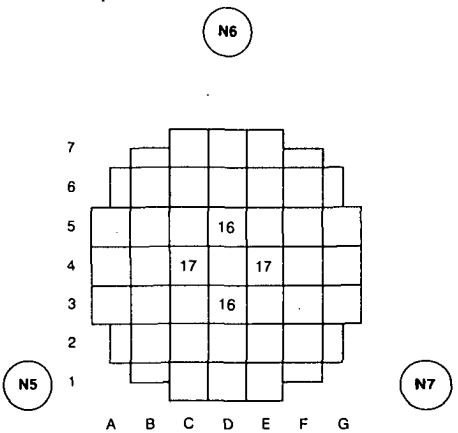
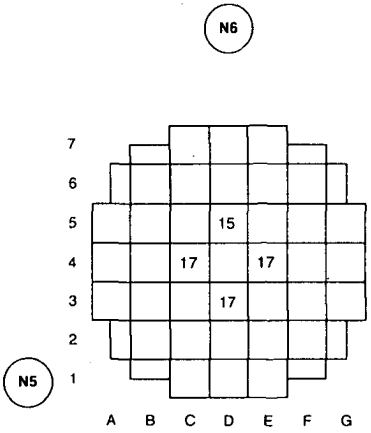
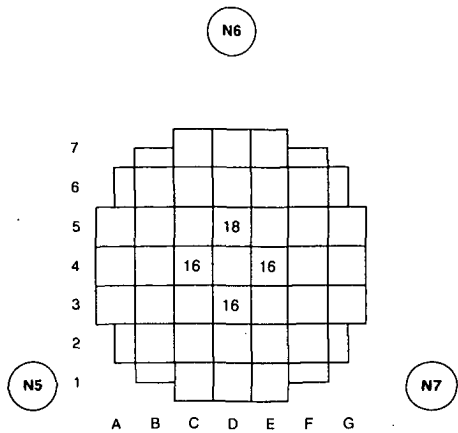
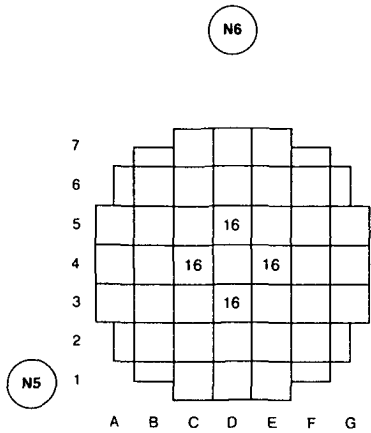
Positive results regarding surveillance of the stability of the core as a whole by using ex-vessel neutron detectors were reported in the preceding chapters. There remains to be discussed the possibility of monitoring local decreases in stability (such as channel-flow instabilities). Experiments dealing with local stability changes were therefore performed during cycle 19 of the Dodewaard reactor. The changes in stability were obtained by slightly changing the control-rod pattern. The effect of this change of the rod pattern was calculated by a Flare-type code (Delp et al., 1964). This code calculates the discretised power distribution for a three-dimensional geometry. The numerical model is based on a one-group transport kernel theory including only k_{∞} and M^2 (the neutron migration area) as parameters. The core geometry is simplified by replacing the reflector by an albedo (i.e. the ratio between the neutron current out of the reflector back into the core to the current into the reflector).

The signals of the three ex-vessel neutron detectors were analysed in order to study the behaviour of the rms ratio - the newly introduced measure for stability.

A second topic dealt with here is the use of variations of the in-core coolant velocity (derived by correlation of the noise of the signals of a TSPND) for stability monitoring. The velocity variations at different radial and axial core positions are compared for this purpose.

Experimental conditions

The relevant reactor signals were recorded at five different control-rod patterns (Fig. 64). The various cases (Fig. 64) will be termed *A*, *B*, *C*, *D* and *E*. The axial control-rod positions are numbered from 0 to 23, corresponding with the discrete control-rod positions in the Dodewaard reactor; 0 corresponds with a fully inserted rod, whereas 23 corresponds with a completely withdrawn rod. The number 23, in the case of a withdrawn rod, is replaced by a blank in Figure 64. All but four control rods were withdrawn in cases *A-D*.



Case A (upper left): power 183 MW(th).
date: 1988-04-07.

Case B: upper right): power 183 MW(th).
date: 1988-03-31.

Case C (middle left): power 183 MW(th).
date: 1988-03-29.

Case D (middle right): power 183 MW(th).
date: 1988-03-31.

Case E (lower left): power 177 MW(th).
date: 1988-05-03.

Fig. 64
Experimental conditions A, B, C, D and E.

Unfortunately, the computer code TIPPEL, normally used by the plant owner for calculating local power and void fractions from neutron TIP measurements, cannot handle an asymmetrical control-rod pattern. This is due to the fact that TIP curves can only be taken in one quadrant of the core. Only the TIPPEL results for case A are therefore given in Table 14.

Table 14

Radial peaking factors and outlet void fractions for one core quadrant for case A calculated with TIPPEL. The positions of inserted control rods are also given.

<i>radial peaking factor</i>	0.41	0.50	0.54						
	0.40	0.55	0.73	0.89	1.05				
	0.38	0.36	0.80	1.07	1.23	1.28			
	0.55	0.80	1.21	1.27	1.37	1.42			
	0.41	0.72	1.07	1.27	1.42	1.37	1.41		
								16	
	0.49	0.89	1.24	1.38	1.38	1.43	1.26		
	0.54	1.05	1.28	1.43	1.42	1.27	1.19	1.20	
								16	
								1.20	1.24

<i>exit void fraction</i>	0.349	0.387	0.404						
	0.343	0.407	0.474	0.526	0.571				
	0.336	0.440	0.499	0.575	0.613	0.623			
	0.408	0.499	0.610	0.621	0.642	0.650			
	0.350	0.471	0.577	0.622	0.650	0.641	0.648		
								16	
	0.384	0.526	0.615	0.643	0.643	0.652	0.619		
	0.406	0.572	0.623	0.653	0.650	0.622	0.604	0.607	
								16	
								0.607	0.614

The local power and the void fractions for all cases were calculated by using the computer code LWRSIM-1, which does not use experimental data. This code is an improvement of the FLARE code (Delp et al., 1964). LWRSIM-1 uses k_{∞} as input data, plus the neutron migration area of every element for a number of void fractions and burn-up states. These values are calculated by means of the neutron transport code LWRWIMS (Halsall, 1982). More information on TIPPEL, LWRSIM-1 and their application to the Dodewaard BWR can be found in Oosterkamp (1987). LWRSIM-1 is able, after slight modification, to calculate peaking factors and exit void fractions for situations with an asymmetrical control-rod pattern.

Appendix 1 gives the results for cases A and B. Note the differences in peaking factors and void fractions between the Toppel and the LWRSIM-1 calculation for case A. These differences - up to 11% relatively in peaking factor - reflect the inaccuracy of the methods. The most important data from these calculations concerning system safety are of course high peaking factors and high void fractions. The two methods agree very well when this is taken into account: the highest peaking factor, being 1.43, corresponds perfectly (as the relation peaking-factor/void-fraction used for the two methods is the same, the outlet void fraction is also identical). In order to compare the local channel-flow stabilities of the various cases, Figure 65 presents the peaking factors averaged over four fuel bundles for case A and the changes in the peaking factors of the other cases with respect to case A ($= \Delta P_{\text{fuel bundle}} \cdot 164 \cdot 100\% / 183 \text{ MW}$; a change of 1% therefore corresponds with an averaged increase of 11.2 kW in fuel-bundle power).

Stability analysis using the ex-vessel neutron flux

Two topics will be dealt with in this section: (1) stability monitoring using the rms ratio, and (2) the influence of the reflector on the rms ratio.

Stability monitoring using the rms ratio - Figure 66 presents the normalised auto-power spectral densities (NAPSD) of the signals of the ex-vessel neutron detector N6 for cases B and E in comparison with the NAPSD of the normal (symmetrical) case A.

The conclusions from this figure are the same as those already drawn in Chapter 8:

- (1) the reactor is very stable (as is usual for the Dodewaard reactor, especially when it is not at the end of a cycle) as there is no spectrum peaking near the resonance frequency of 1.1 Hz,
- (2) the difference between the spectra is very small.

The stability can also be judged from the auto-correlation function of the neutron noise (Chapter 8). It is obvious from Figure 67 that the component of 1.1 Hz is strongly damped, indicating a very stable system. As in

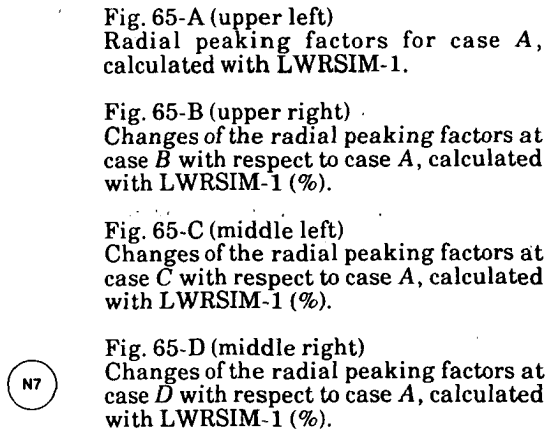
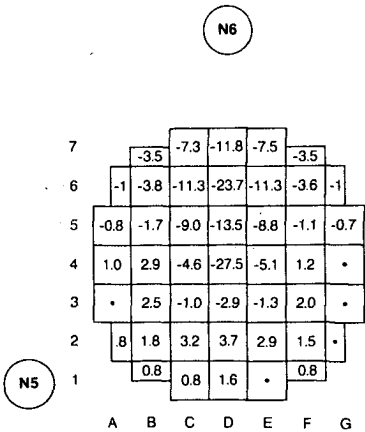
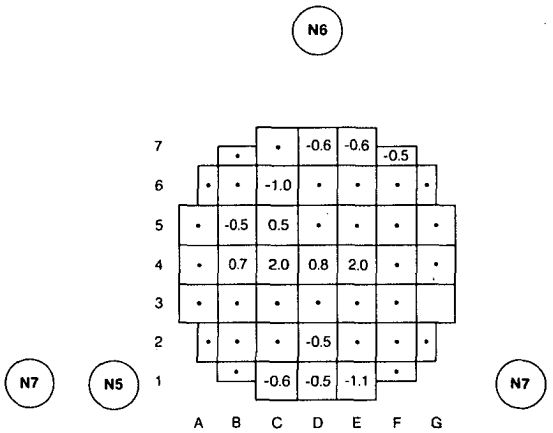
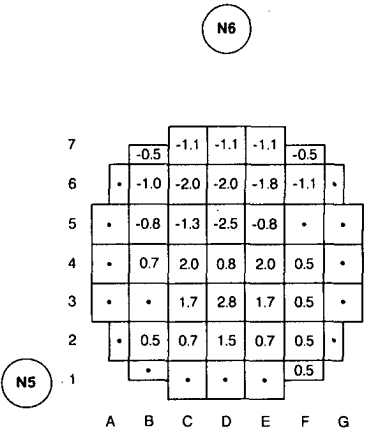
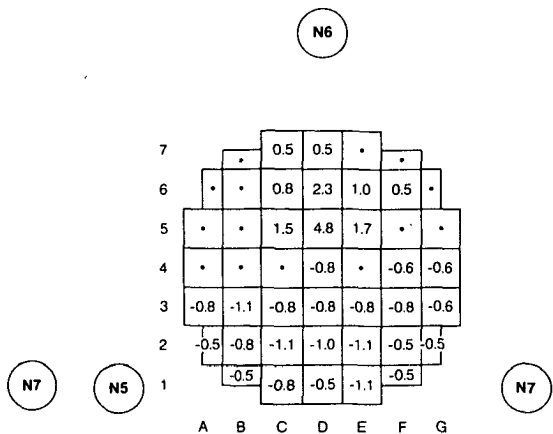
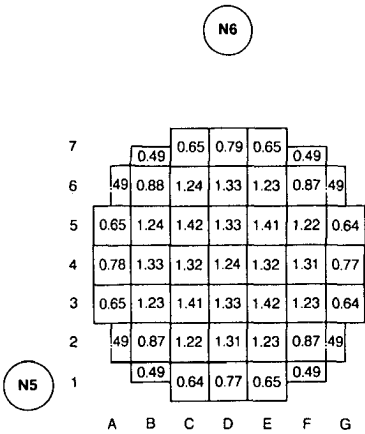


Fig. 65-A (upper left)
Radial peaking factors for case A, calculated with LWRSIM-1.

Fig. 65-B (upper right)
Changes of the radial peaking factors at case B with respect to case A, calculated with LWRSIM-1 (%).

Fig. 65-C (middle left)
Changes of the radial peaking factors at case C with respect to case A, calculated with LWRSIM-1 (%).

Fig. 65-D (middle right)
Changes of the radial peaking factors at case D with respect to case A, calculated with LWRSIM-1 (%).

Fig. 65-E (lower left)
Changes of the radial peaking factors at case E with respect to case A, calculated with LWRSIM-1 (%).

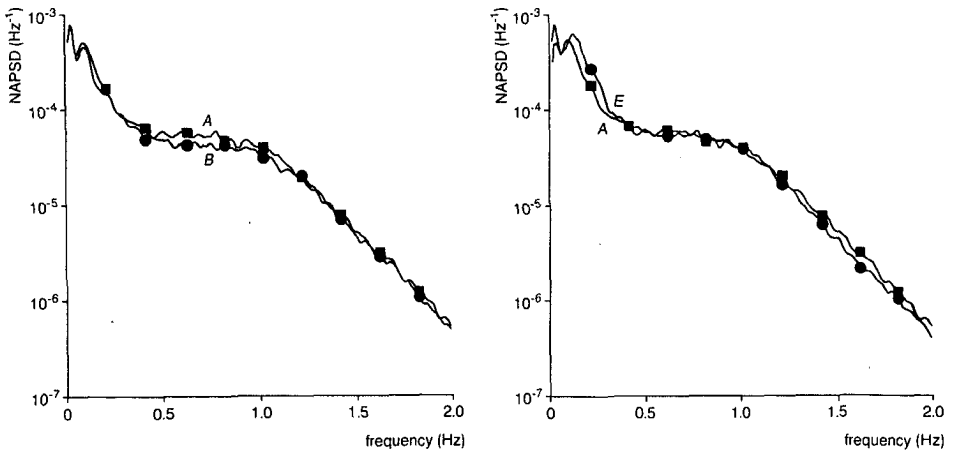


Fig. 66
Normalised auto-power spectral density of N6.
Left: for cases A and B. Right: for cases A and E.

Chapter 8, it can be noted that this function is not simply related to a second-order system as was the case described by March-Leuba & King (1988) but that it also has a slowly decaying component (with a time constant of several seconds), not related to the stability of the core around 1.1 Hz.

The measure for reactor stability introduced in Chapter 8, the rms ratio of the neutron flux (i.e. the ratio of the rms value from 0.8-1.3 Hz and that from 0.4-0.8 Hz), is given in Table 15 for the various cases. The difference from the rms ratio in case A is also given. The signals of the three ex-vessel neutron detectors were sampled with 176 ms sampling time and were Fourier-transformed using 256 samples per record; the total number of records is given in Table 15 as well.

The standard deviation of the rms ratio was calculated taking the correlation between spectrum points due to spectral leakage into account. A detailed derivation is given in Appendix 2. It follows from the analysis presented there that the standard deviation of the estimated rms ratio due to the finite measuring time decreases with the square root of the total measuring time. This holds for both the standard deviation of a single spectrum point and the standard deviation due to spectral leakage.

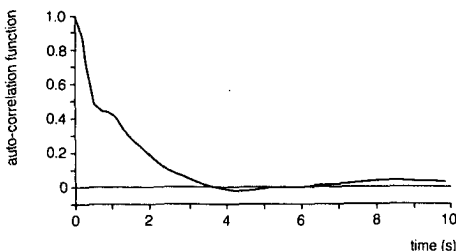


Fig. 67
Auto-correlation function of the ex-vessel neutron flux for case A.

Table 15
Rms ratio of the ex-vessel neutron flux.

case	records	rms ratio	σ (rms ratio) (%)	relative difference with A (%)
A	225	N5: 0.900	0.74	-
		N6: 0.854	0.74	-
		N7: 0.891	0.74	-
B	165	N5: 0.934	0.86	3.8
		N6: 0.887	0.86	3.9
		N7: 0.933	0.86	4.7
C	150	N5: 0.905	0.90	0.56
	150	N6: 0.851	0.91	-0.35
	6	N7: 0.877	4.8	-1.6
D	150	N5: 0.912	0.90	1.3
		N6: 0.864	0.91	1.2
		N7: 0.902	0.90	1.2
E	547	N5: 0.908	0.48	0.89
		N6: 0.836	0.48	-2.1
		N7: 0.902	0.48	1.2

Table 16
Standard deviation of the rms ratio and the decay ratio, DR, as a function of the measuring time.

measuring time	σ (rms ratio) (%)	σ (DR) (%) (DR = 0.1)	σ (DR) (%) (DR = 0.25)	σ (DR) (%) (DR = 0.5)
2 h	0.88	3.1	1.8	1.3
1 h	1.24	4.4	2.5	1.9
30 min	1.75	6.2	3.5	2.6
10 min	3.0	11	6.0	4.5
1 min	9.6	34	19	15
30 s	13.6	48	27	21

Table 16 presents the standard deviation of the rms ratio for various measuring times derived for the normal situation, case A. The standard deviation of the decay ratio, calculated from the relation presented in Figure 62, is given for a decay ratio of 0.1, 0.25 and 0.5, assuming a neutron-noise spectrum equivalent to that of case A. It is seen that using the rms ratio is a most suitable method for on-line stability monitoring, in contrast with the system developed by March-Leuba & King (1988), which is based on AR-modelling of the neutron noise.

Figure 68 shows the rms ratio as a function of the decay ratio for a second-order system with a resonance frequency of 1.1 Hz. The relation is more or less linear in the region that applies to the Dodewaard reactor (a decay ratio between 0.1 and 0.3). The measured rms ratio of the ex-vessel neutron flux is lower due to the influence of the first-order part of the system and the influence of the higher noise spectrum at low frequencies ($f < 0.6$ Hz). It can be seen that, under less stable conditions than those observed in the Dodewaard reactor (high decay ratio), the sensitivity increases, leading to a standard deviation in the estimated decay ratio smaller than the standard deviation presented in Table 16, which was derived from the relation of Figure 62.

The rms ratio of the N5 signal is approximately 0.9 for all cases. According to a linear extrapolation of Figure 62 this corresponds with a decay ratio of 0.10. This again points to a very stable system. This decay ratio is significantly smaller than the decay ratios mentioned in Chapter 8, in which end-of-cycle conditions were considered. This high stability at the beginning of a cycle can be explained by the fact that the fresh elements have a larger fuel time constant due to a lower gap conductance (see Chapter 7), which gives better stability (March-Leuba, 1984). Oosterkamp (1987) suggests that not only are these bundles more stable but that they have a stabilizing effect on other bundles as well, as the bundles are strongly coupled neutronically.

It is striking that the rms ratio of the signal of N6 is always lower than those of N5 and N7 (Table 15), because N6 faces the core from a different point of view (see Fig. 2); the detector is shielded from the core by an extra amount of water (0.1 m: W.H.M. Nissen, private communication, 1988). This aspect will be dealt with in more detail in the next subsection.

The rms ratios of N5 and N7, positioned at equivalent sides of the core, correspond very well for all cases. It should be noted that only six

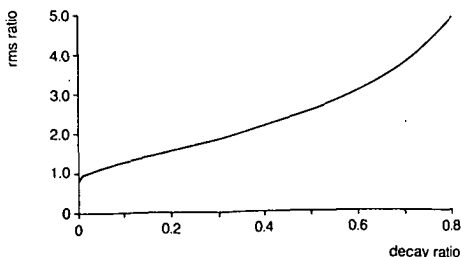


Fig. 68
The rms ratio as a function of the decay ratio for a second-order system with a resonance frequency of 1.1 Hz.

records were available for the determination of the rms ratio of N7 at case C so that the statistics for this value are relatively bad.

The various cases will be treated successively.

- (A) A very accurate determination of the rms ratios, with N6 having a lower rms ratio than N5 and N7 due to the extra shielding (see the next subsection).
- (B) Control rod D5 was withdrawn two notches (the total power was maintained at 183 MWth by lowering the water level in the vessel). This led to higher local power in the elements surrounding D5 and thus to lower local stability. As the detector signal is dominated by the least stable elements in its vicinity (Chapter 2), all three rms ratios were affected: the increase in the rms ratios corresponds with a decrease of stability. The method presented for stability monitoring is obviously very sensitive as all the detectors registered the small change in stability (the maximum difference in peaking factor between cases A and B was only 4.8%; the maximum difference in exit void fraction was only 0.01 (Appendix 1)). N.B.: it is very difficult - were it possible - to detect such a small change in stability (an increase of the decay ratio from approximately 0.10 to 0.12) directly from the decay ratio, as this would involve fitting of either the spectrum or the impulse response (Chapter 8). The decrease in element power of 1.1% in the fuel bundles close to N5 and N7 was not strong enough to cause an increase of the rms ratio of N6 significantly higher than the increase of the rms ratios of N5 and N7.
- (C) Three control rods were withdrawn by one notch; control rod D5 was inserted by one notch. This resulted in a stability increase in the elements surrounding D5 (facing detector N6) and a decrease for the other central elements (facing N5 and N7), as can be seen from Figure 65. The rms ratios were not affected significantly, due to the fact that the decrease in stability of the elements surrounding D3 was compensated by the increase in stability of the elements close to D5. The rms ratio of N7 has relatively bad statistics due to the short signal recordings available.
- (D) Control rods C4 and E4 were withdrawn by one notch; power was maintained by water-level lowering. The situation was again symmetrical, with only a few minor changes in the very centre of the core. However, as the power was more concentrated in the elements C4 and E4, the stability of the core decreased. The rms ratios measured were higher than those for case A due to the decrease in stability. It should be noted that the maximum difference between the exit void fractions of A and D was only 0.004.
- (E) This measurement was made one month after the others. Control rod D6 was inserted up to position 12. This led to a strongly asymmetrical flux profile (Fig. 69 displays the distortion of the axial flux profile at position 5C due to the insertion of control rod D6 in comparison with

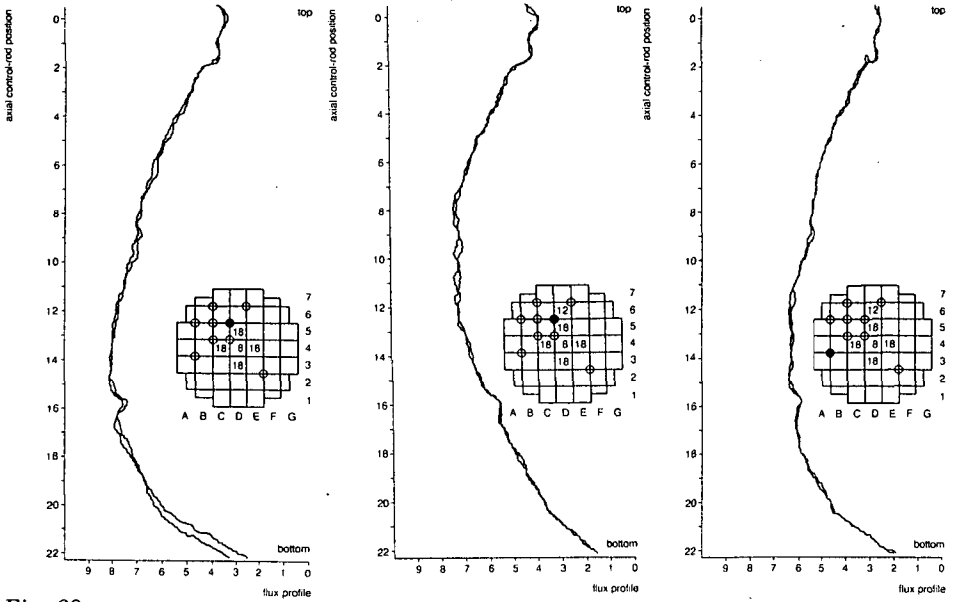


Fig. 69

Tip curves measured from top to bottom and from bottom to top.

Left: at position 5C with control rod D6 at position 23.

Middle: at position 5C with control rod D6 at position 12.

Right: at position 3A with control rod D6 at position 12.

the still normal profile at position 3A). Note that the total power was less than during the other experiments. The rms ratio of N6 - facing the most stable side of the core - dropped 2.1%, whereas the ratios of N5 and N7 increased by 0.9 and 1.2%, respectively. These changes of the rms ratios correspond with the changes of the local element power (Fig. 65).

It can thus be stated that the variations of the rms ratios with the different control-rod patterns are qualitatively perfectly well understood and lead to the conclusions that

- (1) stability monitoring using the rms ratio is a very sensitive method,
- (2) the three ex-vessel detectors cover the entire core,
- (3) the responses of the detector signals correspond with the local stability changes of the core,
- (4) local effects can be distinguished by using three detectors.

The influence of the reflector on the rms ratio - It follows from Figure 2 that detector N6 faces the core from a point of view different from that of detectors N5 and N7. This detector position is shielded from the core by an extra amount of water (0.1 m: W.H.M. Nissen, private communication, 1988). The effect of this extra water layer on the rms ratio measured can easily be derived using Equation (41), where the neutron-flux variations

caused by a mono-energetic, sinusoidally modulated neutron point source in a homogeneous non-multiplying medium were calculated (Beckurts & Wirtz, 1964). It is derived for the detector response δR that

$$\delta R(r, t) = \Sigma_d \frac{\delta Q}{4\pi r D} \exp(-r/L_\omega) \exp(j\omega t) \quad (\text{Eq. 103})$$

where

$$\frac{1}{L_\omega} = \sqrt{\frac{1}{D} \left(\Sigma_a + \frac{j\omega}{v} \right)} \quad (\text{Eq. 104})$$

A first-order approximation for $1/L_\omega$ gives

$$\frac{1}{L_\omega} \approx \left(1 + \frac{j\omega}{2v\Sigma_a} \right) \sqrt{\frac{\Sigma_a}{D}} \quad (\text{Eq. 105})$$

The attenuation in a first-order approximation is therefore independent of the frequency of modulation. This implies that the influence of the reflector on the rms ratio is a second-order effect; Equation (104) will therefore be used here.

It is derived that for the attenuation, $w(r, f)$,

$$w(r, f) = \exp \left\{ -r \left(\left(\frac{\Sigma_a}{D} \right)^2 + \left(\frac{2\pi f}{vD} \right)^2 \right)^{1/4} \cos(\theta/2) \right\} / r \quad (\text{Eq. 106})$$

where

$$\theta = \arctan \left(\frac{2\pi f}{v\Sigma_a} \right) \quad (\text{Eq. 107})$$

The effect of an extra water layer of thickness d on the rms ratio can be calculated using

$$\text{rms-ratio}_{N_6} = \sqrt{\int_{0.8}^{1.3} \Gamma(f) w^2(d, f) df} / \sqrt{\int_{0.4}^{0.8} \Gamma(f) w^2(d, f) df} \quad (\text{Eq. 108})$$

where $\Gamma(f)$ represents the ex-vessel neutron spectrum without extra attenuation. As $w(d, f)$ is a monotonically decreasing function of f , the rms ratio measured by detector N6 will be smaller than the rms ratio measured by detector N5.

Assuming that $\Gamma(f)$ is flat for 0.4-1.3 Hz, the estimated rms ratios measured by N5 and N6 are (using reflector values of the thermal group for Σ_a , D and v): 1.12 for N5, 1.10 (0.1 m extra water) and 1.08 (20 cm extra water) for N6. The rms ratio measured is lower for all detectors as the measured spectrum decreases for frequencies higher than 1.1 Hz. Taking this decrease into account, the following rms ratios are obtained: 0.87 for N5, 0.86 (0.1 m extra water) and 0.85 (0.2 m extra water) for N6.

This holds for the response of a point detector to a point source. Although the situation in the Dodewaard core is much more complex, the results derived above show that detector N6 will measure a lower rms

ratio than the other two neutron detectors, due to the filtering by the extra water layer between the detector and the core.

Variations of the in-core coolant velocity

The in-core coolant velocity is derived by correlating the noise of the signals of the two detectors of the TSPND. The theoretical basis of velocity determination by neutron-noise correlation was described, together with the detector, in Chapter 3.

The variations of the in-core velocity are of importance to the thermal-hydraulic stability (Chapter 8). A decrease in channel-flow stability is expressed by an increase in velocity variations. The variations in coolant velocity are determined by calculating the maximum of the cross-correlation function (CCF) over 128 samples every 0.64 s ($f_{\text{Nyquist}} = 0.78$ Hz). A detailed outline of this method was given in Chapter 5. The variations of the measured velocity have two causes:

- (1) real variations of the in-core coolant velocity,
- (2) statistical inaccuracy of the method due to a finite measuring time.

The shorter the time over which the CCF is determined, the worse are the statistics.

The standard deviation of the estimated standard deviation of the measured velocity ($\sigma[\sigma_{\text{meas } v}]$) is estimated using the relation (Bendat & Piersol, 1971: 259)

$$\sigma(\sigma_{\text{meas } v}) = \frac{\sigma_{\text{meas } v}}{\sqrt{2n}} \quad (\text{Eq. 109})$$

which is an estimate for n independent Gaussian-distributed velocity values.

As described in Chapter 5, the inaccuracy of the method (which results in changes of the measured velocity not related to actual velocity variations) is estimated by least-squares linear fitting of the phase of the cross spectrum from 0-35 Hz and calculation of the standard deviation of the fitted slope for each case/position separately. True velocity variations are then calculated by subtracting the variances (σ^2):

$$\sigma_v^2 = \sigma_{\text{meas } v}^2 - \sigma_{\text{method}}^2 \quad (\text{Eq. 110})$$

The following three subsections will deal with (1) the axial profile of velocity variations, (2) the radial profile of velocity variations, and (3) a comparison of the velocity variations at one core position.

Axial profile of velocity variations - The axial profile of velocity variations was measured in position 4D for the situation presented in Chapter 3. The resulting values are presented in Table 17, where the position of the centre of the detector above the bottom of the core is referred to as 'position'.

Table 17

Axial profile of velocity variations measured in position 4D.

position (cm)	V (cm·s ⁻¹)	$\sigma_{\text{meas V}}$ (%)	$\sigma(\sigma_{\text{meas V}})$ (%)	σ_{method} (%)	σ_V (%)
28	1.32	9.07	0.12	1.2	9.0
58	1.95	4.52	0.06	2.4	3.8
88	2.56	4.31	0.06	2.6	3.4
118	2.96	5.36	0.08	3.6	4.0
148	3.29	6.37	0.09	2.8	5.7
179	3.12	19.4	0.3	9.9	17

The table indicates that the variations in the coolant velocity are greatest near the outer ends of the fuel bundles, which is expected for the flow near the outlet of the fuel bundle but is surprising for the inlet flow. The large fluctuations measured at a low axial position are due to the fact that this is the region of sub-cooled boiling. The velocity of steam bubbles close to the fuel (where they are formed) is therefore measured. These bubbles rise after detachment, with a low velocity, close to the wall and increase their velocity when dragged by the bulk in which they slowly condense (Bowring, 1962).

Radial profile of velocity variations - Velocity measurements were performed in cases A, B and E.

The detector was positioned at a level of 1.105 m above the bottom of the core in detector tube 4C during the first two measurements. Four positions were used during the measurements in case E. Table 18 presents the velocity values obtained and the averaged coherence between the two detector signals (0-35 Hz). The axial detector position in tube 6B differed from the others, as the coherence between the noise signals at a position of 1.105 m was too low for performing accurate velocity measurements. This coherence is greatly influenced by the flow pattern in the surrounding elements. As the local relative power near position 6B was low, a flow pattern (and therefore a coherence) corresponding with the flow patterns of the other measurements existed in a higher part of the core. The detector was therefore placed at a higher axial position (1.58 m), where the coherence (though smaller than for the other measurements) was satisfactory.

The measured velocity variations around these detector positions are shown in Table 19. Comparison of the variations of the velocity as shown in Table 19 with the changes of the peaking factor presented in Figure 65 leads to the conclusion that the velocity variations are not representative of the local core stability: the velocity variations were greatest near posi-

tion 6B, which is the most stable core region investigated. The variations at positions 2E and 4B (at almost equivalent core positions) correspond well. Other effects are clearly dominant.

Lübbesmeyer (1984) states that both the void fraction and the flow pattern in a fuel bundle in the neighbourhood of the detector affect the contribution of the bundle to the velocity measured. Table 20 gives the void fractions in the neighbouring bundles at the axial position of the detector for the various cases. These void fractions were calculated by LWRSIM-1. It is striking to note from this table that the void fractions in the bundles surrounding detector positions 4C and 6B in case *E* differ more than those at the other positions. These are the positions where coherence is the lowest (Table 18) and where the measured variations in coolant velocity are largest (Table 19). The conclusion can therefore be drawn that the relatively high variations measured for the coolant velocity around detector positions 4C and 6B are due to the asymmetry in flow-pattern/ void-fraction/coolant-velocity in the surrounding fuel bundles.

Table 18
In-core coolant velocities measured with the TSPND.

case	detector position (cm)	average coherence	velocity (m·s ⁻¹)
A	4C, 111	0.40	2.91
B	4C, 111	0.41	3.23
E	4C, 111	0.36	2.77
E	6B, 158	0.22	3.11
E	2E, 111	0.52	3.40
E	4B, 111	0.59	3.48

Table 19
Velocity variations at several core positions for case *E*.

position	$\sigma_{\text{meas } v}$ (%)	$\sigma(\sigma_{\text{meas } v})$ (%)	σ_{method} (%)	σv (%)
4C	5.17	0.05	3.0	4.2
6B	8.92	0.07	3.7	8.1
2E	2.40	0.03	1.5	1.9
4B	1.99	0.04	1.3	1.5

Table 20

Void fractions in the bundles surrounding a detector position, calculated with LWRSIM-1.

case	void fractions			
A	0.52 0.48			
	----4C-----			
	0.48 0.46			
B	0.53 0.50			
	----4C-----			
	0.48 0.47			
E	0.48 0.42	0.38 0.48	0.52 0.47	0.51 0.51
	----4C-----	----6B-----	----2E-----	----4B-----
	0.44 0.33	0.49 0.54	0.51 0.47	0.53 0.50

Comparison of velocity variations at one core position - Table 21 compares the velocity variations measured at the same core position (4C) with a symmetrical and an asymmetrical control-rod pattern (cases A and B). Δv is the time between consecutive velocity values. Figure 70 shows the velocity for case B as a function of time. It appeared to be possible to calculate velocity variations for these cases by using only 64 samples per CCF (10 ms sampling time). Thus, the velocity is calculated every 0.32 s ($f_{Nyquist} = 1.56$ Hz). Figure 71 shows the results (again for case B).

Table 21

Variations of the in-core coolant velocity in case A and case B.

case	Δv (s)	$\sigma_{meas v}$ (%)	$\sigma(\sigma_{meas v})$ (%)	σ_{method} (%)	σ_v (%)
A	0.64	4.36	0.05	2.1	3.8
A	0.32	6.12	0.05	3.1	5.3
B	0.64	3.23	0.04	2.1	2.5
B	0.32	5.02	0.04	3.1	4.0

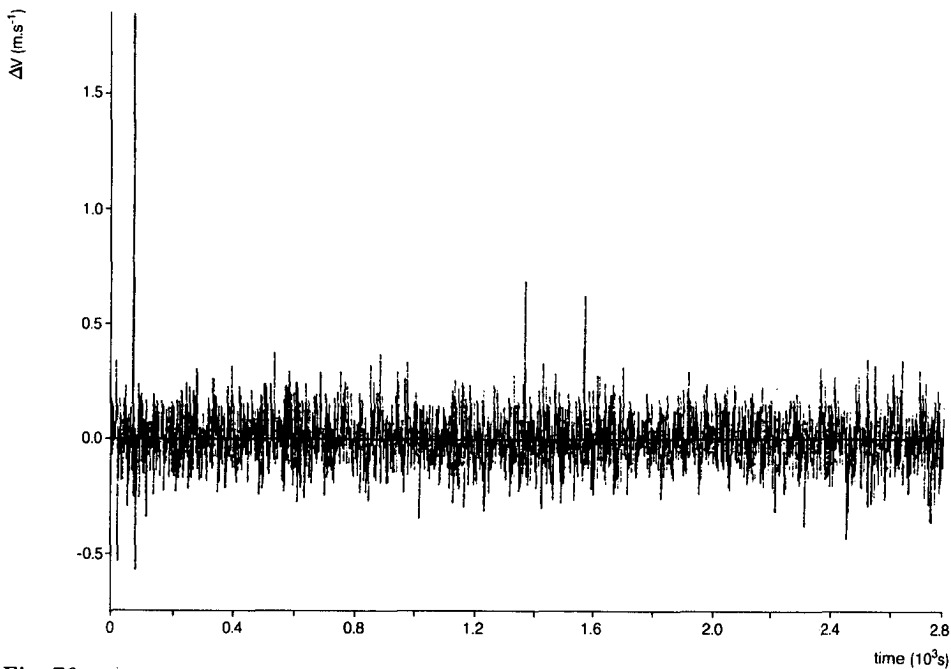


Fig. 70
 Measured variations of the in-core coolant velocity in case *B* (CCF calculated over 128 samples).

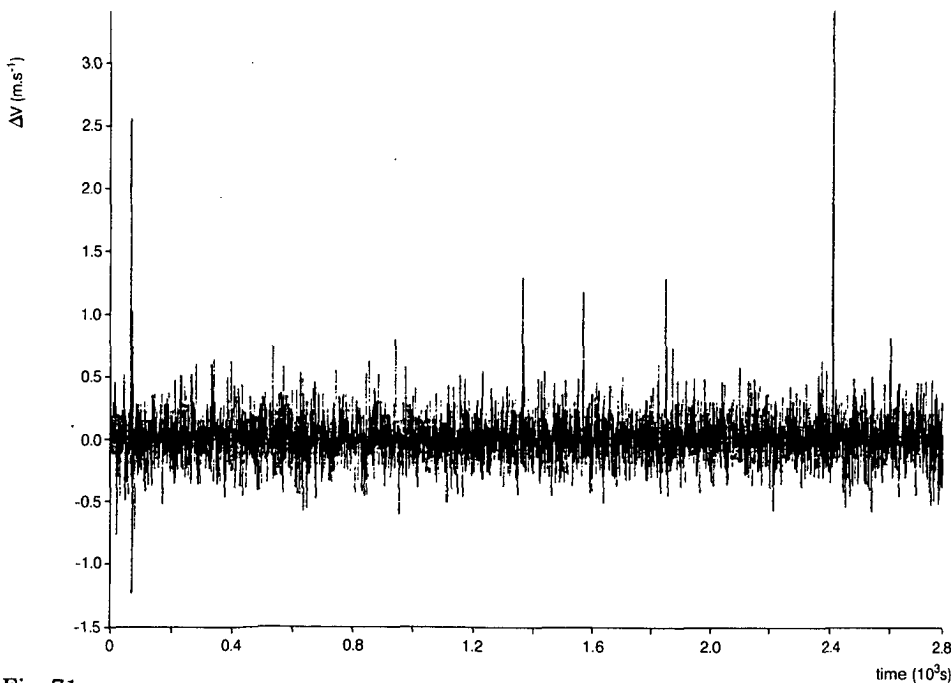


Fig. 71
 Measured variations of the in-core coolant velocity in case *B* (CCF calculated over 64 samples).

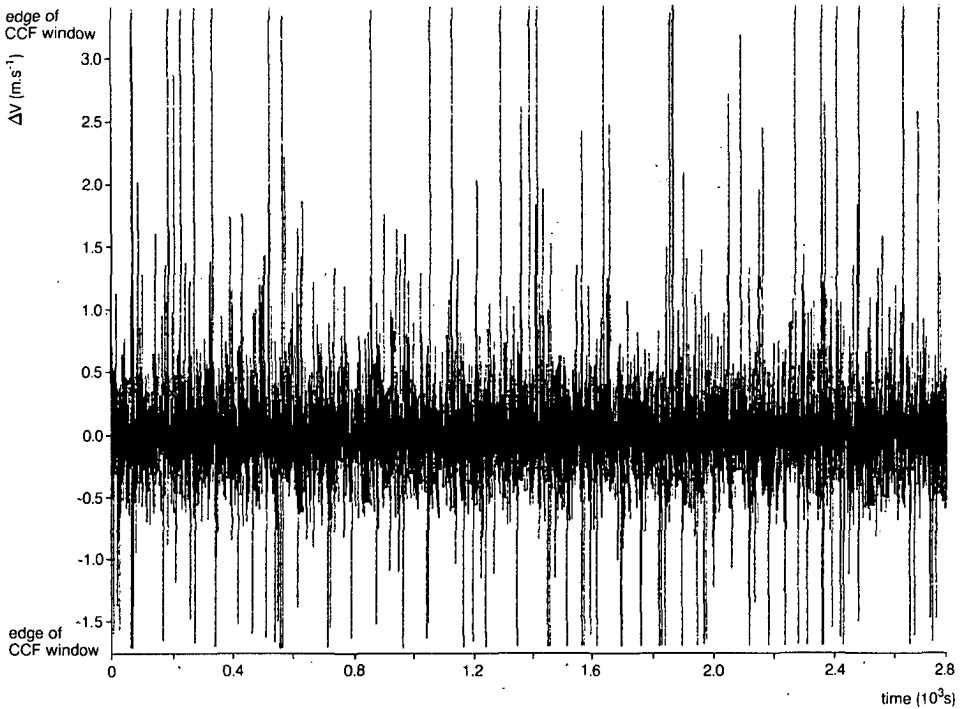


Fig. 72
Measured variations of the in-core coolant velocity in case *B* (CCF calculated over 32 samples).

A further reduction, to 32 samples per CCF, resulted in an inaccurate velocity determination as the maximum of the CCF jumps from one peak to another (Fig. 72).

It can be noted from Table 21 that the velocity variations in the centre of the core are very small, pointing to a stable system. However, the variations are larger at the symmetrical control-rod pattern (case *A*) than at the asymmetrical pattern (case *B*). This is unexpected as the core is more stable in case *A*, especially around detector position 4C (see above). Figure 73, giving the spectra of the velocity for both cases, shows this effect as a function of frequency. An explanation might be that the flow pattern at case *B* differs from that at case *A*. As the power is more concentrated around element D5, the local void fraction is higher in case *B* than in case *A*. It is possible that the variation in steam velocity decreases with void fraction (consider for instance churn and annular flow). Apparently, this change of flow pattern overrules the increase in velocity variations due to the stability decrease.

It is clear from the above mentioned findings that the standard deviation of the velocity is not an absolute measure of the channel-flow stability of the elements surrounding the detector. The increase in

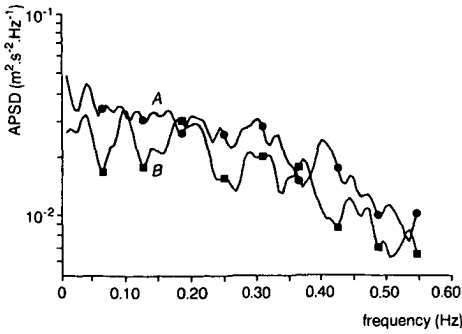


Fig. 73
Auto-power spectral density of the in-core coolant velocity for case A and B.

velocity variations caused by a decrease in channel-flow stability seems to be masked by two other effects:

- (1) the asymmetry between flow patterns in the four fuel bundles surrounding the detector,
- (2) the flow pattern in the four fuel bundles.

Conclusions

Surveillance of core stability by using the rms ratio of the signals of the three ex-vessel neutron detectors, N5, N6 and N7, seems very promising. The local stability changes on different (symmetrical and asymmetrical) control-rod patterns are reflected in the rms ratio of the signal of the corresponding neutron detector.

The method presented here can be applied on-line under normal operating conditions. More sophisticated methods of stability analysis, as presented in Chapter 8, can be applied occasionally as verification.

The axial profile measured for velocity variations corresponds with expectations, except for the velocity variations at the fuel-bundle inlet, where relatively large variations were measured. These are attributed to the characteristics of subcooled boiling.

The radial profile does not correspond with the local channel-flow stability as the local flow patterns play a dominant role. The variations of in-core coolant velocity are therefore not an absolute measure of local channel-flow stability. However, it must be stressed that the reactor under consideration is very stable, resulting in small velocity variations and that the stability changes created were very small.

References

- Albrecht, R.W., R.D. Crowe, D.J. Dailey, M.J. Damborg & G. Kosaly 1982 Measurement of two phase flow properties using the nuclear reactor instrument – *Progress in Nuclear Energy* 9: 37-50.
- Beckurts, K.H. & K. Wirtz 1964 *Neutron physics* – Springer-Verlag (Berlin): 444 pp.
- Behringer, K., G. Kosaly & Lj. Kostic 1977 Theoretical investigation of the local and global components of the neutron-noise field in a boiling water reactor – *Nuclear Science and Engineering* 63: 306-318.
- Behringer, K., G. Kosaly & I. Pazsit 1979 Linear response of the neutron field to a propagating perturbation of moderator density (two-group theory of boiling water reactor noise) – *Nuclear Science and Engineering* 72: 304-321.
- Bell, G.I. & S. Glasstone 1970 *Nuclear reactor theory* – Van Nostrand Reinhold Comp. (New York): 619 pp.
- Bendat, J.S. & A.G. Piersol 1971 *Random data: analysis and measurement procedures* – John Wiley & Sons, Inc. (New York): 407 pp.
- Bouré, J.A., A.E. Bergles & L.S. Tong 1973 Review of two-phase flow instability – *Nuclear Engineering and Design* 25: 165-192.
- Bowring, R.W. 1962 Physical model, based on bubble detachment, and calculation of steam voidage in the sub-cooled region of a heated channel – OECD Halden Reactor Project (Halden) Report HPR-10: 65 pp.
- Delp, D.E., D.L. Fisher, J.M. Haman & M.J. Stedwell 1964 FLARE a three dimensional boiling water reactor simulator – General Electric Company (San Jose) Report GEAP 4598: 94 pp.
- Duderstadt, J.J. & L.J. Hamilton 1976 *Nuclear reactor analysis* – John Wiley & Sons (New York): 650 pp.
- Edenius, M., A. Ahlin & B. Forssen 1986 CASMO-3, a fuel assembly burnup program, user's manual – Studsvik/NFA-86/7 (Nyköping).
- El-Wakil, M.M. 1978 *Nuclear heat transport* – American Nuclear Society (Illinois): 502 pp.
- Federico, A.G. & R. Ragona 1986 Presentation at the 19th Informal Meeting on Reactor Noise (Rome, 4-6 June 1986).
- Fenech, H. 1981 *Heat transfer and fluid flow in nuclear systems* – Pergamon Press (New York): 582 pp.

- Fowler, T.B., M.L. Tobias & D.R. Vondy 1967 Exterminator-2: A Fortran IV code for solving multigroup neutron diffusion equations in two dimensions – Oak Ridge National Laboratory (Oak Ridge, Tennessee) Report ORNL-4078: 75 pp.
- Fry, D.N., J. March-Leuba & F.J. Sweeney 1984 Use of neutron noise for diagnosis of in-vessel anomalies in light-water reactors – United States Nuclear Regulatory Commission (USNRC, Washington) Report NUREG/CR-3303; Oak Ridge National Laboratory (Oak Ridge, Tennessee) Report ORNL/TM-8774; University of Tennessee (Knoxville): 88 pp.
- Garber, D., C. Dunford & S. Pearlstein 1975 ENDF-102, data formats and procedures for the evaluated nuclear data file, ENDF – Brookhaven National Laboratory, Associated Universities Inc. (Upton, New York) Report BNL-NCS-50496.
- Gialdi, E., S. Grifoni, C. Parmeggiani & C. Tricoli 1985 Core stability in operating BWR: operational experience – Progress in Nuclear Energy 15: 447-459.
- Govier, G.W. & K. Aziz 1972 The flow of complex mixtures in pipes – Van Nostrand Reinhold Company (New York): 792 pp.
- Halsall, M.J. 1982 A computer code for light water reactor lattice calculations – Atomic Energy Authority (Winfrith) Report AEEW-R-1498: 113 pp.
- Harris, F.J. 1978 On the use of windows for harmonic analysis with the discrete fourier transform – Proceedings of the Institute of Electrical and Electronics Engineers (IEEE, New York) 66: 51-83.
- HCP (Handbook of Chemistry and Physics, 60th ed.) 1979 – CRC Press (Boca Raton): B-26 + D-182.
- Iriarte Jr., M. 1960 An accurate transfer function for the dynamic analysis of temperature and heat release in cylindrical fuel elements – Nuclear Science and Engineering 7: 26-32.
- Jenkins, G.M. & D.G. Watts 1968 Spectral analysis and its applications – Holden-Day (San Francisco): 525 pp.
- Kataoka, Y., H. Suzuki, M. Murase, I. Sumida, T. Horiuchi & M. Miki 1988 Conceptual design and thermal-hydraulic characteristics of natural circulation boiling water reactors – Nuclear Technology 82: 147-156.
- Kinsey, R. 1979 ENDF-201, ENDF/B summary documentation – Brookhaven National Laboratory, Associated Universities Inc. (Upton, New York) Report BNL-NCS-17541.
- Kleiss, E.B.J. 1982 Determination of BWR incore power feedback effects by radial coherence measurements – Progress in Nuclear Energy 9: 665-674.
- Kleiss, E.B.J. 1983 On the determination of boiling water reactor characteristics by noise analysis – Ph.D. thesis Delft University of Technology; Delftse Universitaire Pers: 147 pp.

- Kleiss, E.B.J., W.J. Oosterkamp & W.H.M. Nissen 1985 Experience with incore neutron and gamma detectors for BWR coolant velocity measurements – *Progress in Nuclear Energy* 15: 735-743.
- Kleiss, E.B.J. & H. van Dam 1981a A twin self-powered neutron detector for steam velocity determination in a boiling water reactor – *Nuclear Technology* 53: 250-256.
- Kleiss, E.B.J. & H. van Dam 1981b Incore power feedback effects deduced from neutron noise measurements – *Annals of Nuclear Energy* 8: 205-214.
- Kleiss, E.B.J. & H. van Dam 1985 A simplified model for the dynamics of a BWR – *Annals of Nuclear Energy* 12: 233-245.
- Kostic, L. 1980 Application of a new correlation method to the local steam transit time determination in a boiling water reactor – *Atomkern-energie* 35: 20-22.
- Kramer, A.W., 1958 *Boiling water reactors* – Addison-Wesley Publishing Company, Inc. (Massachusetts): 563 pp.
- Lahey Jr., R.T. & F.J. Moody 1977 *The thermal-hydraulics of a boiling water nuclear reactor* – American Nuclear Society: 433 pp.
- Lübbesmeyer, D. 1983 On the physical meaning of the fluid velocity measured in BWRs by noise analysis – *Annals of Nuclear Energy* 10: 233-241.
- Lübbesmeyer, D. 1984 *Experimental reactor noise - a review on noise-analytic measurements of thermohydraulic parameters in operating BWRs and their interpretations* – *Progress in Nuclear Energy* 14: 41-93.
- Magurno, B.A. & P.G. Young 1985 ENDF-201 supplement I, ENDF/B-V.2 summary documentation – Brookhaven National Laboratory, Associated Universities Inc. (Upton, New York) Report BNL-NCS-17541: 203 pp.
- March-Leuba, J. 1984 *Dynamic behaviour of boiling water reactors* – Ph.D. thesis University of Tennessee (Knoxville): 277 pp.
- March-Leuba, J. 1986 A reduced-order model of boiling water reactor linear dynamics – *Nuclear Technology* 75: 15-22.
- March-Leuba, J. & W.T. King 1987 Development of a real-time stability measurement system for boiling water reactors – *Transactions of the American Nuclear Society* 54: 370-371.
- March-Leuba, J. & W.T. King 1988 A real-time BWR stability measurement system – *Progress in Nuclear Energy* 21: 181-190.
- Murphy, G.A. 1988 Selected safety-related events, summary of AEOD Special Report S803: Power oscillation at LaSalle 2 – *Nuclear Safety* 29: 356-362.
- Neal, L.G. & S.M. Zivi 1967 The stability of boiling-water reactors and loops – *Nuclear Science and Engineering* 30: 25-38.
- NEI (Nuclear Engineering International) 1988 volume 33, issue number 409: 3.

- Nielsen, L.A., D.W. Pruitt & S.W. Jones 1988 Stability monitoring in boiling water reactors – Transactions of the American Nuclear Society 57: 277-279.
- OECD/NEA (Organisation for Economic Co-operation and Development / Nuclear Energy Agency) 1986 Technical report on the APRMS instability occurrence in Santa Maria de Garona NPP – NEA/Incident Reporting System 677: 17 pp.
- Oosterkamp, W.J. 1987 Reactor physics at the Dodewaard BWR – Kema Scientific & Technical Reports 5: 219-257.
- Priestley, M.B. 1981 Spectral analysis and time series – Academic Press (London): 890 pp.
- Salmon, L. & D.V. Booker 1972 FATAL - a general purpose computer program for fitting experimental data to any required function – Atomic Energy Research Establishment (Harwell) Report AERE-R 7129: 37 pp.
- Sandoz, S.A. & S.F. Chen 1983 Vermont Yankee stability tests during cycle 8 – Transactions of the American Nuclear Society 45: 754-755.
- Seifritz, W. & F. Cioli 1973 On-load monitoring of local steam velocity in BWR cores by neutron noise analysis – Transactions of the American Nuclear Society 17: 451-453.
- Thie, J.A. 1981 Power reactor noise – American Nuclear Society (Illinois): 208 pp.
- Upadhyaya, B.R. & M. Kitamura 1981 Stability monitoring of boiling water reactors by time series analysis of neutron noise – Nuclear Science and Engineering 77: 480-492.
- Upadhyaya, B.R., M. Kitamura & T.W. Kerlin 1980 Multivariate signal analysis algorithms for process monitoring and parameter estimation in nuclear reactors – Annals of Nuclear Energy 7: 1-11.
- Upadhyaya, B.R., J. March-Leuba, D.N. Fry & M. Kitamura 1982 Application of noise analysis methods to monitor stability of boiling water reactors – Progress in Nuclear Energy 9: 619-630.
- Van Dam, H. 1976 Neutron noise in boiling water reactors – Atomkernenergie 27: 8-14.
- Van Dam, H. & E.B.J. Kleiss 1985 Response of incore γ -detectors to parametric fluctuations in a reactor core – Annals of Nuclear Energy 12: 201-207.
- Van der Hagen, T.H.J.J. 1988 Experimental and theoretical evidence for a short effective fuel time constant in a boiling water reactor – Nuclear Technology 83: 171-181.
- Van der Hagen, T.H.J.J. & J.E. Hoogenboom 1988 Fast measurements of the in-core coolant velocity in a BWR by neutron noise analysis – Annals of Nuclear Energy 15: 439-448.
- Van der Hagen, T.H.J.J., W.H.M. Nissen, W.J. Oosterkamp, H. van Dam & J.E. Hoogenboom 1988 Application of noise analysis to stability

- determination of a natural circulation cooled BWR – Progress in Nuclear Energy 21: 753-761.
- Van der Hagen, T.H.J.J., H. van Dam, J.E. Hoogenboom, E.B.J. Kleiss, W.H.M. Nissen & W.J. Oosterkamp 1986 Analysis of natural circulation BWR dynamics with stochastic and deterministic methods – Proceedings of the 6th Power Plant Dynamics, Control & Testing Symposium (Knoxville, 14-16 April 1986): 48.01-48.17.
- Van der Hagen, T.H.J.J. & J. van der Voet 1988 Interpretation of velocities determined by noise analysis for various void fractions and flow regimes in two-phase flow – Progress in Nuclear Energy 21: 565-573.
- Van der Veer, J.H.C. 1982 Noise analysis of the Dodewaard boiling water reactor: characteristics and time history – Progress in Nuclear Energy 9: 607-618.
- Van Engen, W.R. & W.H.M. Nissen 1981 Elongation measurements on fuel assemblies during irradiation in the Dodewaard boiling water reactor – Proceedings of the Enlarged Halden Program Group Meeting on Water Reactor Fuel Performance (Hankö, 1981) HPR-286 (4).
- Waaranderä, Y. & S. Andersson 1981 BWR stability testing: reaching the limit-cycle threshold at natural circulation – Transactions of the American Nuclear Society 39: 868-870.
- Wach, D. 1973 Ermittlung lokaler Dampfblasengeschwindigkeiten aus Rauschsignalen von Incore-Ionisationskammern – Atomwirtschaft 18: 580-582.
- Wach, D. & G. Kosaly 1974 Investigation of the joint effect of local and global driving sources in incore-neutron noise measurements – Atomkernenergie 23: 244-250.
- Wallis, G.B. 1969 One-dimensional two-phase flow – McGraw-Hill (New York): 408 pp.
- WNIH (World Nuclear Industry Handbook) 1989 special issue of Nuclear Engineering International – Reed Business Publishing Company: 25-134.

0.354 0.392 0.415 0.415 0.391 0.353
 0.346 0.421 0.490 0.535 0.562 0.560 0.533 0.489 0.420 0.345
 0.345 0.443 0.527 0.588 0.616 0.621 0.616 0.614 0.537 0.525 0.442 0.344
 0.419 0.527 0.579 0.617 0.635 0.649 0.643 0.634 0.615 0.578 0.525 0.417
 0.353 0.488 0.588 0.617 0.648 0.649 0.635 0.635 0.648 0.646 0.615 0.585 0.485 0.351
 16
 0.392 0.534 0.616 0.635 0.649 0.652 0.630 0.630 0.652 0.647 0.633 0.612 0.530 0.390
 0.414 0.561 0.621 0.649 0.635 0.629 0.613 0.613 0.629 0.634 0.646 0.614 0.556 0.411
 16 16
 0.413 0.559 0.615 0.648 0.635 0.629 0.613 0.618 0.631 0.635 0.646 0.612 0.556 0.411
 0.392 0.532 0.613 0.633 0.648 0.652 0.630 0.631 0.653 0.650 0.634 0.612 0.530 0.390
 16
 0.352 0.486 0.586 0.615 0.646 0.647 0.634 0.635 0.649 0.652 0.617 0.586 0.485 0.351
 0.417 0.525 0.577 0.614 0.632 0.645 0.646 0.633 0.617 0.579 0.525 0.417
 0.343 0.441 0.524 0.585 0.611 0.611 0.611 0.612 0.586 0.526 0.442 0.344
 0.344 0.418 0.486 0.529 0.555 0.555 0.530 0.487 0.419 0.345
 0.351 0.387 0.410 0.410 0.388 0.351

Table A-2
Outlet void-fraction distribution for case A calculated by LWRSIM-1.

Appendix 2: standard deviation of the estimated rms ratio

The rms ratio is defined (Chapter 8) as

$$\text{rms-ratio} = \frac{\sqrt{\int_{0.8}^{1.3} \Gamma_{xx}(f) df}}{\sqrt{\int_{0.4}^{0.8} \Gamma_{xx}(f) df}} \quad (\text{Eq. A-1})$$

This is calculated from the estimated spectrum by

$$\text{rms-ratio} \approx \frac{\sqrt{\Delta f \sum_{i=b}^c C_{xx,i}}}{\sqrt{\Delta f \sum_{i=a}^b C_{xx,i}}} = \frac{\sqrt{\sum_{i=b}^c C_{xx,i}}}{\sqrt{\sum_{i=a}^b C_{xx,i}}} \quad (\text{Eq. A-2})$$

where $\Delta f = 1/(2n\Delta)$ and a, b and c correspond with the frequencies 0.4, 0.8 and 1.3 Hz.

The expression in Equation (A-2) is an estimate of the rms ratio, as $C_{xx}(f)$ is an estimate of $\Gamma_{xx}(f)$. The uncertainty (standard deviation) of the rms ratio can be estimated by calculating the variance (σ^2) of one spectrum point and taking into account the covariance between spectrum points due to spectral leakage.

There holds for the variance of one spectrum point (Jenkins & Watts, 1968: 251) that

$$\frac{\sigma^2(C_{xx}(f))}{\Gamma_{xx}^2(f)} \approx \frac{w_b}{N} \quad (\text{Eq. A-3})$$

Thus, there holds for a sum of spectrum points that

$$\sigma^2\left(\sum_{i=a}^b C_{xx,i}\right) \approx \frac{W_b}{N} \sum_{i=a}^b \Gamma_{xx,i}^2 + \sum_{i=a}^b \sum_{\substack{j=a \\ j \neq i}}^b \text{cov}(C_{xx,i}, C_{xx,j}) \quad (\text{Eq. A-4})$$

The covariance term can be estimated by (Jenkins & Watts, 1968: 251)

$$\text{cov}(C_{xx}(f_1), C_{xx}(f_2)) \approx \frac{1}{T_{\text{tot}}} \int_{-\infty}^{\infty} \Gamma_{xx}^2(g) W(f_1 - g) \{W(f_2 + g) + W(f_2 - g)\} dg. \quad (\text{Eq. A-5})$$

The standard deviation of the square root of an estimate of the form $y = p\sqrt{x}$ can be estimated using (Jenkins & Watts, 1968: 76)

$$\sigma^2(y) \approx \frac{p^2}{4x} \left| \sigma^2(x) \right|_{x=\langle x \rangle} \quad (\text{Eq. A-6})$$

Thus in this case (no bias assumed)

$$\sigma^2 \left(\sqrt{\sum_{i=a}^b C_{xx,i}} \right) = \frac{1}{4 \sum_{i=a}^b \Gamma_{xx,i}} \left\{ \frac{W_b}{N} \sum_{i=a}^b \Gamma_{xx,i}^2 + \sum_{i=a}^b \sum_{\substack{j=a \\ j \neq i}}^b \text{cov}(C_{xx,i}, C_{xx,j}) \right\} \quad (\text{Eq. A-7})$$

There holds for the standard deviation of a quotient of two estimates of the form $z = x/y$ that

$$\frac{\sigma(z)}{z} = \sqrt{\left(\frac{\sigma^2(x)}{x^2} + \frac{\sigma^2(y)}{y^2} - \frac{2 \text{cov}(x, y)}{xy} \right)} \quad (\text{Eq. A-8})$$

The standard deviation of the rms ratio can be expressed with Equations (A-2), (A-6) and (A-8), assuming that the covariance between

$$\sum_{i=a}^b C_{xx,i} \quad \text{and} \quad \sum_{i=b}^c C_{xx,i}$$

is equal to 0, as

$$\begin{aligned} \frac{\sigma(\text{rms-ratio})}{\text{rms-ratio}} &\approx \frac{1}{2} \left| \frac{\frac{W_b}{N} \sum_{i=a}^b C_{xx,i}^2 + \sum_{i=a}^b \sum_{\substack{j=a \\ j \neq i}}^b \text{cov}(C_{xx,i}, C_{xx,j})}{\left(\sum_{i=a}^b C_{xx,i} \right)^2} + \right. \\ &\left. + \frac{\frac{W_b}{N} \sum_{i=b}^c C_{xx,i}^2 + \sum_{i=b}^c \sum_{\substack{j=b \\ j \neq i}}^c \text{cov}(C_{xx,i}, C_{xx,j})}{\left(\sum_{i=b}^c C_{xx,i} \right)^2} \right| 1/2 \end{aligned} \quad (\text{Eq. A-9})$$

where $\text{cov}(C_{xx,i}, C_{xx,j})$ is given by Equation (A-5).

There follows from Equation (A-9), for a white spectrum ($C_{xx,i}$ is constant) and no spectral leakage that

$$\frac{\sigma(\text{rms-ratio})}{\text{rms-ratio}} = \frac{1}{2} \sqrt{\frac{W_b}{N} \left(\frac{1}{n_1} + \frac{1}{n_2} \right)} \quad (\text{Eq. A-10})$$

where n_1 is the number of spectrum points used for the first interval ($= b - a + 1$), n_2 is the number of spectrum points used for the second interval ($= c - b + 1$).

The standard deviation of the rms ratio was calculated using Equation (A-9) with a Hanning data window ($W_b = 0.75$; Jenkins & Watts, 1968):

$$\begin{aligned}
 W(i\Delta f) = n\Delta \left| \frac{1}{2} \frac{\sin\left(\frac{\pi}{2}(i-1)\right)}{\frac{\pi}{2}(i-1)} + \frac{1}{4} \frac{\sin\left(\frac{\pi}{2}(i-1)+\pi\right)}{\frac{\pi}{2}(i-1)+\pi} + \right. \\
 \left. + \frac{1}{4} \frac{\sin\left(\frac{\pi}{2}(i-1)-\pi\right)}{\frac{\pi}{2}(i-1)-\pi} \right| \quad (\text{Eq. A-11})
 \end{aligned}$$

The integral of Equation (A-5) was calculated numerically (Γ_{xx} was estimated by C_{xx}).

About 12% of the standard deviation is due to the covariance between spectrum points.

Appendix 3: nomenclature

List of most important symbols

A	tube cross-section static amplification	m^2
A_f	fuel-heat transfer area	m^2
A_k	autoregression parameter	
B_g^2	geometric buckling of the neutron flux	m^{-2}
B_m^2	material buckling of the neutron flux	m^{-2}
B_n^2	buckling of the neutron flux of mode n	m^{-2}
Bi	Biot number	
c_f	specific fuel-heat capacity	$J \cdot kg^{-1} \cdot K^{-1}$
c_p	specific heat capacity	$J \cdot kg^{-1} \cdot K^{-1}$
C_k	concentration of delayed-neutron precursors of group k	m^{-3}
C_0	Zuber-Findlay distribution parameter	
$C_{xx}(f)$	estimated auto-power spectral density of x	$[x]^2 \cdot Hz^{-1}$
$C_{xx,i}$	estimated discrete auto-power spectral density of x	$[x]^2 \cdot Hz^{-1}$
d_b	bubble diameter	m
D	pressure neutron-diffusion coefficient tube diameter	$N \cdot m^{-2}$ m m
f	frequency	Hz
f_0	characteristic frequency	Hz
f_R	resonance frequency	Hz
f_{tp}	two-phase friction factor	
F	feedback transfer function	
g	acceleration due to gravity	$m \cdot s^{-2}$
h	impulse response	
H	transfer function	
j	imaginary unit	
J_0	Bessel function of zero order, first kind	
J_1	Bessel function of first order, first kind	
k	thermal conductivity	$W \cdot m^{-1} \cdot K^{-1}$
k_{eff}	multiplication factor of a finite system	

k_{∞}	multiplication factor of an infinite system	
ℓ	relaxation length of the detector field-of-view	m
L	neutron diffusion length	m
L_{ω}	complex neutron diffusion length	m
M^2	neutron migration area	m ²
M_s	steam mass in the vessel	kg
M_w	water mass in the vessel	kg
n	number of samples per record	
	number of energy groups	
	number of points	
N	number of records	
N_A	Avogadro's number	
p	pressure	N·m ⁻²
	autoregression model order	
P	power	W
q	heat current	W
q''	heat flux per unit of surface area	W·m ⁻²
q'''	heat-generation rate density	W·m ⁻³
Q	point neutron-source strength	s ⁻¹
Q_a	volumetric air-flow rate	m ³ ·s ⁻¹
Q_w	volumetric water-flow rate	m ³ ·s ⁻¹
r	distance	m
R	fuel-pellet radius	m
	detection interaction rate	s ⁻¹
Re	Reynolds number	
s	Laplace variable	s ⁻¹
	estimated standard deviation	
S	neutron-source strength density	m ⁻³ ·s ⁻¹
t	time	s
T	temperature	K
	time interval	s
T_c	coolant temperature	K
T_{tot}	total measuring time	s
v	neutron velocity	m·s ⁻¹
v_s	steam velocity	m·s ⁻¹
V_a	air velocity	m·s ⁻¹
V_b	bubble velocity	m·s ⁻¹
V_{bs}	bubble velocity in stagnant water	m·s ⁻¹
V_{bs0}	single-bubble velocity in stagnant water	m·s ⁻¹
V_f	fuel volume	m ³
V_M	volumetric flux	m·s ⁻¹
V_s	steam volume	m ³
	slug velocity	m·s ⁻¹
V_{ss}	slug velocity in stagnant water	m·s ⁻¹
V_w	water volume	m ³

$W(f)$	spectral window	
W_b	window parameter	
W_p	steam-mass production rate	$\text{kg}\cdot\text{s}^{-1}$
W_s	steam-mass flow	$\text{kg}\cdot\text{s}^{-1}$
z	axial height	m
α	heat-transfer coefficient	$\text{W}\cdot\text{m}^{-2}\cdot\text{K}^{-1}$
	void (air) fraction	
β	fraction of delayed neutrons	
γ^2	coherence	
$\Gamma_{xx}(f)$	auto-power spectral density of x	$[\text{x}]^2\cdot\text{Hz}^{-1}$
$\Gamma_{xx,i}$	discrete auto-power spectral density of x	$[\text{x}]^2\cdot\text{Hz}^{-1}$
Δ	sampling time	s
Δh_{ev}	effective specific evaporation enthalpy of water	$\text{J}\cdot\text{kg}^{-1}$
ΔV	time between two successive velocity points	s
η	negative imaginary part of the adjoint function	
λ	relaxation length of light	m
λ_k	decay constant of k^{th} precursor group	s^{-1}
Λ	neutron-generation time	s
μ_w	dynamic viscosity of water	$\text{N}\cdot\text{s}\cdot\text{m}^{-2}$
ν	average number of fast neutrons per fission	
ξ	damping constant	
ρ_a	air-mass density	$\text{kg}\cdot\text{m}^{-3}$
ρ_w	water-mass density	$\text{kg}\cdot\text{m}^{-3}$
ρ_f	fuel-mass density	$\text{kg}\cdot\text{m}^{-3}$
σ	standard deviation	
	rate of decay index	s^{-1}
σ_s	steam-mass density	$\text{kg}\cdot\text{m}^{-3}$
σ_w	water-mass density	$\text{kg}\cdot\text{m}^{-3}$
Σ_a	macroscopic absorption cross-section	m^{-1}
Σ_d	macroscopic detector cross-section	m^{-1}
Σ_f	macroscopic fission cross-section	m^{-1}
$\Sigma_{s,ij}$	macroscopic scattering cross-section from group i to j	m^{-1}
τ	transit time	s
	Fermi age	m^2
τ_f	fuel time constant	s
τ_s	mean residence-time of the steam in the vessel	s
Φ	neutron-flux density	$\text{m}^{-2}\cdot\text{s}^{-1}$
	linear heat flux	$\text{W}\cdot\text{m}^{-1}$
ϕ^+	adjoint function	
χ_i	fraction of neutrons produced by fission in energy group i	
ψ	real part of the adjoint function	
ω	radial frequency	s^{-1}

List of abbreviations

ACF	auto-correlation function
APRM	average power range monitor
APSD	auto-power spectral density
AR	autoregressive
BWR	boiling water reactor
CCF	cross-correlation function
CPSD	cross power spectral density
DR	decay ratio
FOV	field-of-view
NAPSD	normalised auto-power spectral density
PDF	probability density function
PSD	power spectral density
rms	root mean square
RTF	reactivity-to-power transfer function
TIP	traversing in-core probe
TSPGD	twin self-powered gamma detector
TSPND	twin self-powered neutron detector
UV	ultra-violet

Stabiliteitsbewaking van een door natuurlijke circulatie gekoelde kokend-waterreactor

Samenvatting

Methodes voor het bewaken van de stabiliteit van een kokend-waterreactor (BWR) worden behandeld. Het toezicht houden op de stabiliteit van BWRs is van belang daar stabiliteitsproblemen zijn opgetreden in verschillende grote reactoren. Bovendien maakt het de bedrijver van een centrale mogelijk een hoog vermogen te produceren met aanvaardbare stabiliteitsgrenzen.

De resultaten van experimenten die zijn uitgevoerd bij de kokend-waterreactor te Dodewaard (Nederland) worden vermeld. Onderzoek aan juist dit reactortype is van belang daar dit type wordt gekoeld door natuurlijke circulatie, een koelprincipe dat ook wordt overwogen voor nieuwe reactorontwerpen. Op het moment zijn slechts twee reactoren van dit type in bedrijf.

De stabiliteit van de Dodewaard-reactor is zowel met deterministische methoden (regelstaafstappen en druk-klepbewegingen) als door middel van ruisanalyse bestudeerd. Deze laatste methode kan gedurende normaal bedrijf worden toegepast en verstoort het systeem niet, daar het kookproces van het water in de kern een continue intrinsieke ruisbron vormt. Drie typen stabiliteit worden onderscheiden die elk afzonderlijk werden onderzocht: reactorkinetische stabiliteit, thermohydraulische stabiliteit en de stabiliteit van het totale systeem. Aangetoond wordt dat de Dodewaard-reactor zeer grote stabiliteitsmarges heeft.

Een eenvoudig maar betrouwbaar stabiliteitscriterium dat grondig werd getest, wordt geïntroduceerd. Dit criterium kan gedurende normaal bedrijf worden afgeleid uit de ruissignalen van de neutronendetectors buiten het reactorvat. Om een correcte stabiliteitsbewaking te garanderen, werd de gevoeligheid berekend van de neutronendetectors voor fluxverstoringen in de kern die wordt weergegeven in het zogenaamde gezichtsveld van de detector.

Een nieuwe techniek wordt gepresenteerd die het mogelijk maakt de variatie van de koelmiddelsnelheid door de kern te bepalen door middel van ruisrelatie. De interpretatie van de gemeten snelheid werd bestudeerd aan de hand van metingen aan een lucht/water-model van een koelkanaal van een BWR. Uit de resultaten bleek dat de gemeten snelheid

veel hoger is dan de volume-gemiddelde watersnelheid, de volume-gemiddelde luchtsnelheid en de volumetrische flux, waarden die door andere onderzoekers als interpretatie geponeerd zijn.

De toepasbaarheid van deze methode voor het bewaken van de lokale stabiliteit van de stroming door een koelkanaal werd onderzocht. Het bleek dat de invloed van de stabiliteit op de koelmiddelsnelheid gemaskeerd wordt door andere effecten die voortkomen uit het lokale stromingstype. Daar de stroming in de Dodewaard-reactor erg stabiel is, zijn de variaties van de koelmiddelsnelheid echter erg klein.

Experimenteel en theoretisch onderzoek werd verricht aan de splijtstof tijdconstante, een parameter die van groot belang is voor de reactor-kinetische stabiliteit. Aangetoond wordt dat de effectieve waarde van deze constante veel geringer kan zijn dan tot dusver werd aangenomen.

Tenslotte werden de gepresenteerde methoden voor het bewaken van de stabiliteit toegepast onder verschillende condities van de kern van de Dodewaard-reactor.

摘要

沸騰水型原子炉（BWR）の安定性をモニタリングする方法が論じられる。いくつかの大型原子炉で問題が生じたのでBWRの安定性の監視は重要と言える。さらに、安定性の監視により、発電所の経営者が原子炉を許容安定性限度内で高出力で操業することが可能となる。

ドーデヴァールト（オランダ）のBWRで行なわれた実験の結果が報告される。同原子炉の研究が特に興味深い理由は、自然循環により冷却されるタイプだからである。この冷却原理は、新型原子炉設計でもその使用が考慮されている。同タイプの原子炉で現在操業されているのは二つだけである。

ドーデヴァールトの原子炉の安定性が、確定的方法（制御棒の上下運動・圧力弁の動き）及び雑音解析によって検討された。後者の方法については、炉心の水の沸騰過程が連続固有雑音源であるため、正常運転中に使用でき、いかなる故意的システム外乱も避けることができる。原子炉動特性的安定性、熱水力学的安定性、トータルシステムの安全性の三つのタイプの安定性が区別され、個別に検討された。ドーデヴァールトの原子炉は安定性に極めて十分の余裕があることが明らかにされる。

簡単でしかも信頼性のある、徹底的に試験済みの安定性基準が紹介される。同基準は正常運転中、原子炉容器外の中性子検出器の雑音シグナルからオンラインで導くことができる。適切な安定性監視を保証するため、中性子検出器のいわゆる検出器の視野に反映される一炉心中の中性子束振動に対する感度が計算された。

炉心中の冷却材速度の変動値を雑音との相関関係により測定することを可能にする新しい技術が紹介される。測定された速度は、空気／水の流れに関してBWR冷却材チャンネルの模型を用いて行なわれた試験をもとに解釈された。この分析の結果、測定された速度が、他の研究者が同等の有効性を認めていた水の体積平均速度、空気の体積平均速度、並びに、体積フラックスを大幅に上回っていることが明らかになった。

チャンネルの流れの局部安定性をモニタリングする上での上述の技術の適用可能性が試験された。安定性が冷却材の速度に及ぼす影響が局部流れ方式から生ずる他の効果により隠されてしまうことが観察された。ただし、ドーデヴァールトの原子炉では、チャンネルの流れが極めて安定しているため、冷却材速度の変動が非常に少ない。

原子炉動特性的安定性の重要なパラメーターである燃料時定数に関して実験的・理論的研究が行なわれた。この時定数の実効値が普通考えられているよりずっと低い可能性があることが明らかにされる。

最後に、紹介された安定性のモニタリング方法がドーデヴァールト原子炉で色々な条件の下に試みられた。

Acknowledgements

Several people contributed to the present study in one way or another; I thank all of them and I wish to express my special gratitude explicitly to a number of them.

First of all, I would like to thank Prof. Dr. Ir. H. van Dam for giving me the opportunity of performing this study in the Department of Reactor Physics of the Interfaculty Reactor Institute and for his advices, criticisms and suggestions concerning the research. Dr. Ir. Eduard Hoogenboom is greatly acknowledged for introducing me into the world of reactor noise, for his permanent attention and for the many valuable discussions. Jelle Schut, whose excellent craftsmanship played an important role in the design and manufacturing of the 'bubble tube' and the self-powered detectors, is greatly thanked. Thanks are also due to my predecessor, Dr. Ir. Erik Kleiss, for his outstandingly useful advices and his never flagging interest in the progress of the project. I am indebted to Dick de Haas for his assistance at even the most inconvenient moments and to Ir. Piet de Leege, Theo van Bloois and all other members of the Department of Reactor Physics for their help and continuous concern.

I wish to express my gratitude to Ir. Jaap van der Voet for his contribution during his last year of study for physical engineer and afterwards, when working as an employee of the Dodewaard company.

The experiments at the Dodewaard reactor could not have been performed without the co-operation of the Dodewaard management; I thank Ir. Jan Hoekstra and Ir. Peter van der Hulst for providing a perfect research atmosphere. Wim Nissen is greatly acknowledged for his enthusiastic and skilful help and for his valuable ideas and suggestions.

Thanks are due to Drs. Jan van der Veer and Dr. Ir. Willem-Jan Oosterkamp of N.V. KEMA for their useful suggestions.

I am indebted to the KEMA editor Dr. Tom van Loon and his assistant Janette Rietbergen for putting the finishing touches to the thesis.

Finally, I would like to thank Drs. Jan Linders for his advices as to the English text.

Tim van der Hagen

Curriculum vitae

- October 7th, 1959 : born at Tilburg, The Netherlands
- 1972-1978 : attending high school at the 'Maurick College' at Vught;
Gymnasium- β certificate
- 1978-1984 : studying physical engineering at the Eindhoven University of Technology
projects: - Doppler broadening of spectral lines in a neon discharge tube
- free-electron laser based on Smith-Purcell radiation (Tel-Aviv)
- inharmonicity of piano strings
Masters project (the development of a micro-anemometer) performed in the group of Prof. Dr. J.A. Poulis
- December 12th, 1984 : Master of Science degree
- Jan. 1985 - March 1989 : performing research in the field of boiling-water-reactor noise at the Department of Reactor Physics of the Interfaculty Reactor Institute of the Delft University of Technology